5-2018

Microstructure, Luminescence, and Performance of Garnet Polycrystalline Ceramic Scintillators

Artem Trofimov
Clemson University, atrofim@g.clemson.edu

MICROSTRUCTURE, LUMINESCENCE, AND PERFORMANCE OF GARNET POLYCRYSTALLINE CERAMIC SCINTILLATORS

A Dissertation
Presented to
the Graduate School of
Clemson University

In Partial Fulfillment
of the Requirements for the Degree
Doctor of Philosophy
Materials Science & Engineering

---

by
Artem A. Trofimov
May 2018

Accepted by:
Luiz G. Jacobsohn, Committee Chair
Kyle S. Brinkman
Timothy A. DeVol
Fei Peng

ABSTRACT

Polycrystalline ceramic scintillators have received increasing attention due to a number of advantages over single crystals, including faster production and lower fabrication costs and easier fabrication of materials with high melting temperatures. Nevertheless, scintillation performance of polycrystalline ceramics is commonly inferior to single crystals. In the present work, a detailed comparative investigation of the family of garnet scintillators in the form of polycrystalline ceramic and single crystal scintillators was performed in terms of their microstructure, as well as optical and luminescent properties, to gain insight into the factors influencing their scintillation performance. The use of infrared vibrational spectroscopy to gain relevant microstructural information was demonstrated for polycrystalline ceramic scintillators. The investigation was focused on $Y_3Al_5O_{12}$:Ce (YAG:Ce), $Lu_3Al_5O_{12}$:Ce (LuAG:Ce), $Lu_3Al_5O_{12}$:Pr (LuAG:Pr), mixed garnets $(Lu,Gd)_3(Al,Ga)_5O_{12}$:Ce, and $Li_7La_3Zr_2O_{12}$:Ce (LLZO:Ce). Evaluation and analysis of material properties revealed reasons for lower performance of polycrystalline ceramic scintillators including lower optical transparency, higher level of structural disorder, higher self-absorption, and possibly shallower traps. This work reports for the first time a systematic evaluation of microstructure, luminescence, and scintillation performance of $(Lu,Gd)_3(Al,Ga)_5O_{12}$:Ce in the form of polycrystalline ceramics focusing on the effect of the substitution of Lu^{3+} with Gd^{3+}, and also the fabrication and characterization of luminescent properties of Ce-doped $Li_7La_3Zr_2O_{12}$ towards the discovery of new scintillating materials.

DEDICATION

I dedicate this work to my wonderful parents, Aleksandr and Tatiana Trofimov, and my beautiful fiancée, Katie Burdette, with love. Without your never-failing support and encouragement this PhD journey would not be possible. Спасибо мои дорогие мама и папа и спасибо любимая. Люблю вас очень сильно!

ACKNOWLEDGMENTS

I wish to express my gratitude to my adviser Dr. Luiz G. Jacobsohn for his advice, guidance, and willingness to provide me with invaluable knowledge. I thank my committee members Dr. Timothy A. DeVol, Dr. Kyle S. Brinkman, and Dr. Fei Peng for their time, advice, and lab space. I would also like to thank Dr. Charles Melcher from University of Tennessee for the single crystals used in the present work, Dr. Ronaldo S. da Silva from Federal University of Sergipe in Brazil for $Y_3Al_5O_{12}$:Ce polycrystalline ceramics, Dr. Yimin Wang from Radiation Monitoring Devices Inc. for $(Gd,Lu)_3(Ga,Al)_5O_{12}$:Ce samples, as well as Dr. Colin McMillen, Dr. John M. Ballato, Dr. Stephen H. Foulger, and Courtney Kucera for providing advice and lab equipment.

I am incredibly thankful to my fiancée, Katie Burdette, and my best friends, Dmitry Gil and Nick Borodinov, for their encouragement and companionship. I wish them the most successful research career and future endeavors. I am much oblige to my parents for their encouragement through all these years.

I would also like to thank my current and former group members Matthew Chapman, Matthew Marchewka, Matthew Kielty, and Yu (Michelle) Wu for their assistance and advice, as well as Changlong Li from Dr. Brinkman's group for his assistance with the synthesis of $Li_7La_3Zr_2O_{12}$:Ce.

This material is based upon work supported by the National Science Foundation under Grant № 1207080 and 1653016 (CAREER).

TABLE OF CONTENTS

Page

TITLE PAGE i

ABSTRACT ii

DEDICATION iii

ACKNOWLEDGMENTS iv

TABLE OF CONTENTS v

LIST OF TABLES vii

LIST OF FIGURES ix

CHAPTER

I. INTRODUCTION 1

1.1 Objectives 1
1.2 Basic principles of scintillation mechanism 2
1.3 Development of ceramic scintillators 5
1.4 Development of garnet scintillators 7
References 19

II. EXPERIMENTAL PROCEDURES 28

2.1 Materials 28
2.2 Characterization techniques 30
2.2.1 X-ray diffraction (XRD) 30
2.2.2 Scanning electron microscopy (SEM) and energy dispersive X-ray spectroscopy (EDX) 34
2.2.3 Density measurements 39
2.2.4 Attenuated total reflectance Fourier transform infrared spectroscopy (ATR FTIR) 41
2.2.5 Ultraviolet/visible (UV/Vis) spectroscopy 43

Table of Contents (Continued)

Page

2.2.6 Photoluminescence (PL) 45
2.2.7 Radioluminescence (RL) 54
2.2.8 Thermoluminescence (TL) 55
2.2.9 Differential pulse height distribution measurements 60
References 64

III. RESULTS AND DISCUSSION 66

3.1 Microstructure, luminescence, and scintillation of laser-sintered ceramic and single crystal $Y_3Al_5O_{12}$:Ce (YAG:Ce) 66
3.2 Comparative investigation of transparent ceramic and single crystal $Lu_3Al_5O_{12}$:Ce (LuAG:Ce) scintillators 89
3.3 Microstructure and optical and luminescence properties of $Lu_3Al_5O_{12}$:Pr (LuAG:Pr) 110
3.4 Microstructure and luminescence of $(Gd,Lu)_3(Ga,Al)_5O_{12}$:Ce (GLuGAG:Ce) polycrystalline ceramic scintillators with various Gd/Lu ratios 125
3.5 Luminescence investigation of Ce incorporation in garnet-type $Li_7La_3Zr_2O_{12}$ (LLZO) 142
References 149

IV. CONCLUSIONS AND FUTURE WORK 157

4.1 Conclusion 157
4.2 Future work 158

LIST OF TABLES

Table		Page
2.1	Specifications of Ce-doped $(Lu_{3-x}, Gd_x)(Al_{0.6}, Ga_{0.4})_5O_{12}$ polycrystalline ceramics	30
2.2	Electron configurations of rare-earth elements	46
2.3	Correspondence of *L* values to letter symbols	48
2.4	Point sources and their energies used for differential pulse height distribution measurements	63
3.1	Literature review of defect excitation and emission in YAG and YAG:Ce in the order of increasing energies	77
3.2	Parameters of the glow peaks and corresponding traps using McKeever-Chen expression	83
3.3	Parameters of the traps using glow curve fitting	85
3.4	Parameters of the traps using multiple heating rates method	87
3.5	Literature review of defect excitation and emission in LuAG and LuAG:Ce at room temperature in the order of increasing emission energy	100
3.6	Parameters of the glow peaks and corresponding traps using McKeever-Chen expression	105
3.7	Summary of the analysis of glow curves of LuAG:Ce polycrystalline ceramic using GlowFit software for different irradiation times	106
3.8	Summary of the analysis of glow curves of LuAG:Ce single crystal using GlowFit software for different irradiation times	106
3.9	Summary of the analysis of glow curves of LuAG:Ce polycrystalline ceramic using combination of GlowFit software and McKeever-Chen formula for different irradiation times	107

List of Tables (Continued)

Table Page

3.10 Summary of the analysis of glow curves of LuAG:Ce single crystal using combination of GlowFit software and McKeever-Chen formula for different irradiation times 107

3.11 $4f \rightarrow 4f$ transitions observed in PL measurements of LuAG:Pr 121

LIST OF FIGURES

Figure Page

1.1 Schematic of the band structure of an inorganic scintillator and the scintillation process at an extrinsic luminescent center 5

1.2 Evolution of the light yield of YAG:Ce single crystals and polycrystalline ceramics reported in the literature 10

1.3 Evolution of the light yield of LuAG:Ce single crystals and polycrystalline ceramics reported in the literature 14

2.1 Bragg's relationship between incident and diffracted X-ray beams 31

2.2 Rigaku Ultima IV X-ray diffractometer used to characterize crystalline structure. a) outside view; b) inside view 33

2.3 a) General structure of a SEM; b) General structure of an electron gun 34

2.4 a) Electron detection in SEM; b) Schematic of EDX in an SEM 37

2.5 Universal specific gravity kit, bench model SGK-B 40

2.6 Schematic of a Michelson interferometer in transmission FTIR 42

2.7 a) A schematic of a single reflection ATR; b) Thermo-Scientific Nicolet 6700 FTIR spectrometer with a diamond crystal ATR plate 43

2.8 a) A schematic of a double beam UV/Vis spectrophotometer; b) Perkin Elmer Lambda 950 UV/Vis/NIR spectrophotometer 45

2.9 Orbitals available for an *f* electron with electrons placed for the case of Ce^{3+} (f^1) and Pr^{3+} (f^2) 49

2.10 Section of a Dieke diagram showing energy levels of Ce^{3+} and Pr^{3+} ions... 50

2.11 a) A schematic representation of the energy levels splitting of Ce^{3+} in a garnet matrix; b) The absorption and emission energies in a vibrating lattice showing the Stokes shift 52

List of Figures (Continued)

Figure Page

2.12 a) A schematic diagram of photoluminescence spectrofluorometer; b) Horiba Jobin-Yvon Fluorolog-322 spectrofluorometer 54

2.13 Custom-designed Freiberg Instruments Lexsyg Research spectrofluorometer 55

2.14 a) Common electronic transitions in inorganic scintillators; b) Correlation between TL intensity and a number of electrons released from the traps and recombined 57

2.15 Computer-simulated a) first- and b) second-order kinetics glow-curves 59

2.16 Thermo Scientific Harshaw TLD reader model 3500 60

2.17 A schematic representation of differential pulse-height measurements apparatus 61

2.18 Pulse height distribution measurements apparatus with Hamamatsu R6095 bialkali photocathode photomultiplier tube 63

3.1 XRD results of YAG:0.3% Ce polycrystalline ceramic indexed according to ICDD #00-033-0040 66

3.2 SEM micrographs of YAG:0.3%Ce polycrystalline ceramic 67

3.3 Pulse height spectra of 59.5 keV γ-rays from ^{241}Am point source. (a) YAG:Ce single crystal (gain 50), (b) YAG:0.1%Ce polycrystalline ceramic (gain 250) and (c) YAG:0.3%Ce polycrystalline ceramic (gain 250) 68

3.4 Light yield of the YAG:Ce relative to BGO crystal 69

3.5 Normalized absorption ATR FTIR spectra of the YAG:Ce 71

3.6 PL (blue circles) and PLE (black lines) spectra of a) YAG:Ce single crystal, b) YAG:0.1%Ce polycrystalline ceramic, and c) YAG:0.3%Ce polycrystalline ceramic 73

List of Figures (Continued)

Figure Page

3.7 Normalized RL spectra of YAG:Ce single crystal (black), YAG:0.1%Ce polycrystalline ceramic (red), and YAG:0.3%Ce polycrystalline ceramic (blue) 75

3.8 PLE spectrum monitored at 3.21 eV (386 nm; red), and PL spectrum excited at 4.54 eV (273 nm; blue) for a) YAG:Ce single crystal, b) YAG:0.1%Ce polycrystalline ceramic, and c) YAG:0.3%Ce polycrystalline ceramic 76

3.9 Optical transmission of YAG:Ce single crystal (black), YAG:0.1%Ce polycrystalline ceramic (red), and YAG:0.3%Ce polycrystalline ceramic (blue) 79

3.10 TL glow curves of YAG:Ce single crystal (black), YAG:0.1%Ce polycrystalline ceramic (red), and YAG:0.3%Ce polycrystalline ceramic (blue) 80

3.11 TL glow curves obtained using different X-ray irradiation time for (a) YAG:Ce single crystal, (b) YAG:0.1%Ce polycrystalline ceramic and (c) YAG:0.3%Ce polycrystalline ceramic 81

3.12 Decomposition of glow curves (black circles) of (a) YAG:Ce single crystal, (b) YAG:0.1%Ce polycrystalline ceramic and (c) YAG:0.3%Ce polycrystalline ceramic X-ray irradiated for 120 sec 84

3.13 Comparison of the present results of TL peak positions to the literature on TL of YAG:Ce 85

3.14 Experimental points and fits for TL glow peaks using method of multiple heating rates. (a) YAG:0.2%Ce single crystal, (b) YAG:0.1%Ce polycrystalline ceramic and (c) YAG:0.3%Ce polycrystalline ceramic 87

3.15 Pulse height spectra of γ-rays from ^{22}Na point source. (a) LuAG:Ce single crystal, (b) LuAG:Ce polycrystalline ceramic and (c) BGO single crystal 90

List of Figures (Continued)

Figure Page

3.16 Light yield of LuAG:Ce single crystal (black squares) and polycrystalline ceramic (red circles) normalized to the light yield of a BGO crystal for each γ-ray energy used 91

3.17 Normalized absorption ATR FTIR spectra of the LuAG:Ce single crystal and polycrystalline ceramic normalized to the most intense peak 93

3.18 Optical transmission of LuAG:Ce single crystal and polycrystalline ceramic 94

3.19 PL (blue circles) and PLE (black circles) spectra of a) single crystal, and b) polycrystalline ceramic 95

3.20 RL spectra (black circles) together with Gaussian deconvolution (green lines) and best fit (red lines) for the single crystal (a and c), and polycrystalline ceramic (b and d) 97

3.21 Superimposition of RL results (blue lines) and optical transmission results (red lines) for the a) single crystal, and b) polycrystalline ceramic 97

3.22 PLE spectrum monitored at 2.95 eV (420 nm; red), and PL spectrum excited at 3.53 eV (351 nm; blue) for a) single crystal and b) polycrystalline ceramic 99

3.23 Comparison of the present results of TL peak positions to the literature on TL of LuAG:Ce 102

3.24 Mass-normalized TL glow curves of LuAG:Ce single crystal (black circles) and polycrystalline ceramic (red circles) 103

3.25 TL glow curves of a) single crystal, and b) polycrystalline ceramic obtained after irradiation with X-ray for different times 104

3.26 Dependence of the FWHM of the glow peaks on the peak temperature, according to eq. (3.1) 109

3.27 Activation energy, *E*, of the traps in LuAG:Ce single crystal and polycrystalline ceramic for different peak positions, T_m 109

List of Figures (Continued)

Figure Page

3.28 (A) Evolution of the density of LuAG:Pr polycrystalline ceramic as a function of sintering temperature; (B) Average grain size as a function of the relative density 111

3.29 (A) XRD investigation of LuAG:Pr polycrystalline ceramics as a function of sintering temperature; (B) Comparison of the width of the XRD peak at different sintering temperatures; (C) Lattice parameter of polycrystalline LuAG:Pr as a function of sintering temperature 113

3.30 ATR FTIR spectra of LuAG:Pr single crystal and polycrystalline ceramics fabricated at various sintering temperatures 114

3.31 Transmission spectra of LuAG:Pr polycrystalline ceramics fabricated at various sintering temperatures 115

3.32 (A) RL spectra of LuAG:Pr normalized to the most intense peak at ca. 3.3 eV; (B) Ratio of the integrated intensities of emission from *5d* → *4f* transitions to *4f* → *4f* transitions of Pr^{3+} as a function of sintering temperature 116

3.33 RL spectra (black curves) of polycrystalline ceramics sintered at (A) 1400 °C, (B) 1500 °C, (C) 1600 °C, (D) 1700 °C, and (E) RL spectra of the single crystal; (F) Integrated intensities of *5d* → $^3F_{3(4)}$ (black squares), *5d* → $^3H_6$ (red circles), *5d* → $^3H_5$ (blue triangles)), and 5*d* → $^3H_4$ (purple rhombs) transitions relative to the total integrated intensity 118

3.34 Normalized emission (PL; solid lines) and excitation (PLE; dashed lines) spectra of LuAG:Pr polycrystalline ceramics and single crystal. (A) Spectra corresponding to *4f* → *5d* and *5d* → *4f* transitions of Pr^{3+}; (B) Spectra corresponding to *4f* → *4f* transitions of Pr^{3+} 120

3.35 Normalized emission (PL; solid line) and excitation (PLE; dashed line) spectra of defects in LuAG:Pr polycrystalline ceramics and single crystal 123

3.36 Normalized TL glow curves of the single crystal and the polycrystalline ceramics sintered at different temperatures 124

List of Figures (Continued)

Figure Page

3.37 (A) Surface area-normalized TL glow curves of the polycrystalline LuAG:Pr sintered at different temperatures; (B) Surface area-normalized integral TL intensity as a function of sintering temperature 125

3.38 SEM micrographs of GLuGAG:Ce polycrystalline ceramics 126

3.39 (a) EDX evaluation of Gd and Lu content in GLuGAG:Ce polycrystalline ceramics; (b) Evolution of the average grain size of the samples as a function of Gd content 127

3.40 (a) XRD results of GLuGAG:Ce polycrystalline ceramics; (b) Diffraction peak shift of GLuGAG:Ce at different Gd/Lu ratios... 128

3.41 (a) The peak position shift of the most intense diffraction peak and (b) change of the lattice constant of GLuGAG:Ce at different Gd/Lu ratios 128

3.42 Absorption ATR FTIR spectra of GLuGAG:Ce polycrystalline ceramics normalized to the peak between 650-700 cm^{-1} 130

3.43 Dependence of the peak position of the resolved IR modes on the unit cell volume of GLuGAG:Ce polycrystalline ceramics..... 131

3.44 Transmission of GLuGAG:Ce polycrystalline ceramics at different Gd/Lu ratios 132

3.45 (a) Ce^{3+} related PLE of GLuGAG:Ce polycrystalline ceramics with different Gd/Lu ratios; (b) Dependence of the peak position of the Ce^{3+} $4f \rightarrow 5d_2$ excitation on Gd content in comparison to the SCF and powder of similar compositions..... 133

3.46 (a) The binding energy (VRBE) for electrons in the 4*f* ground state and first two excited 5*d* states of Ce^{3+} in the $RE_3(Al_{1-x}Ga_x)_5O_{12}$ garnet compounds (b) Schematic representation of the increase of Gd/Lu ratio on Ce^{3+} levels in garnets..... 134

List of Figures (Continued)

Figure Page

3.47 (a) Ce^{3+} related PL of GLuGAG:Ce polycrystalline ceramics with different Gd/Lu ratios; (b) Dependence of the peak position of the Ce^{3+} $5d_1 \rightarrow 4f$ emission on Gd content in comparison to the SCF and single crystal of similar compositions 135

3.48 (a) Gd^{3+} related PLE (solid lines; E_{em} = 3.96 eV) and PL (dashed lines; E_{ex} = 4.53 eV) of GLuGAG:Ce polycrystalline ceramics with different Gd/Lu ratios; (b) Concentration quenching of Gd^{3+} emission in GLuGAG:Ce polycrystalline ceramic 136

3.49 (a) F^{+} related PLE (solid lines; E_{em} = 3.26 eV) and PL (dashed lines; E_{ex} = 3.72 eV) and (b) V_O related PLE (solid lines; E_{em} = 3.02 eV) and PL (dashed lines; E_{ex} = 3.32 eV) of GLuGAG:Ce polycrystalline ceramics with different Gd/Lu ratios 137

3.50 (a) Eu^{3+} related PLE (solid lines; E_{em} = 1.80 eV) and PL (dashed lines; E_{ex} = 2.11 eV) and (b) and (c) Nd^{3+} related PLE (solid lines; (b) E_{em} = 3.24 eV; (c) E_{em} = 1.53 eV) and PL (dashed lines; (b) E_{ex} = 4.68 eV; (c) E_{ex} = 1.68 eV) of GLuGAG:Ce polycrystalline ceramics 139

3.51 Pulse height distribution of GLuGAG:Ce polycrystalline ceramics with different Gd/Lu ratios and BGO single crystal excited with ^{241}Am 141

3.52 Light yield of GLuGAG:Ce polycrystalline ceramics relative to the light yield of BGO single crystal for each γ-ray energy used. (a) “Sintered only” samples, (b) HIPed samples 141

3.53 XRD results of $Li_7(La_{1-x}Ce_x)_3Zr_2O_{12}$ with x = 0, 0.005, 0.01, 0.03, and 0.05, together with calculated diffractograms of cubic and tetragonal LLZO 143

3.54 a) Normalized RL spectra of $Li_7(La_{1-x}Ce_x)_3Zr_2O_{12}$ with x = 0, 0.005, 0.01, 0.03, and 0.05 obtained at room temperature. Gaussian band deconvolution of RL spectra for b) x = 0, c) x = 0.005, d) x = 0.01, e) x = 0.03, and f) x = 0.05 144

List of Figures (Continued)

Figure Page

3.55 a) Peak position of Gaussian bands used in the deconvolution of RL spectra obtained at room temperature, and b) 2.41/2.78 integrated band intensity ratio as a function of the nominal Ce content.....146

3.56 RL spectra obtained at different temperatures for a) x = 0, b) x = 0.005, and c) x = 0.01.....147

3.57 Results of Gaussian band spectral deconvolution as a function of temperature for x = 0.005, and 0.01: a) peak position, and b) integrated band intensity ratio 148

CHAPTER ONE

INTRODUCTION

1.1 Objectives

Scintillators are unique materials capable of emitting ultraviolet and visible photons upon absorption of high energy ionizing radiation. They are employed for the detection and measurement of ionizing radiation in many strategic fields including security, medical imaging and diagnostics, environmental monitoring, high-energy physics, and oil logging [1]. While many scintillation detectors use single crystals due to their high luminosity, polycrystalline transparent ceramic scintillators have received considerable attention as a feasible alternative due to such advantages as faster and lower cost fabrication methods, higher homogeneity of the dopant (luminescent center) distribution, greater shape control, and easier fabrication of materials with high melting temperature (preparation of polycrystalline ceramics does not require melting of raw materials unlike the preparation of single crystals) [2]. However, despite the aforementioned benefits, the overall scintillation performance of polycrystalline ceramics is typically inferior to that of single crystals, and the reasons for this behavior are still not fully understood. Microstructure-luminescence/scintillation property relationships are necessary for improving performance of polycrystalline scintillators.

This research corresponds to a detailed investigation of the microstructural and scintillation features of polycrystalline ceramic scintillators in order to better understand factors influencing scintillation behavior with particular emphasis on the light yield. The investigation is focused on garnet and garnet-type materials: $Y_3Al_5O_{12}$:Ce (YAG:Ce), $Lu_3Al_5O_{12}$:Ce (LuAG:Ce), $Lu_3Al_5O_{12}$:Pr (LuAG:Pr), $(Lu,Gd)_3(Al,Ga)_5O_{12}$:Ce solid solutions, and $Li_7La_3Zr_2O_{12}$:Ce (LLZO:Ce). YAG:Ce is commonly used as a detector in scanning electron microscopy (SEM)

and transmission electron microscopy (TEM) [3, 4]; LuAG:Ce and LuAG:Pr are promising scintillators for the next generation of positron emission tomography (PET) scanners [5-7]. Additionally, $(Lu,Gd)_3(Al,Ga)_5O_{12}$:Ce is an excellent example of composition engineering, where gallium is used to control the band-gap and gadolinium is used to adjust the position of energy levels of the luminescence center, aiming at the enhancement of the light yield [8], and LLZO:Ce is investigated as a new material for potential scintillation applications.

This research has the potential to bridge the knowledge gap between the microstructure of polycrystalline scintillators with their scintillation performance. As a result, the fabrication of polycrystalline ceramic scintillators with comparable or even superior performance relative to the single crystal analogy may be achieved.

1.2 Basic principles of scintillation mechanism

The main idea of the scintillation mechanism is the conversion of energy of an incident particle (alpha or beta particles) or energetic photon (X-ray or γ-ray) into a large number of photons of much lower energy in the visible or ultraviolet range. These lower energy photons can be detected using a photodetector (photomultiplier, photodiode), and the combination of a scintillator with a photodetector is called a scintillation counter [1, 9]. Depending on the application and the type of ionizing radiation being detected, the scintillator may be in the form of a single crystal [10, 11], powder [12], polycrystalline ceramic [13, 14], fiber [15, 16], glass [17], liquid [18], or plastic [19]. The present work is focused on ceramic scintillators and, thus, the discussion on the mechanism of scintillation is restricted to inorganic solid scintillators.

An inorganic scintillator can be intrinsic or extrinsic, depending on whether or not the host matrix includes a luminescent dopant known as the activator. An intrinsic scintillator has inherent luminescent centers, *i.e.*, a specific element in the compound, while an extrinsic

scintillator has a dopant intentionally incorporated in the material to promote luminescence (*e.g.* Ce^{3+} and Pr^{3+} ions). A schematic energy diagram of an inorganic extrinsic scintillator is shown in Figure 1.1. Since scintillators are primarily insulating materials, all electrons are bound to the atoms of the material, creating a filled valence band. At the same time, the higher energy conduction band is able to accommodate energetic electrons which are able to move freely throughout the material. An intermediate region between these two bands represents a zone which electrons are forbidden to occupy in a pure crystal and is known as the band gap. Since the band gap of the insulators is typically several electron-volts (eV), electrons promoted to the conduction band would directly de-excite to the valence band emitting photons outside the visible light range, which are inefficiently detected by photodetectors. Thus, a luminescent center is commonly introduced in a material, where it forms localized energy states within the band gap.

The mechanism of scintillation can be divided in the following stages (see Figure 1.1):

1. Absorption of the incident ionizing radiation and creation of electron-hole pairs.

The scintillation process starts with the absorption of incoming high-energy photons by the electrons in the material matrix. These photons interact with the electrons through one of three mechanisms: the photoelectric effect (photon transfers its energy to the electron, ejecting it from one of the shells of the absorber atom), Compton scattering (photon is scattered off of an electron of the material transferring part of its energy to the electron), and pair production (the energy of a photon converted into an electron-positron pair in the vicinity of an atomic nucleus; however, this mechanism has significant probability to occur only at very high energies (<2 MeV) and, it is not considered in this work) [17]. The electrons that are excited from the valence band into the conduction band of the material due to absorption of energy from photons or

particles of ionizing radiation are known as primary electrons. The primary electrons are ejected from the parent atoms with considerable kinetic energy, leaving behind holes in the normally filled valence band and forming the electron-hole (e-h) pairs. These primary electrons then proceed to collide with other electrons in the scintillator, ejecting additional electrons and generating additional e-h pairs. The process continuous in a cascading manner until the energy of the ejected electrons no longer exceeds the energy threshold required to eject any further electrons from atoms of the host material. As a result, tens of thousands of e-h pairs are generated [1, 9].

2. Thermalization of the electron-hole pairs.

The generated e-h pairs lose their energy through phonon generation and heat transfer, until the electrons reach the bottom of the conduction band and the holes correspondingly reach the top of the valence band.

3.1. Motion of the charge carriers through the material towards the luminescent center.

3.2. Potential trapping of the electrons and holes.

During their motion through the scintillator, the electrons and/or holes can be captured by electronic traps and are no longer available for radiative recombination. These traps correspond to the electronic manifestation of structural defects in the material, e.g., vacancies, interstitials, impurities, etc., that commonly create local energy levels within the band gap. The presence of these traps is highly detrimental to the scintillation performance since they diminish the scintillation output by capturing the charge carriers [20, 21].

4. Transfer of energy from the electron-hole pairs to the luminescent centers and their excitation.

5. De-excitation of the luminescent center with an emission of light.

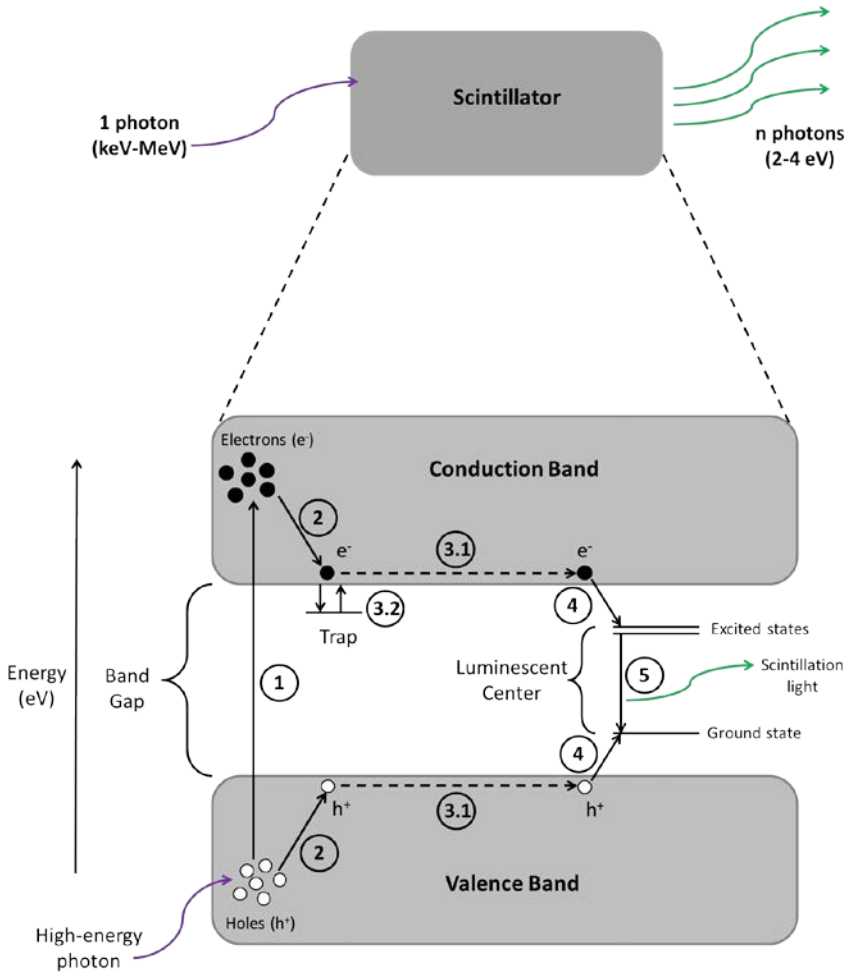

Figure 1.1. Schematic of the band structure of an inorganic scintillator and the scintillation process at an extrinsic luminescent center.

1.3 Development of ceramic scintillators

Inorganic materials can be characterized by many important features but one of the most prominent ones is the degree of structural order. In that regard, two extreme groups can be emphasized: amorphous and crystalline materials. Crystalline materials can further be broken into two types, single crystals and polycrystalline ceramics. A perfect single crystal possesses translational symmetry and no internal interfaces, while polycrystalline ceramics are essentially

an arrangement of small single crystals (grains) that are randomly oriented throughout the material and separated by the grain boundaries [22].

Due to the high optical quality together with the development of photomultiplier tube (PMT) technology [23], single crystals began to be actively used as scintillators in the late 1940s with the introduction of NaI:Tl and CsI:Tl [24, 25]. Since that time, a large number of single crystals with a variety of dopants have been reported for scintillation applications [26, 27]. However, despite the great performance of monocrystalline scintillators, it is challenging to grow bulk single crystals due to the high melting temperature, stoichiometry issues with the possible loss of volatile species, or chemical stability (e.g. hygroscopicity) [2, 27]. Moreover, not all compounds can be grown as bulk single crystals with reasonably large dimensions at an affordable manufacturing cost [2]. In some cases, the homogeneity of the activator cannot be successfully achieved. Meanwhile, polycrystalline ceramics offer a variety of advantages over single crystals, including easier fabrication of materials with high melting temperatures and faster and lower cost fabrication methods (due to the absence of melting of raw materials), higher homogeneity of the dopant distribution, and greater post-fabrication shape control (due to the polycrystalline nature). Therefore, polycrystalline ceramics have been under development as an alternative to single crystals. The technology of optical (transparent or translucent) polycrystalline ceramics was developed in the 1960s for lighting applications [28, 29], and was further expanded in the 1990s, when Nd-doped $Y_3Al_5O_{12}$ (YAG) polycrystalline ceramics began to be used in solid-state laser optics instead of single crystals due to comparable properties and lower manufacturing cost [30, 31]. Development of scintillating polycrystalline ceramics started in the 1980s and was driven by demands of computed tomography (CT) for medical imaging [32, 33]. The first scintillating ceramics were simultaneously created by Hitachi Ltd. [33, 34],

developing $Gd_2O_2S_2$:Pr,Ce,F for X-ray CT detectors, and by General Electric Corporation [13, 35], when $(Y,Gd)_2O_3$:Eu was introduced, tailored-made for high performance medical detectors. As a result, in the early 1990s research was focused on manufacturing and characterizing $(Y,Gd)_2O_3$:Eu, Gd_2O_2S:Pr,Ce,F as well as, $Gd_3Ga_5O_{12}$:Cr,Ce polycrystalline ceramics [36]. It is important to notice that the scintillation time response of these ceramics was in the microsecond-to-millisecond time scale, which is relatively slow for scintillators. Thus, in order to satisfy demands for scintillators with nanosecond response time, research focus turned to the family of Ce^{3+} and Pr^{3+} activated garnet-based materials.

1.4 Development of garnet scintillators

One of the most investigated representatives of the garnet family is yttrium aluminum garnet ($Y_3Al_5O_{12}$ or YAG) doped with Ce^{3+}. This luminescent material has an intense research history and a wide variety of applications. The first reference to the crystal structure analysis of $Y_3Al_5O_{12}$ goes back to the 1928 review on the structures of rare earth aluminum garnets, where the crystallographic structure of YAG and other rare earth aluminum garnets was established as the body centered cubic lattice with space group symmetry *Ia3d* [37]. In the 1960s, it has been proposed to use this garnet as a new phosphor for flying-spot cathode ray tubes due to its short decay time and high luminescence efficiency [38, 39]. An early study of the Ce^{3+} fluorescence decay kinetics in the YAG matrix [40] showed the appearance of thermal quenching only at ca. 550 K. Consequently, at room temperature the $5d \rightarrow 4f$ transition of Ce^{3+} center showed a potential for fast and efficient scintillation in the YAG host. By the end of the 1970s, the important aspects of the luminescence properties and luminescence quenching of Ce^{3+} in YAG were published [41, 42], and a detailed description of YAG:Ce single crystals was reported: it has relatively low density and effective atomic number (*i.e.* weighted average of the atomic

numbers of the elements in the compound; ρ = 4.56 g/cm^3, Z_{eff} = 32.0) but exhibits high light yield (20000-28000 photons/MeV), short decay time (90-100 ns) [27, 43], and good energy resolution of 6-7 % at 662 keV [27]. The mentioned properties (short decay time and high light yield) together with peak emission at 550 nm made this material suitable for use as detectors in scanning electron microscopes (SEM) [44] and as yellow-green emitting scintillators for potential applications of high-energy physics [43, 45]. Since this material showed a long wavelength excitation band peaked at ca. 460 nm, it also received some attention as an absorber of mercury-plasma lines in the blue/violet region of the spectrum in low-pressure Hg-vapor discharge lamps [46]. At the beginning of the 21st century, YAG:Ce received renewed interest as a material for luminescent imaging screens [47-49], including cathodoluminescent (CL) imaging screens in transmission electron microscopes (TEM) [50], due to the well-defined optical properties, such as homogeneity of the CL emission, and the possibilities of quite precise and even complex shaping. Most recently, attention was brought to the material as a suitable phosphor for white-light emitting LED sources, where part of the blue light from the LED is absorbed by YAG:Ce and converted into yellow light, and the combination of blue and yellow gives a bright white light source [51, 52].

The garnet structure appears very flexible for cation substitution [53], which should, in principle, favor the preparation of YAG:Ce crystals with homogeneous cerium distribution as Ce^{3+} substitutes for the Y^{3+} cation. However, the same feature also results in easier compositional defect formation, and small fractions of Ce and Y can be found at antisite positions, switching places with aluminum (Ce_{Al} and Y_{Al}). Only in the mid-2000s were these defects reported to be present in YAG single crystal due to the high temperature required for growth of the crystals and are considered to be one of the main reasons for the lower-than-

theoretical light yield. Emission at ca. 300 nm and the dominant thermoluminescence peak at 92 K associated with shallow electron traps were related to Y_{Al} antisite defects [54, 55], and Ce_{Al} has been predicted to have the second lowest formation energy after Y_{Al} based on atomic scale simulation techniques [56].

In the late 1990s, polycrystalline ceramic YAG:Ce was reported for the first time [57, 58], and further research and development improved the quality and performance of the ceramic, making it increasingly comparable with the single crystal analogy. It was confirmed that Y_{Al} antisite defects are of very low concentration in the polycrystalline structure due to the absence of the melting of raw materials and lower preparation temperatures [59]. On the other hand, the light output from the Ce^{3+}-doped polycrystalline YAG was noticeably lower (ca. 30-40 %) than in the case of the single crystal. The reasons for such behavior are not known but it was proposed that lower light output can be caused by the deep traps at the surface and interface of the grains in the polycrystalline ceramic [59]. Some improvements in the light yield were made in the mid-2000s, when it was shown that the fabrication of YAG:Ce polycrystalline ceramics with luminosity similar to that of the single crystals was possible [60, 61]. However, authors report unknown cerium concentration in the single crystal. Thereby, observed improvement of the performance of the polycrystalline YAG:Ce relative to the single crystal can be simply related to the difference in the cerium content. A well-established procedure to make polycrystalline YAG:Ce with better scintillation performance than the monocrystalline analogy is still absent, while the reasons for the lower performance of the polycrystalline ceramic YAG:Ce are still unclear. Figure 1.2 illustrates the evolution of the luminosity of YAG:Ce polycrystalline ceramics since its first fabrication in 1997 [57, 58, 60-62] and is compared to the luminosity of single crystals [27, 43, 57, 58, 60, 61, 63]. It can be seen, that to the present time, the average

value of the most recent results for the light yield of single crystals is ca. 11% higher than those of the polycrystalline ceramic. In the present work, a comparative investigation of polycrystalline ceramic and single crystal $Y_3Al_5O_{12}$:Ce scintillators was conducted in order to gain a better understanding of the reasons influencing their scintillation performance.

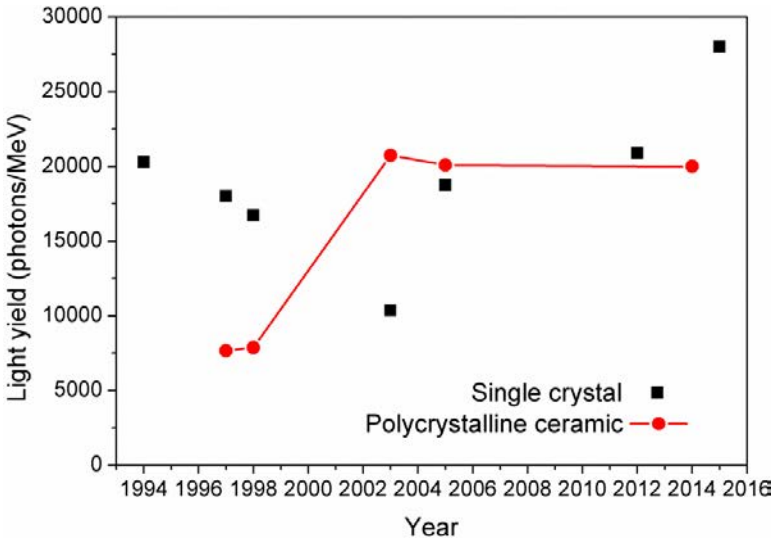

Figure 1.2. Evolution of the light yield of YAG:Ce single crystals and polycrystalline ceramics reported in the literature [27, 43, 57, 58, 60-64].

Replacement of yttrium with lutetium in the garnet structure led to an isostructural compound $Lu_3Al_5O_{12}$ (LuAG). Lutetium aluminum garnet exhibits the same crystallographic structure as YAG [37] but contains a heavier ion, Lu^{3+}, instead of Y^{3+} resulting in higher density and effective atomic number (ρ = 6.67 g/cm^3, Z_{eff} = 63.0) [65], which is advantageous for the scintillators in the case of X- and γ-ray detection. As a result, LuAG:Ce was more intensely studied for scintillation applications than YAG:Ce. Originally, LuAG attracted attention as a potential material for laser applications and, as early as the late 1960's, Ce-doped LuAG was investigated as a fluorescent material for the aforementioned applications [66]. It was shown that

the Ce^{3+} ions in the LuAG matrix exhibit a broad emission band centered around 525 nm at room temperature and that at low temperature (77 K) fluorescent spectra can be resolved into two components, which corresponds to the splitting of 4*f* energy levels of the Ce^{3+} ions due to the influence of the host crystal field. This phenomenon is common for scintillators doped with Ce^{3+}, such as LuAG and YAG. However, this material had not been explored as a potential scintillator until the 1990s, when applications using ionizing radiation (high energy physics, medical imaging, security) demanded discovery of new scintillation materials with a fast response time. Investigation of LuAG:Ce single crystals showed that this material had a decay constant of 60-70 ns [67], which is faster than YAG:Ce but appeared to be significantly slower than the analogous cubic perovskite $LuAlO_3$:Ce (LuAP:Ce) with the response time of 18 ns and even higher density of 8.4 g/cm^3 [67, 68]. As a result, research focus was mainly directed towards the investigation of faster and more dense LuAP:Ce crystals. However, by the end of 1990s, it was shown that fabrication of a pure LuAP single crystal has serious difficulties during crystal growth due to instability of the perovskite phase and often occurrence of the garnet phase. Moreover, Ce-doped LuAP showed a decrease in the light yield with increase of the sample size due to self-absorption [69, 70].

Consequently, by the beginning of the 2000s, the aforementioned undesirable features of LuAP:Ce resulted in the reinstatement of systematic studies of Ce-doped lutetium aluminum garnets for the detection of X- and γ-ray radiation [65]. It was shown that, besides the dominant decay component of about 50-55 ns, LuAG:Ce single crystal exhibits significant amount of light emission in the scintillation response with slow decay components of around 210 ns and 410 ns [65] (some sources even report this value up to 600-1000 ns [71]). Based on the thermoluminescence (TL) analysis at low temperatures (below room temperature), it was

suggested that point defects and their manifestation as electronic traps in the band gap of LuAG:Ce crystal resulted in significantly delayed energy transfer to the Ce^{3+} luminescent centers [59, 72]. Additionally, it was shown that the radiative electron-hole recombination around the antisite defects (AD) Lu_{Al} (Lu^{3+} ion at Al^{3+} lattice site) leads to a luminescence emission at 325 nm with decay time around 540 ns, which excites Ce^{3+} (excitation is a broad band centered around 340nm) and leads to the appearance of slow components in the overall decay in LuAG:Ce [73].

Attempts have been made to improve the performance of LuAG:Ce single crystals [74, 75] and, while individual reports showed high light output of 24000-26000 ph/MeV [75, 76], typically the value of the light yield for LuAG:Ce crystals has not exceeded 18000 ph/MeV (see Figure 1.3).

In the mid-2000s, first investigations of LuAG:Ce scintillation polycrystalline ceramics were reported [77, 78]. Initially, a solid-state reaction method was employed to synthesize the precursor powder, and cold isostatic pressing of powder compacts and a vacuum sintering technique were used to fabricate the polycrystalline ceramics [78]. The samples showed no secondary phase, 70-80 % transmittance, and 99.5 % of the theoretical density. This research was followed by a study of sol-gel combustion process [79] and a co-precipitation method [80] for the production of highly sinterable, nanosized LuAG:Ce precursor powders and further sintering of it into a polycrystalline ceramic. The specimen exhibited typical Ce^{3+} emission bands, corresponding to transitions from the lowest 5*d* excited state to the 4*f* ground state ($^2F_{5/2}$, $^2F_{7/2}$); however, polycrystalline ceramics had a more complicated microstructure due to presence of grains, grain boundaries, and residual pores, which significantly decreased the optical properties.

As a result, many studies were devoted to the development of new fabrication methods of LuAG:Ce transparent ceramics, including low-temperature vacuum sintering and solid-state reaction method using nanopowders, in order to increase optical transmittance through the improvement of the microstructure of the material [81, 82].

Additional investigations focused on improving the light yield of polycrystalline ceramics [77, 83-85]. It was shown that the fabrication of LuAG:Ce polycrystalline ceramics with luminosity similar to that of single crystals is possible [83]; however, typically it is 50-70 % of that of the single crystals [74, 76, 77, 85, 86]. Figure 1.3 illustrates the evolution of the luminosity of LuAG:Ce polycrystalline ceramics since its first fabrication in 2005 together with that of single crystals [74, 76, 77, 83-85, 87-90].

Recently, an investigation comparing a LuAG:Ce single crystal with polycrystalline ceramics prepared in different ways was reported [77]. They showed that, even though fastest decay time is similar (55 ns and 59 ns for the polycrystal and single crystal, respectively) and polycrystalline ceramic has higher radioluminescence (RL) intensity, the light yield measured within a shaping time of 1 μs is about 50 % lower with respect to the single crystal which also leads to a lower energy resolution (16.2 % and 11.0 % at 511 keV for the ceramic and the crystal, respectively). This means that at least half of the generated light is emitted at times longer than 1 μs. This result was interpreted as due to a larger number of deeper electronic traps in the polycrystalline material. Interestingly, TL measurements of the polycrystalline ceramic with lower light yield suggested the absence of Lu_{Al} antisite defects due to the absence of the typical structure of the glow-curves below 300 K, related to this type of defect. The reasons for the lesser performance of polycrystalline ceramics remained to be identified, and in this work a comparative investigation between a LuAG:Ce transparent polycrystalline ceramic and single

crystal scintillators was performed to gain insight into the factors influencing their scintillation performance.

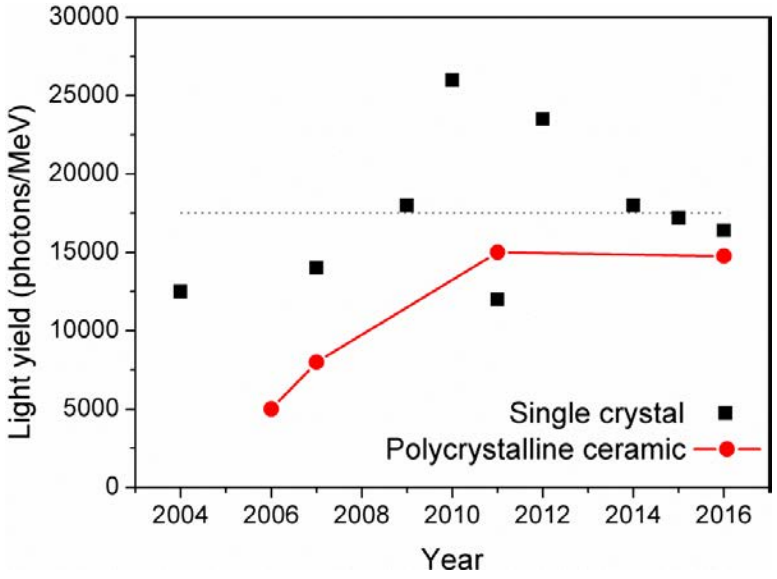

Figure 1.3. Evolution of the light yield of LuAG:Ce single crystals and polycrystalline ceramics reported in the literature [74, 76, 77, 83-85, 87-90]. The dotted line marks the average value of 17510 photons/MeV obtained for single crystals.

In 2005, the search for inorganic scintillators with a fast response led to the investigation of Pr^{3+}-doped LuAG single crystal [91]. The effort was done in order to obtain faster $5d \rightarrow 4f$ emission with regard to Ce^{3+} ions. It was discovered that Pr^{3+} doping in LuAG gives rise to a fast (ca. 20 ns) and intense $5d \rightarrow 4f$ emission peaking at 310 nm. Shorter decay times than in the case of LuAG:Ce can be achieved since $5d \rightarrow 4f$ emission of Pr^{3+} is characterized by a shorter wavelength compared to $5d \rightarrow 4f$ emission of Ce^{3+}. Shortly after its discovery, a detailed scintillation characterization of LuAG:Pr single crystals was reported [92]. The relatively high difference in ionic radius between Lu^{3+} and Pr^{3+} (more than 13 %) has been reported to limit the

incorporation of Pr in single crystals and to lead to considerable inhomogeneity of the dopant. The maximum of the concentration quenching curve has been found to be only 0.23 at.% in these crystals. However, it was confirmed that luminescence activation by means of the incorporation of Pr^{3+} ions substituting for Lu^{3+} leads to a fast scintillation decay time of about 20 ns and emission peak at 320 nm that closely matches the maximum detection efficiency of PMTs. The light yield of this scintillator has been reported to be 2 to 3 times higher than that of $Bi_4Ge_3O_{12}$ (BGO) single crystal. Furthermore, LuAG:Pr achieved outstanding temperature stability, where the onset of temperature quenching is located above 500 K [93].

In comparison to the Ce-doped LuAG, a slightly lower light yield of 16000-20000 ph/MeV was achieved for LuAG:Pr [94, 95]; however, it was determined that the energy resolution and linearity of the energy response (absence of non-proportionality) are improved and found to be one of the smallest among the high-performance complex oxide scintillators [96, 97]. The best value of energy resolution was found to be 4.6 % compared to 5.5 % at 662 keV in the case of LuAG:Ce [97].

The first report about a transparent polycrystalline ceramic LuAG:Pr was published in 2009 [98]. The ceramic sample reached a high transparency of 70 % above 310 nm, which matched closely to the results of the single crystal, and both of them showed similar emission spectra. However, the polycrystalline ceramic sample had about 2.5 times lower light yield and only 12 % energy resolution compared to 4.6 % for the single crystal at 662 keV. Following this investigation, research was focused on improving the properties of the ceramic material, eventually showing the decay time of the LuAG:Pr ceramic comparable to that of the single crystals [99], and the onset of the concentration quenching at about 1.0 at.% of Pr^{3+} for the polycrystalline LuAG:Pr ceramic, which is much higher than 0.23 at.% for LuAG:Pr single

crystals [100]. It was also shown that too high of a temperature for the typical annealing treatment of LuAG:Pr ceramics to reinstate oxygen stoichiometry after the hot isostatic pressing (HIP) potentially causes a transport and aggregation of nanometer pores into bigger clusters which significantly decreases optical properties of the material [101].

Nevertheless, the light yield and energy resolution were still below the corresponding values for the single crystal analogy. Light yield of polycrystalline ceramics appeared to be about 30% lower than that of BGO and about 65% lower than that of LuAG:Pr single crystals. The energy resolution at 511 keV was 15% for LuAG:Pr ceramic, 15% for the BGO crystal and 5% for the LuAG:Pr crystal [102]. In the case of the single crystals, the degradation was typically related to antisite defects but, with the example of LuAG:Ce [77], it was stated that antisite defects are of very low concentration for the polycrystalline ceramics due to a lower fabrication temperature. However, TL revealed deeper electron traps in the ceramics, which were connected to the defects at grain boundaries. As a result, the retrapping of electrons at the structural defects leads to significant degradation of the yield and scintillation response.

Investigation of the deterioration of scintillation characteristics of the ceramics showed that the antisite defects have low concentration in the polycrystalline LuAG:Pr due to relatively low sintering temperatures [103]. Harmful effects of sintering aids in the garnet scintillation ceramics were also shown. These aids behave as impurities in the lattice, introducing local structural disorder due to radii differences with lattice ions, and can segregate at grain boundaries. As a result, they induce the creation of point defects, which affect the carrier migration to luminescent centers (step 3 in Figure 1.1) [103, 104].

Only very recently, the first LuAG:Pr transparent ceramic with higher light yield and lower energy resolution than the single crystal analog was fabricated [105]. Light yield was ca.

20% higher when compared to the single crystal under gamma excitation, and energy resolutions of 4.6 % and 5 % at 622 keV were found for the polycrystalline ceramic and single crystal LuAG:Pr samples, respectively. However, the characteristics of the single crystal used in the investigation were lower than previously reported, and better understanding of what aspects of the ceramic microstructure effect the material performance as a scintillator is still required.

Another important member of the garnet family of scintillators is the Ce- or Pr-doped multicomponent garnets. Multicomponent garnets have the general chemical formula $RE_3(Al,Me)_5O_{12}$, where RE is a rare-earth element such as Gd, Y, Lu or their mixture and Me is a metallic element such as Ga, which partially substitutes for Al [2]. Investigation of $Y_3(Al_{1-x},Ga_x)_5O_{12}$ and $Lu_3(Al_{1-x},Ga_x)_5O_{12}$ single crystals doped with Ce^{3+} and Pr^{3+} showed that the substitution of Al for Ga affects the conduction band of the material by lowering the bottom of this band, which results in a smaller band gap [106-108]. Therefore, it naturally suppresses the energy trapping effect of the antisite defects by immersing shallow traps into the conduction band [109, 110]. However the content of Ga above x = 0.4-0.6 is unfavorable for the light emission as the bottom of the host conduction band becomes low enough to include 5*d* level of Ce^{3+} or Pr^{3+} resulting in the absence of luminescence [37, 109]. On the other hand, the addition of a larger Gd^{3+} cation into the garnet structure (e.g. $(Gd,Y)_3(Ga,Al)_5O_{12}$:Ce and $(Gd,Lu)_3(Ga,Al)_5O_{12}$:Ce single crystals) lowers the position of $5d_1$ level due to the stronger crystalline field ensuring the presence of the emission from the luminescent centers [8, 107, 111]. Such manipulations with the composition yielded a single crystal with light yield of ca. 46000 ph/MeV and energy resolution of 4.9 % at 662 keV [112].

Following the research of the multicomponent garnet scintillators in the form of single crystals, investigation of the multicomponent polycrystalline ceramics was also performed. The

effort was invested into the study of the Ce-doped $(Gd,Y)_3(Ga,Al)_5O_{12}$ polycrystalline ceramic [19, 113, 114]. First, the possibility of manufacturing optically transparent $(Gd,Y)_3(Ga,Al)_5O_{12}$:Ce ceramics was reported [113], and later, these ceramics were improved to have higher scintillation performance with a light yield of 50000 ph/MeV and energy resolution of 4.5-4.8 % at 662 keV [19, 114], which are promising results for X- and γ-ray detectors. Very recently, the luminescence properties of $(Gd,Lu)_3(Ga,Al)_5O_{12}$:Ce powders were also reported and appeared to be similar to the single crystal analogy [115]. To the best of the author's knowledge, only one team reported investigation of $(Gd,Lu)_3(Ga,Al)_5O_{12}$:Ce in the form of polycrystalline ceramics [116, 117]. The work described here extended the multicomponent garnet polycrystalline ceramic investigation as reported in Chapter 3. Overall, it was shown that significant improvements were achieved in the fabrication and performance of the garnet polycrystalline ceramic scintillators. However, there is still limited knowledge of the reasons affecting the scintillation performance, and further investigation is required. The present work aims to understand the connection between the microstructural features and the scintillation performance of the garnet polycrystalline ceramic.

References

[1] P.A. Rodnyi, Physical Processes in Inorganic Scintillators, CRC Press, Boca Raton, USA, 1997.

[2] M. Nikl, T. Yanagida, H. Yagi, T. Yanagitani, E. Mihokova, A. Yoshikawa, Optical Ceramics for Fast Scintillator Materials, in: J.J.R. Rovira, M.S. Rubi (Eds.) Recent advances in ceramic materials research, Nova Science Publisher, New York, 2013, pp. 127-176.

[3] D.B. Williams, C.B. Carter, Transmission electron microscopy: a textbook for materials science, 2nd ed., Springer, 2009.

[4] J. Goldstein, D.E. Newbury, D.C. Joy, Scanning Electron Microscopy and X-Ray Microanalysis, 3rd ed., Kluwer Academic/Plenum Publishers, New York, 2003.

[5] A. Yoshikawa, T. Yanagida, K. Kamada, Y. Yokota, J. Pejchal, A. Yamaji, Y. Usuki, S. Yamamoto, M. Miyake, K. Kumagai, K. Sasaki, T.R. dos Santos, M. Baba, M. Ito, M. Takeda, N. Ohuchi, M. Nikl, Positron emission mammography using Pr:LuAG scintillator – Fusion of optical material study and systems engineering, Opt Mater, 32 (2010) 1294-1297.

[6] T. Yanagida, A. Yoshikawa, Y. Yokota, K. Kamada, Y. Usuki, S. Yamamoto, M. Miyake, M. Baba, K. Kumagai, K. Sasaki, M. Ito, N. Abe, Y. Fujimoto, S. Maeo, Y. Furuya, H. Tanaka, A. Fukabori, T.R.d. Santos, M. Takeda, N. Ohuchi, Development of Pr:LuAG Scintillator Array and Assembly for Positron Emission Mammography, IEEE T Nucl Sci, 57 (2010) 1492-1495.

[7] H. Sato, S. Ito, Y. Usuki, M. Miyake, K. Kumagai, M. Baba, M. Ito, S. Yamamoto, Evaluation and Development for Positron Emission Mammography based on Pr:LuAG Scintillator Crystals in: B. Yu (Ed.) IEEE NSS/MIC, Anaheim, CA, 2012, pp. 3537-3539.

[8] K. Kamada, T. Endo, K. Tsutumi, T. Yanagida, Y. Fujimoto, A. Fukabori, A. Yoshikawa, J. Pejchal, M. Nikl, Composition Engineering in Cerium-Doped $(Lu,Gd)_3(Ga,Al)_5O12$ Single-Crystal Scintillators, Cryst Growth Des, 11 (2011) 4484-4490.

[9] P. Lecoq, A. Annenkov, A. Gektin, M. Korzhik, C. Pedrini, Inorganic Scintillators for Detector Systems: Physical Principles and Crystal Engineering Springer, Heidelberg, Germany, 2006.

[10] W.W. Moses, Current trends in scintillator detectors and materials, Nucl Instrum Meth A, 487 (2002) 123-128.

[11] G. Blasse, Scintillator materials, Chem Mater, 6 (1994) 1465-1475.

[12] G.W. Ludwig, X-Ray Efficiency of Powder Phosphors, J Electrochem Soc, 118 (1971) 1152-1159.

[13] C. Greskovich, D. Cusano, R. Riedner, D. Hoffman, Ceramic scintillators for advance, medical X-ray detectors, Am Ceram Soc Bull, 71 (1992) 1120-1130.

[14] J.A. Mares, Y. Shi, M. Nikl, Y. Shen, Y. Pan, X. Feng, Scintillation properties of Pr^{3+}-doped optical ceramic and single crystals of $Lu_3Al_5O_{12}$, in: 11^{th} Europhysical Conference on Defects in Insulating Materials, IOP Publishing Ltd, , Pécs, Hungary, 2010.
[15] P. Anfre, C. Dujardin, J.M. Fourmigue, B. Hautefeuille, K. Lebbou, C. Pedrini, D. Perrodin, O. Tillement, Evaluation of Fiber-Shaped LYSO for Double Readout Gamma Photon Detection, IEEE T Nucl Sci, 54 (2007) 391-397.
[16] H. Leutz, Scintillating fibres, Nucl Instrum Meth A, 364 (1995) 422-448.
[17] G.F. Knoll, Radiation Detection and Measurement, 4th ed., John Wiley & Sons, Inc, Michigan, 2010.
[18] G.A. Bray, A simple efficient liquid scintillator for counting aqueous solutions in a liquid scintillation counter, Anal Biochem, 1 (1960) 279-285.
[19] N.J. Cherepy, S.A. Payne, B.W. Sturm, J.D. Kuntz, Z.M. Seeley, B.L. Rupert, R.D. Sanner, O.B. Drury, T.A. Hurst, S.E. Fisher, M. Groza, L. Matei, A. Burger, R. Hawrami, K.S. Shah, L.A. Boatner, Comparative Gamma Spectroscopy with SrI_2(Eu), GYGAG(Ce) and Bi-loaded Plastic Scintillators, in: IEEE NSS/MIC, IEEE, Knoxville, TN, 2010, pp. 1288-1291.
[20] A. Lempicki, A.J. Wojtowicz, E. Berman, Fundamental limits of scintillator performance, Nucl Instrum Meth A, 333 (1993) 304-311.
[21] S.W.S. McKeever, Thermoluminescence of Solids, Cambrige University Press, Cambrige, 1988.
[22] W.D.J. Callister, D.G. Rethwisch, Fundamentals of Materials Science & Engineering, 3rd ed., John Wiley & Sons, 2008.
[23] W.R. Leo, Techniques or Nuclear and Particle Physics Experiments, in, Springer, New York, 1994.
[24] W. Van Sciver, R. Hofstadter, Scintillations in Thallium-Activated CaI_2 and CsI, Phys Rev, 84 (1951) 1062-1063.
[25] R. Hofstadter, The Detection of Gamma-Rays with Thallium-Activated Sodium Iodide Crystals, Phys Rev, 75 (1949) 796-810.
[26] M.J. Weber, Inorganic scintillators: today and tomorrow, J Lumin, 100 (2002) 35-45.
[27] M. Nikl, A. Yoshikawa, Recent R&D Trends in Inorganic Single-Crystal Scintillator Materials for Radiation Detection Adv Opt Mater, 3 (2015) 463-481.
[28] G.C. Wei, Transparent ceramics for lighting, J Eur Ceram Soc, 29 (2009) 237-244.
[29] G.C. Wei, Transparent ceramic lamp envelope materials, J Phys D Appl Phys, 38 (2005) 3057.
[30] A. Ikesue, Y.L. Aung, Ceramic laser materials, Nat Photonics, 2 (2008) 721-727.
[31] A. Ikesue, T. Kinoshita, K. Kamata, K. Yoshida, Fabrication and Optical Properties of High-Performance Polycrystalline Nd:YAG Ceramics for Solid-State Lasers, J Am Ceram Soc, 78 (1995) 1033-1040.

[32] B.C. Grabmaier, W. Rossner, J. Leppert, Ceramic scintillators for X-Ray computed tomography, Phys Status Solidi A, 130 (1992) K183-K187.
[33] Y. Ito, H. Yamada, M. Yoshida, H. Fujii, G. Toda, H. Takeuchi, Y. Tsukuda, Hot isostatic presse Gd_2O_2S:Pr, Ce, F translucent scintillator ceramics for X-ray computed tomography detectors, Jpn J Appl Phys, 27 (1988) L1371-L1373.
[34] M. Yoshida, M. Nakagawa, H. Fujii, F. Kawaguchi, H. Yamada, Y. Ito, H. Takeuchi, T. Hayakawa, Y. Tsukuda, Application of Gd_2O_2S ceramic scintillator for x-ray solid-state detector in x-ray CT, Jpn J Appl Phys, 27 (1988) L1572-L1575.
[35] C. Greskovich, D. Cusano, F. DiBianca, Rare-earth-doped yttria-gadolinia ceramic scintillators, in: U.S. Patent (Ed.) №4571312, U.S.A., 1986.
[36] C. Greskovich, S. Duclos, Ceramic Scintillators, Annu Rev Mater Sci, 27 (1997) 69-88.
[37] G. Menzer, Die Kristallstruktur der Granate, Z Kristallogr, 69 (1928) 300-396.
[38] G. Blasse, A. Bril, Investigation of Some Ce^{3+}-Activated Phosphors, J Chem Phys, 47 (1967) 5139-5145.
[39] G. Blasse, A. Bril, A new phosphor for flying-spot cathode-ray tubes for color television: yellow-emitting $Y_3Al_5O_{12}$:Ce^{3+}, Appl Phys Lett, 11 (1967) 53-55.
[40] M.J. Weber, Nonradiative decay from 5d states of rare earths in crystals, Solid State Commun, 12 (1973) 741-744.
[41] D.J. Robbins, B. Cockayne, J.L. Glasper, B. Lent, The Temperature Dependence of Rare-Earth Activated Garnet Phosphors: I. Intensity and Lifetime Measurements on Undoped and Ce-Doped $Y_3Al_5O_{12}$, J. Electrochem. Soc., 126 (1979) 1213-1220.
[42] D.J. Robbins, B. Cockayne, J.L. Glasper, B. Lent, The Temperature Dependence of Rare-Earth Activated Garnet Phosphors: II . A Comparative Study of Ce^{3+}, Eu^{3+}, Tb^{3+}, and Gd^{3+} in $Y_3Al_5O_{12}$, J. Electrochem. Soc., 126 (1979) 1221-1228.
[43] M. Moszynski, T. Ludziewski, D. Wolski, W. Klamra, L.O. Norlin, Properties of the YAG:Ce scintillator, Nucl Instrum Meth A, 345 (1994) 461-467.
[44] R. Autrata, P. Schauer, J. Kuapil, A single crystal of YAG-new fast scintillator in SEM, J Phys E Sci Instrum, 11 (1978) 707-708.
[45] T. Ludziejewski, M. Moszyński, M. Kapusta, D. Wolski, W. Klamra, K. Moszyńska, Investigation of some scintillation properties of YAG:Ce crystals, Nucl Instrum Meth A, 398 (1997) 287-294.
[46] E.F. Wyner, A.J. Daigneault, Improved mercury lamp for low color temperature applications, J Illum Eng Soc, 9 (1980) 109-114.
[47] P. Schauer, J. Bok, Study of spatial resolution of YAG:Ce cathodoluminescent imaging screens, Nucl Instrum Meth B, 308 (2013) 68-73.
[48] J. Tous, J. Blazek, J. Zemlicka, J. Jakubek, Evaluation of a YAG:Ce scintillation crystal based CCD X-ray imaging detector with the Medipix2 detector, J Instrum, 6 (2011) 1-6.

[49] D. Cavouras, I. Kandarakis, D. Nikolopoulos, I. Kalatzis, G. Kagadis, N. Kalivas, A. Episkopakis, D. Linardatos, M. Roussou, E. Nirgianaki, D. Margetis, I. Valais, I. Sianoudis, K. Kourkoutas, N. Dimitropoulos, A. Louizi, C. Nomicos, G. Panayiotakis, Light emission efficiency and imaging performance of $Y_3Al_5O_{12}$:Ce (YAG:Ce) powder screens under diagnostic radiology conditions, Appl. Phys. B, 80 (2005) 923-933.
[50] G.Y. Fan, M.H. Ellisman, Digital imaging in transmission electron microscopy, J Microsc, 200 (2000) 1-13.
[51] V. Bachmann, C. Ronda, A. Meijerink, Temperature quenching of yellow Ce^{3+} luminescence in YAG:Ce, Chem Mater, 21 (2009) 2077-2084.
[52] N.C. George, A.J. Pell, G. Dantelle, K. Page, A. Llobet, M. Balasubramanian, G. Pintacuda, B.F. Chmelka, R. Seshadri, Local Environments of Dilute Activator Ions in the Solid-State Lighting Phosphor $Y_{3-x}Ce_xAl_5O_{12}$, Chem Mater, 25 (2013) 3979-3995.
[53] M. Nikl, A. Vedda, V. Laguta, Single-crystal scintillation materials, in: G. Dhanaraj, K.Byrappa, V.Prasad, M.Dudley (Eds.) Springer Handbook of Crystal Growth, Springer, Berlin Heidelberg, 2010, pp. 1663–1700.
[54] V. Babin, K. Blazek, A. Krasnikov, K. Nejezchleb, M. Nikl, T. Savikhina, S. Zazubovich, Luminescence of undoped LuAG and YAG crystals, Phys Status Solidi C, 2 (2005) 97-100.
[55] Y. Zorenko, Luminescence of isoelectronic impurities and antisite defects in garnets, Phys Status Solidi C, 2 (2005) 375-379.
[56] C.R. Stanek, K.J. McClellan, M.R. Levy, C. Milanese, R.W. Grimes, The effect of intrinsic defects on $RE_3Al_5O_{12}$ garnet scintillator performance, Nucl Instrum Meth A, 579 (2007) 27-30.
[57] E. Zych, C. Brecher, A.J. Wojtowicz, H. Lingertat, Luminescence properties of Ce-activated YAG optical ceramic scintillator materials, J Lumin, 75 (1997) 193-203.
[58] E. Zych, C. Brecher, H. Lingertat, Scintillation properties of YAG:Ce optical ceramics, Mater Sci Forum, 239-241 (1997) 257-260.
[59] E. Mihóková, M. Nikl, J.A. Mareš, A. Beitlerová, A. Vedda, K. Nejezchleb, K. Blažek, C. D'Ambrosio, Luminescence and scintillation properties of YAG:Ce single crystal and optical ceramics, J Lumin, 126 (2007) 77-80.
[60] H. Takahashi, T. Yanagida, D. Kasama, T. Ito, H. Niko, T. Yanagitani, H. Yagi, T. Shigeta, T. Ito, Comparative studies of YAG:Ce single/poly-crystal scintillators, in: S. Sugimoto (Ed.) KEK: Scint Cryst, High Energy Accelerator Research Organization, Tsukuba, Japan, 2003, pp. 105-110.
[61] T. Yanagida, H. Takahashi, T. Ito, D. Kasama, T. Enoto, M. Sato, S. Hirakuri, M. Kokubun, K. Makishima, T. Yanagitani, H. Yagi, T. Shigeta, Evaluation of properties of YAG:Ce ceramic scintillators, IEEE T Nucl Sci, 52 (2005) 1836-1841.

[62] T. Yanagida, K. Watanabe, Y. Fujimoto, A. Uritani, H. Yagi, T. Yanagitani, Scintillation properties of composite ceramic YAG and its capability on pulse shape descrimination, J Ceram Soc Jpn, 122 (2014) 1016-1019.
[63] J.A. Mares, M. Nikl, A. Beitlerova, P. Horodysky, K. Blazek, K. Bartos, C. D'Ambrosio, Scintillation Properties of Ce^{3+}- and Pr^{3+}-Doped LuAG, YAG and Mixed $Lu_x,Y_{1-x}AG$ Garnet Crystals, IEEE T Nucl Sci, 59 (2012) 2120-2125.
[64] M. Moszynski, M. Kapusta, M. Mayhugh, D. Wolski, S.O. Flyckt, Absolute light output of scintillators, IEEE T Nucl Sci, 44 (1997) 1052-1061.
[65] M. Nikl, E. Mihoková, J.A. Mareš, A. Vedda, M. Martini, K. Nejezchleb, K. Blažek, Traps and Timing Characteristics of LuAG:Ce^{3+} Scintillator, Phys Status Solidi A, 181 (2000) R10-R12.
[66] W.W. Holloway, M. Kestigian, On the fluorescence of cerium-activated garnet crystals, Phys Lett A, 25 (1967) 614 - 615.
[67] A. Lempicki, M.H. Randles, A.J. Wojtowicz, LuAlO3:Ce and other Aluminate Scintillators, IEEE T Nucl Sci, 42 (1995) 280-284.
[68] C.W.E. van Eijk, Inorganic scintillators in medical imaging, Phys Med Biol, 47 (2002) R85-106.
[69] J.A. Mareš, N. Čechová, M. Nikl, J. Kvapil, R. Krátký, J. Pospíšil, Cerium-doped $RE^{3+}AlO_3$ perovskite scintillators: Spectroscopy and radiation induced defects, J Alloy Compd, 275–277 (1998) 200-204.
[70] C. Dujardin, C. Pedrini, W. Blanc, J.C. Gâcon, J.C.v.t. Spijker, O.W.V. Frijns, C.W.E.v. Eijk, P. Dorenbos, R. Chen, A. Fremout, F. Tallouf, S. Tavernier, P. Bruyndonckx, A.G. Petrosyan, Optical and scintillation properties of large $LuAlO_3$:Ce^{3+} crystals, J Phys Condens Mat, 10 (1998) 3061.
[71] M. Nikl, J.A. Mares, N. Solovieva, J. Hybler, A. Voloshinovskii, K. Nejezchleb, K. Blazek, Energy transfer to the Ce^{3+} centers in $Lu_3Al_5O_{12}$:Ce scintillator, Phys Status Solidi A, 201 (2004) R41-R44.
[72] M. Nikl, E. Mihokova, J. Pejchal, A. Vedda, Y. Zorenko, K. Nejezchleb, The antisite Lu_{Al} defect-related trap in $Lu_3Al_5O_{12}$:Ce single crystal, Phys Status Solidi B, 242 (2005) R119–R121.
[73] Y. Zorenko, A. Voloshinovskii, I. Konstankevych, V. Kolobanov, V. Mikhailin, D. Spassky, Luminescence of excitons and antisite defects in the phosphors based on garnet compounds, Radiat Meas, 38 (2004) 677-680.
[74] J.A. Mares, A. Beitlerova, M. Nikl, N. Solovieva, C. D'Ambrosio, K. Blazek, P. Maly, K. Nejezchleb, F. de Notaristefani, Scintillation response of Ce-doped or intrinsic scintillating crystals in the range up to 1 MeV, Radiat Meas, 38 (2004) 353-357.

[75] C. Dujardin, C. Mancini, D. Amans, G. Ledoux, D. Abler, E. Auffray, P. Lecoq, D. Perrodin, A. Petrosyan, K.L. Ovanesyan, LuAG:Ce fibers for high energy calorimetry, J Appl Phys, 108 (2010) 013510.
[76] A.G. Petrosyan, K.L. Ovanesyan, R.V. Sargsyan, G.O. Shirinyan, D. Abler, E. Auffray, P. Lecoq, C. Dujardin, C. Pedrini, Bridgman growth and site occupation in LuAG:Ce scintillator crystals, J Cryst Growth, 312 (2010) 3136-3142.
[77] M. Nikl, J.A. Mares, N. Solovieva, H.-L. Li, X.-J. Liu, L.-P. Huang, I. Fontana, M. Fasoli, A. Vedda, C. D'Ambrosio, Scintillation characteristics of $Lu_3Al_5O_{12}$:Ce optical ceramics, J Appl Phys, 101 (2007) 0335151-0335155.
[78] H.-L. Li, X.-J. Liu, L.-P. Huang, Fabrication of Transparent Cerium-Doped Lutetium Aluminum Garnet (LuAG:Ce) Ceramics by a Solid-State Reaction Method, J Am Ceram Soc, 88 (2005) 3226-3228.
[79] X.-J. Liu, H.-L. Li, R.-J. Xie, N. Hirosaki, X. Xu, L.-P. Huang, Cerium-doped lutetium aluminum garnet optically transparent ceramics fabricated by a sol-gel combustion process, J Mater Res, 21 (2006) 1519-1525.
[80] H.-L. Li, X.-J. Liu, R.-J. Xie, Y. Zeng, L. Ping Huang, Fabrication of Transparent Cerium-Doped Lutetium Aluminum Garnet Ceramics by Co-Precipitation Routes, J Am Cer Soc, 89 (2006) 2356-2358.
[81] J. Xu, Y. Shi, J. Xie, F. Lei, Fabrication, Microstructure, and Luminescent Properties of Ce^{3+}-Doped $Lu_3Al_5O_{12}$ (Ce:LuAG) Transparent Ceramics by Low-Temperature Vacuum Sintering, J Am Ceram Soc, 96 (2013) 1930-1936.
[82] J. Li, J. Xu, Y. Shi, H. Qi, J. Xie, F. Lei, Fabrication and microstructure of cerium doped lutetium aluminum garnet (Ce:LuAG) transparent ceramics by solid-state reaction method, Mater Res Bull, 55 (2014) 161-167.
[83] T. Yanagida, Y. Fujimoto, Y. Yokota, K. Kamada, S. Yanagida, A. Yoshikawa, H. Yagi, T. Yanagitani, Comparative study of transparent ceramic and single crystal Ce doped LuAG scintillators, Radiat Meas, 46 (2011) 1503-1505.
[84] S. Liu, X. Feng, J.A. Mares, V. Babin, M. Nikl, A. Beitlerova, Y. Shi, Y. Zeng, Y. Pan, C. D'Ambrosio, Y. Huang, Optical, luminescence and scintillation characteristics of non-stoichiometric LuAG:Ce ceramics, J Lumin, 169, Part A (2016) 72-77.
[85] G. Hull, J. Roberts, J. Kuntz, S. Fisher, R. Sanner, T. Tillotson, A. Drobshoff, S. Payne, N. Cherepy, Ce-doped single crystal and ceramic garnet for γ-ray detection, in: R.B. James, A. Burger, L.A. Franks (Eds.) Conference on Hard X-Ray and Gamma-Ray Detector Physics IX, SPIE, San Diego, CA, 2007, pp. 6706171-6706175.
[86] W. Chewpraditkul, L. Swiderski, M. Moszynski, T. Szczesniak, A. Syntfeld-Kazuch, C. Wanarak, P. Limsuwan, Scintillation Properties of LuAG:Ce, YAG:Ce and LYSO:Ce Crystals for Gamma-Ray Detection, IEEE T Nucl Sci, 56 (2009) 3800-3805.

[87] W. Chewpraditkul, L. Swiderski, M. Moszynski, T. Szczesniak, A. Syntfeld-Kazuch, C. Wanarak, P. Limsuwan, Comparative studies of $Lu_3Al_5O_{12}$:Ce and $Y_3Al_5O_{12}$:Ce scintillators for gamma-ray detection, Phys Status Solidi A, 206 (2009) 2599-2605.
[88] J.A. Mares, M. Nikl, A. Beitlerova, P. Horodysky, K. Blazek, K. Bartos, C. D'Ambrosio, Scintillation Properties of Ce^{3+} and Pr^{3+}-Doped LuAG, YAG and Mixed $Lu_{(x)}Y_{(1-x)}AG$ Garnet Crystals, IEEE T Nucl Sci, 59 (2012) 2120-2125.
[89] K. Kamada, M. Nikl, S. Kurosawa, A. Beitlerova, A. Nagura, Y. Shoji, J. Pejchal, Y. Ohashi, Y. Yokota, A. Yoshikawa, Co-doping effects on luminescence and scintillation properties of Ce doped $Lu_3Al_5O_{12}$ scintillator, Nucl Instrum Meth A, 782 (2015) 9-12.
[90] S. Liu, X. Feng, Z. Zhou, M. Nikl, Y. Shi, Y. Pan, Effect of Mg^{2+} co-doping on the scintillation performance of LuAG:Ce ceramics, Phys Status Solidi-R, 8 (2014) 105-109.
[91] M. Nikl, H. Ogino, A. Krasnikov, A. Beitlerova, A. Yoshikawa, T. Fukuda, Photo-and radioluminescence of Pr-doped $Lu_3Al_5O_{12}$ single crystal, Phys Status Solidi A, 202 (2005) R4–R6.
[92] H. Ogino, A. Yoshikawa, M. Nikl, K. Kamada, T. Fukuda, Scintillation characteristics of Pr-doped $Lu_3Al_5O_{12}$ single crystals, J Cryst Growth, 292 (2006) 239-242.
[93] J. Pejchal, M. Nikl, E. Mihóková, J.A. Mareš, A. Yoshikawa, H. Ogino, K.M. Schillemat, A. Krasnikov, A. Vedda, K. Nejezchleb, V. Múčka, Pr^{3+}-doped complex oxide single crystal scintillators, J Phys D Appl Phys, 42 (2009) 055117.
[94] W. Drozdowski, P. Dorenbos, J.T.M. de Haas, R. Drozdowska, A. Owens, K. Kamada, K. Tsutsumi, Y. Usuki, T. Yanagida, A. Yoshikawa, Scintillation Properties of Praseodymium Activated $Lu_3Al_5O_{12}$ Single Crystals, IEEE T Nucl Sci, 55 (2008) 2420-2424.
[95] L. Swiderski, M. Moszynski, A. Nassalski, A. Syntfeld-Kazuch, T. Szczesniak, K. Kamada, K. Tsutsumi, Y. Usuki, T. Yanagida, A. Yoshikawa, W. Chewpraditkul, M. Pomorski, Scintillation Properties of Praseodymium Doped LuAG Scintillator Compared to Cerium Doped LuAG, LSO and LaBr3, IEEE T Nucl Sci, 56 (2009) 2499-2505.
[96] W. Chewpraditkul, K. Sreebunpeng, M. Nikl, J.A. Mares, K. Nejezchleb, A. Phunpueok, C. Wanarak, Comparison of $Lu_3Al_5O_{12}$:Pr^{3+} and $Bi_4Ge_3O_{12}$ scintillators for gamma-ray detection, Radiat Meas, 47 (2012) 1-5.
[97] I.V. Khodyuk, J.T.M. de Haas, P. Dorenbos, Nonproportional response between 0.1-100 keV energy by means of highly monochromatic synchrotron X-rays, IEEE T Nucl Sci, 57 (2010) 1175-1181.
[98] T. Yanagida, A. Yoshikawa, A. Ikesue, K. Kamada, Y. Yokota, Basic Properties of Ceramic Pr:LuAG Scintillators, IEEE T Nucl Sci, 56 (2009) 2955 - 2959.
[99] Y. Shi, X.Q. Feng, Y.B. Pan, J. Zhou, Y. Huang, Z.H. Gao, Fabrication and photoluminescence characteristic of Pr:LuAG scintillator ceramics, Radiat Meas, 45 (2010) 457-460.

[100] J. Zhao, Z. Wang, C. Wang, X. Wei, Y. Li, W. Zhang, M. Yin, Synthesis and luminescent properties of Pr-doped $Lu_3Al_5O_{12}$ translucent ceramic, J Rare Earth, 27 (2009) 376-380.
[101] W.H. Rhodes, Y. Wang, C. Brecher, J. Gary Baldoni, Loss and Recovery of Transparency in Pressure-Consolidated $Lu_3Al_5O_{12}$, J Am Ceram Soc, 94 (2011) 3655-3658.
[102] Y. Shi, M. Nikl, X. Feng, J.A. Mares, Y. Shen, A. Beitlerova, R. Kucerkova, Y. Pan, Q. Liu, Microstructure, optical, and scintillation characteristics of Pr^{3+} doped $Lu_3Al_5O_{12}$ optical ceramics, J Appl Phys, 109 (2011) -.
[103] Y. Shen, Y. Shi, X. Feng, Y. Pan, J. Li, Y. Zeng, M. Nikl, A. Krasnikov, A. Vedda, F. Moretti, The Harmful effects of sintering aids in Pr:LuAG optical ceramic scintillator, J Am Ceram Soc, 95 (2012) 2130-2132.
[104] Y. Shen, X. Feng, V. Babin, M. Nikl, A. Vedda, F. Moretti, E. Dell'Orto, Y. Pan, J. Li, Y. Zeng, Fabrication and scintillation properties of highly transparent Pr:LuAG ceramics using Sc,La-based isovalent sintering aids, Ceram Int, 39 (2013) 5985-5990.
[105] T. Yanagida, Y. Fujimoto, K. Kamada, D. Totsuka, H. Yagi, T. Yanagitani, Y. Futami, S. Yanagida, S. Kurosawa, Y. Yokota, A. Yoshikawa, M. Nikl, Scintillation Properties of Transparent Ceramic Pr:LuAG for Different Pr Concentration, IEEE T Nucl Sci, 59 (2012) 2146-2151.
[106] P. Dorenbos, Electronic structure and optical properties of the lanthanide activated $RE_3(Al_{1-x}Ga_x)_5O_{12}$ (RE=Gd, Y, Lu) garnet compounds, J Lumin, 134 (2013) 310-318.
[107] S.K. Yadav, B.P. Uberuaga, M. Nikl, C. Jiang, C.R. Stanek, Band-Gap and Band-Edge Engineering of Multicomponent Garnet Scintillators from First Principles, Phys Rev Appl, 4 (2015) 0540121-0540129.
[108] M. Fasoli, A. Vedda, M. Nikl, C. Jiang, B.P. Uberuaga, D.A. Andersson, K.J. McClellan, C.R. Stanek, Band-gap engineering for removing shallow traps in rare-earth $Lu_3Al_5O_{12}$ garnet scintillators using Ga^{3+} doping, Phys Rev B, 84 (2011) 0811021-0811024.
[109] M. Nikl, E. Mihokova, J. Pejchal, A. Vedda, M. Fasoli, I. Fontana, V.V. Laguta, V. Babin, K. Nejezchleb, A. Yoshikawa, H. Ogino, G. Ren, Scintillator Materials - Achievements, Opportunities, and Puzzles, IEEE T Nucl Sci, 55 (2008) 1035-1041.
[110] M. Nikl, J. Pejchal, E. Mihokova, J.A. Mares, H. Ogino, A. Yoshikawa, T. Fukuda, A. Vedda, C. D'Ambrosio, Antisite defect-free $Lu_3(Ga_xAl_{1-x})_5O_{12}$:Pr scintillator, Appl Phys Lett, 88 (2006) 1419161-1419163.
[111] K. Kamada, T. Yanagida, J. Pejchal, M. Nikl, T. Endo, K. Tsutumi, Y. Fujimoto, A. Fukabori, A. Yoshikawa, Scintillator-oriented combinatorial search in Ce-doped $(Y,Gd)_3(Ga,Al)_5O_{12}$ multicomponent garnet compounds, J Phys D Appl Phys, 44 (2011) 5051041-5051048.

[112] K. Kamada, T. Yanagida, T. Endo, K. Tsutumi, Y. Usuki, M. Nikl, Y. Fujimoto, A. Fukabori, A. Yoshikawa, 2 inch diameter single crystal growth and scintillation properties of Ce:$Gd_3Al_2Ga_3O_{12}$, J Cryst Growth, 352 (2012) 88-90.
[113] N.J. Cherepy, J.D. Kuntz, Z.M. Seeley, S.E. Fisher, O.B. Drury, B.W. Sturm, T.A. Hurst, R.D. Sanner, J.J. Roberts, S.A. Payne, Transparent ceramic scintillators for gamma spectroscopy and radiography, in: A. Burger, L.A. Franks, R.B. James (Eds.) Conference on Hard X-Ray, Gamma-Ray and Neutron Detector Physics XII, SPIE, San Diego, CA, 2010, pp. 78050I-78050I-78055.
[114] N.J. Cherepy, S.A. Payne, B.W. Sturm, S.P. O'Neal, Z.M. Seeley, O.B. Drury, L.K. Haselhorst, B.L. Rupert, R.D. Sanner, P.A. Thelin, S.E. Fisher, R. Hawrami, K.S. Shah, A. Burger, J.O. Ramey, L.A. Boatner, Performance of europium-doped strontium iodide, transparent ceramics and bismuth-loaded polymer scintillators, in: L.A. Franks, R.B. James, A. Burger (Eds.) Conference on Hard X-Ray, Gamma-Ray and Neutron Detector Physics XIII, SPIE, San Diego, CA, 2011, pp. 814201-814208.
[115] J. Luo, Y. Wu, G. Zhang, H. Zhang, G. Ren, Composition–property relationships in $(Gd_{3-x}Lu_x)(Ga_yAl_{5-y})O_{12}$:Ce (x = 0, 1, 2, 3 and y = 0, 1, 2, 3, 4) multicomponent garnet scintillators, Opt Mater, 36 (2013) 476-481.
[116] Y. Wang, G. Baldoni, C. Brecher, W.H. Rhodes, U. Shirwadkar, J. Glodo, I. Shah, C. Ji, Properties of transparent $(Gd,Lu)_3(Al,Ga)_5O_{12}$:Ce ceramic with Mg, Ca and Ce co-dopants, in: H.B. Barber, L.R. Furenlid, H.N. Roehrig (Eds.) Medical Applications of Radiation Detectors V, SPIE, San Diego, CA, 2015, pp. 959401-959408.
[117] Y. Wang, G. Baldoni, W.H. Rhodes, C. Brecher, A. Shah, U. Shirwadkar, J. Glodo, N. Cherepy, S. Payne, Transparent garnet ceramic scintillators for gamma-ray detection, in: R.B. James, A. Burger, L.A. Franks, M.Fiederle (Eds.) Conference on Hard X-Ray and Gamma-Ray Detector Physics XIV, SPIE, San Diego, CA, 2012, pp. 8507171-8507178.

CHAPTER TWO

EXPERIMENTAL PROCEDURES

2.1 Materials

The following materials were investigated in the present work: $Y_3Al_5O_{12}$:Ce (YAG:Ce), $Lu_3Al_5O_{12}$:Ce (LuAG:Ce), $Lu_3Al_5O_{12}$:Pr (LuAG:Pr), $(Lu,Gd)_3(Al,Ga)_5O_{12}$:Ce (GLuGAG:Ce), and $Li_7La_3Zr_2O_{12}$:Ce (LLZO:Ce).

A Czochralski-grown polished YAG single crystal doped with 0.2 mol% of Ce^{3+} was purchased from MTI Corporation, Richmond, CA, as a 5 x 5 x 0.5 mm^3 plate. YAG:Ce polycrystalline ceramics were provided by Dr. Ronaldo S. da Silva, Federal University of Sergipe, Brazil. $Y_3Al_5O_{12}$:Ce precursor powder was prepared by the modified polymeric precursor method [1] using $Al(Cl_3)_3 \cdot 6H_2O$ (99 % purity), $Y(NO_3)_3 \cdot 6H_2O$ (99.8 %), and $CeH_8O_{18}N_8$ (99.99 %) as starting materials. Powders were calcined at 1000 °C for 6 hours and uniaxially pressed at 120 MPa into 4-mm-diameter, 1.2-mm-thick disk-shaped samples [2]. Sintering was done by the previously reported method of laser sintering [3-5]. Sintering was performed using a CO_2 laser (GEM-100L-Coherent) in continuous mode as the main heating source. The laser beam had a diameter of 5.2±0.5 mm and laser power density was up to 3.3 W/mm^2. Total laser sintering time was 11 min [2]. The YAG polycrystalline ceramic prepared this way had either 0.1 mol% or 0.3 mol% of Ce^{3+} in the samples. Polycrystalline samples were opaque and had dimensions of ca. $\varnothing$ 3.1 mm x 0.7 mm thick. Six samples of the polycrystalline ceramics with each Ce concentration were used.

The LuAG:Ce and LuAG:Pr single crystals were courtesy of Dr. Charles L. Melcher, University of Tennessee, Knoxville, TN and were grown by the Czochralski method using a 60 mm diameter, 60 mm tall iridium crucible that was inductively heated by an 8 kHz power supply.

Lu_2O_3, Al_2O_3, and CeO_2 (or Pr_6O_{11}) starting materials were at least 99.99 % pure, and the flowing atmosphere was nitrogen mixed with a small amount of oxygen (ca. 0.25 %) monitored continuously by a residual gas analyzer [6]. Polished LuAG:Ce (or Pr) crystals with nominal dopant concentration of 1 % and dimensions of 3.9 x 3.9 x 3.9 mm^3 were used in the present work. The transparent LuAG:Ce polycrystalline ceramic was fabricated by high temperature vacuum sintering with a nominal composition of $Lu_{2.985}Ce_{0.015}Al_5O_{12}$ (*i.e.*, nominal Ce concentration = 0.075 at.%). Precursor powders were prepared by the co-precipitation method using high purity (99.99 %) starting materials and tetraethyl orthosilicate (TEOS) as a sintering additive. Powders were calcined and uniaxially pressed at 10 MPa, and the pellet was heated at 400 ^oC, cold isostatically pressed, and sintered at 1800 ^oC for 10 hours. A polished transparent ceramic of LuAG:Ce with a 13.5 mm diameter and a 2.9 mm thickness was used in the present work. LuAG:Pr polycrystalline ceramics doped with 0.18 at.% of Pr (concentration determined by means of energy dispersive X-ray spectroscopy) were fabricated by high temperature sintering in air by Matthew R. Marchewka, a former graduate student in Dr. Jacobsohn's group. Precursor powders were prepared by the co-precipitation method using Lu_2O_3 (99.995 % purity), 70 % HNO_3, $Al(NO_3)_3$ (98 %), and $Pr(NO_3)_3 \cdot 6H_2O$ (99.9 %) as starting materials. Powder was calcined at 1000 °C for 2 hours and uniaxially pressed at 28 MPa for 45 sec. Obtained pellets with dimensions of ca. $\varnothing$ 10 mm x 1 mm thick were sintered in air at 1400 °C, 1500 °C, 1600 °C, or 1700 °C for 20 hours resulting in 4 different samples [7].

$(Lu_{3-x}, Gd_x)(Al_{0.6}, Ga_{0.4})_5O_{12}$ polycrystalline ceramics doped with 0.6 % of Ce^{3+} and various Gd to Lu ratios (x = 0, 0.15, 0.3, 0.9, 2.1, 3) were provided by Radiation Monitoring Devices, Inc., (RMD), Watertown, MA. The samples were sintered and some were also hot isostatically pressed (HIPed). The sample specifications can be seen in Table 2.1. Further details

of the sample preparation and treatment were not provided due to proprietary nature of the materials.

Table 2.1. Specifications of Ce-doped $(Lu_{3-x}, Gd_x)(Al_{0.6}, Ga_{0.4})_5O_{12}$ polycrystalline ceramics.

$(Lu_{3-x}, Gd_x)(Al_{0.6}, Ga_{0.4})_5O_{12}$:Ce polycrystalline ceramics				
Sample ID	[Gd] content (x value)	Thickness, mm	Diameter, mm	Treatment type
R12	0	2.43	9.62	Sintered only
R15	0.15	1.96	8.80	Sintered only
R16	0.3	1.97	9.24	Sintered only
R17	0.9	2.04	9.23	Sintered only
R26	2.1	1.64	8.84	Sintered + HIPed
R9	3	1.16	9.12	Sintered + HIPed

$Li_7(La_{1-x}Ce_x)_3Zr_2O_{12}$ (LLZO:Ce) was investigated in the form of powder synthesized via the solid state reaction method. Powders with a nominal composition of $Li_7(La_{1-x}Ce_x)_3Zr_2O_{12}$ with x = 0, 0.005, 0.01, 0.03, and 0.05 used the following starting materials: Li_2CO_3 (99.9 % purity), La_2O_3 (99.99 %), ZrO_2 (99.7 %), and $CeH_8N_7O_{15}{\cdot}4H_2O$ (reagent purity). The precursor powders were ball-milled for 24 hours using yttrium stabilized zirconia (YSZ) grinding balls, followed by calcination in sealed alumina crucibles at 950 °C for 5 hours in a box furnace. The ball-milling and calcination steps were repeated a total of 3 times for each sample [8].

2.2 Characterization techniques

2.2.1 X-ray diffraction (XRD)

Crystalline structures and phase purity of powders and ceramic bodies were investigated by means of X-ray powder diffractometry. The technique is based on generation of X-rays, their

interaction with the sample, and the collection of the diffracted rays. When X-ray beams incident on a crystalline solid are diffracted in-phase by the parallel crystallographic planes, as illustrated in Figure 2.1, constructive interference occurs and a peak in the diffraction pattern is observed. The deflected beams will be in-phase only when Bragg's law is satisfied [9]:

$$n\lambda = 2d\sin\theta \tag{2.1}$$

where n is an integer number, λ is the wavelength of incident X-ray, d is the spacing between crystal planes (A and B in Figure 2.1), and θ is the incident angle.

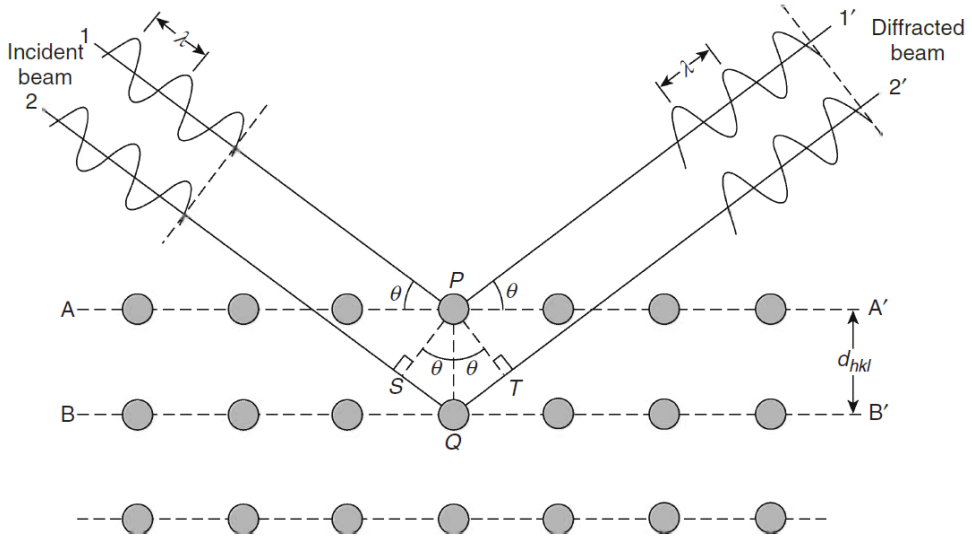

Figure 2.1. Bragg's relationship between incident and diffracted X-ray beams [10].

Bragg's law combined with experimental variation of the angle θ and detection of constructive interference at specific incident angles provide information about spacing between atomic planes of a crystal (d_{hkl} in Figure 2.1). Since all of the materials investigated in this work have cubic unit cell, plane spacing is related to the lattice parameter as:

$$d_{hkl} = \frac{a}{\sqrt{h^2 + k^2 + l^2}} \tag{2.2}$$

where a is a lattice parameter, and the Miller indices (hkl) represent a series of parallel planes with spacing of d_{hkl}.

Equation (2.2) in combination with equation (2.1) provides a relation between the lattice parameter and the incident angle for a given wavelength λ of X-rays. It is important to note that the wavelength of incident radiation must be comparable with the atomic spacing in order for diffraction to occur. This requirement explains the use of X-rays as incident electromagnetic waves as the atomic spacing typically falls within the X-ray wavelength range.

X-rays are generated by an X-ray tube, where high-energy electrons are accelerated from a filament into a metallic target. The target material is typically copper due to short wavelength of its characteristic X-rays which allows for a relatively large range of plane spacing values to be detected. As a result of the bombardment of copper with high-energy electrons, electrons from the inner K shells of the atoms of target material are removed, which results in the creation of holes. Electrons from outer L and M shells move to fill these holes, leading to the emission of characteristic K_α (λ = 1.542 Å) and K_β (λ = 1.392 Å) X-rays, respectively. To maximize the technique resolution, K_β X-rays are eliminated by a monochromater before the diffracted X-rays reach the detector. The K_α X-ray is composed of two separate characteristic X-rays: $K_{\alpha1}$ (λ = 1.541 Å) and $K_{\alpha2}$ (λ = 1.544 Å). These lines result from transitions between different subshells within the L shell and the K shell. As the wavelength difference between these two X-rays is only 0.003 Å, it is difficult to eliminate one of them without great reduction of beam intensity and, consequently, filtering of one of these K_α lines is rarely done. The emitted X-ray beam is collimated by thin slits which are comprised of closely spaced metal plates before irradiating the sample. The X-ray diffractogram is obtained by varying the incident angle θ of the X-ray beam onto the sample and simultaneously recording the diffraction intensity as a function of the diffraction angle 2θ. The collection of several diffraction peaks at specific values of 2θ creates a

unique pattern, which is the “fingerprint” of a material and contains the aforementioned information about its crystallographic structure [9].

In the present work, X-ray diffraction was obtained with a Rigaku Ultima IV X-ray diffractometer with Cu K_α radiation (40 kV, 40 mA) (see Figure 2.2). Samples were scanned over values of 2θ between 15° and 65° at a rate of 1 °/min with an angular resolution of 0.01° using unfiltered X-ray line with a dominant wavelength of 1.542 Å. Collected diffractograms were compared against powder diffraction files (PDFs) of corresponding materials obtained from PDXL: Integrated X-ray powder diffraction software using the ICDD (International Centre for Diffaction Data) database.

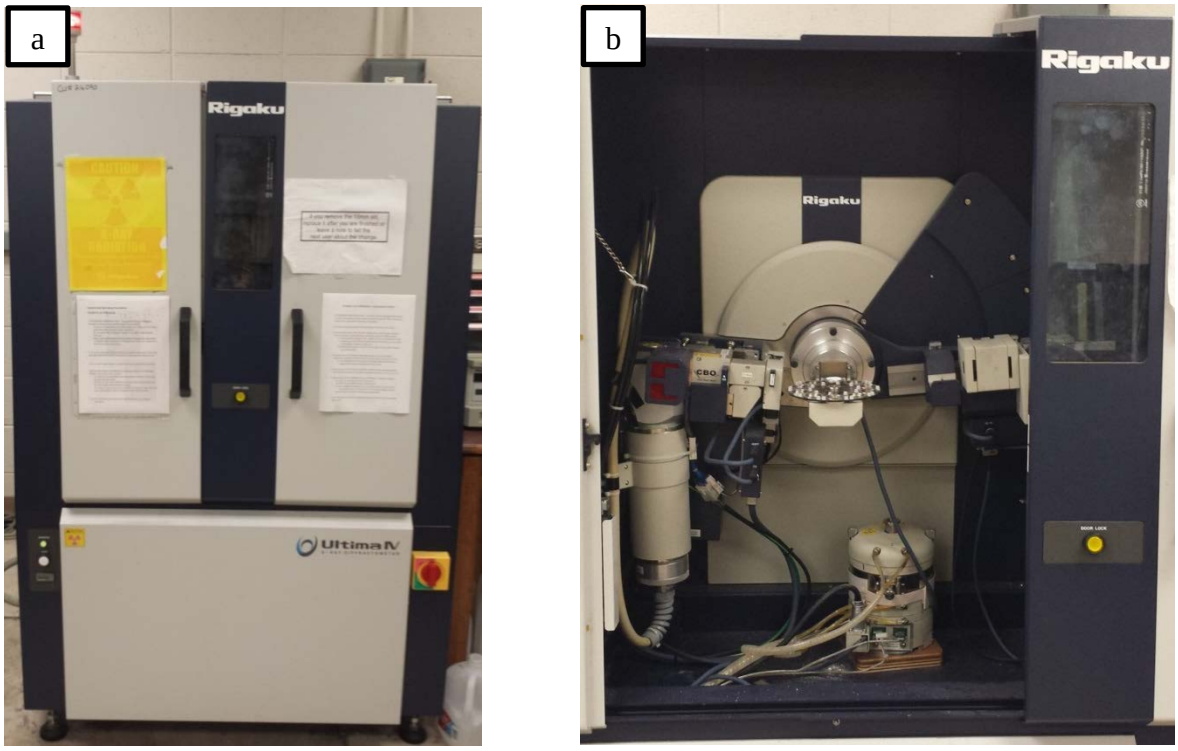

Figure 2.2. Rigaku Ultima IV X-ray diffractometer used to characterize crystalline structure. a) outside view; b) inside view (X-ray tube, detector, and sample rotary table can be seen).

2.2.2 Scanning electron microscopy (SEM)/energy dispersive X-ray spectroscopy (EDX)

Grain/particle morphology, grain size evaluation, and chemical composition of the investigated materials were analyzed by means of scanning electron microscopy in combination with energy dispersive X-ray spectroscopy (SEM/EDX).

As the name suggests, SEM examines microscopic characteristics of the material by scanning its surface using a focused beam of electrons. Use of electrons enables much higher magnification and resolution of an image than with conventional light microscopy due to the shorter wavelengths of the electrons (ca. 10,000 times shorter) than that of visible light.

A typical SEM is composed of an electron gun and several electromagnetic lenses and apertures (Figure 2.3a). The electron gun itself (Figure 2.3b) is composed of a cathode, anode, and a Wehnelt electrode placed between the cathode and anode. Electrons are emitted from the heated cathode and accelerated by an electric field towards the anode. The Wehnelt electrode is used for focusing and control of the electron beam [9].

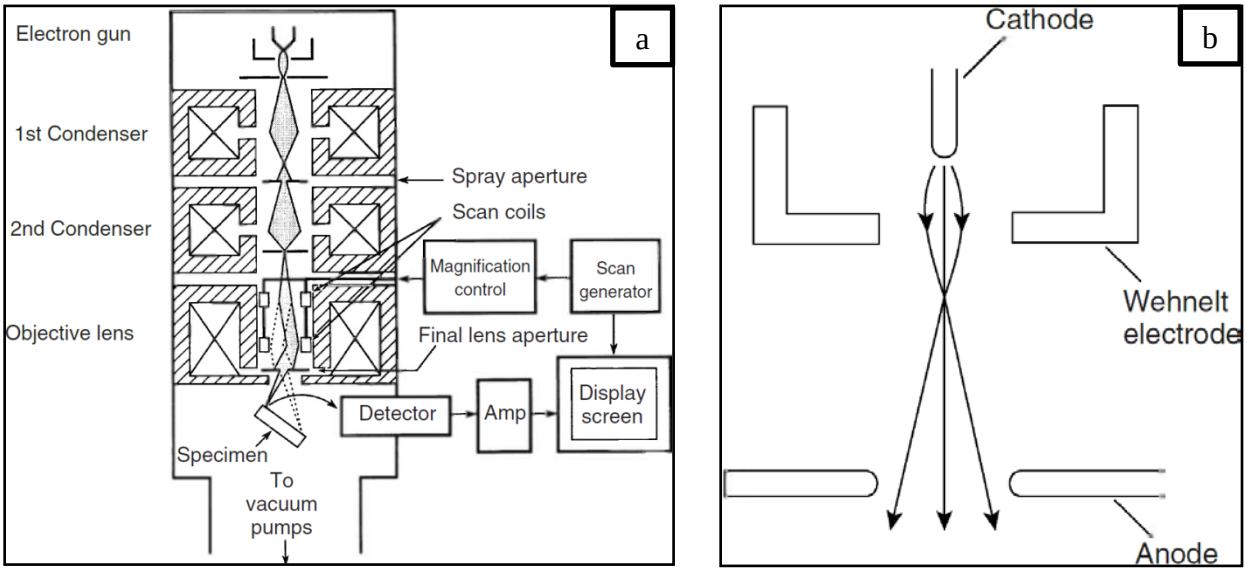

Figure 2.3. a) General structure of a SEM [11]; b) General structure of an electron gun [9].

The most common type of electron guns is the thermionic emission gun. Since the SEM used in this work was equipped with this type of electron gun, it is considered here in more detail. A tungsten filament used as a cathode in thermionic emission gun is heated by an electric current to allow for the electrons to achieve enough kinetic energy to leave the material. Tungsten is used due to its ability to withstand high temperatures for long periods of time without degrading. Free electrons that leave the filament are then accelerated from the cathode to the anode by a high electric voltage. The electric current (and thus the temperature of the tungsten filament) and the voltage used for the acceleration of the electrons determine the intensity of the beam. Further, the beam is deflected and focused by passing through a set of lenses. An electron microscope lens corresponds to the electromagnetic field generated by an electric current passing through a solenoid. The use of electromagnetic lenses allows the magnification to be easily changed by altering the electric current running through the solenoid. The generated field controls the beam diameter and the angle that the beam converges on the surface of the sample. In addition, a scanning electron microscope usually contains two condenser lenses to reduce the diameter of the electron beam together with a final objective lens to focus the beam to nanometer scale diameter (Figure 2.3a). This process leads to a focused beam of electrons that act as a fine probe of the surface of the material. Finally, the beam is deflected by the objective lenses to scan across the surface of the material, while the signal electrons are detected, amplified, and then reconstructed into the surface image [11].

Two types of signal electrons are used in SEM: backscattered electrons (BSEs) and secondary electrons (SEs). Both of these are generated from the collisions of incident electrons with the specimen. Backscattered electrons are generated through elastic scattering leading to high scattering angles. On the other hand, secondary electrons are generated as a result of an

inelastic scattering when incident electrons collide with the electrons bound to the atoms of the specimen and eject them from their orbitals. Electrons that leave the specimen with energies up to 50 eV are considered SE and those with energies above 50 eV are BSE. As a result, BSEs are most useful for volumetric and elemental composition analysis, while SEs are useful for collecting topographical information [9]. As a last step, signal electrons (either BSEs or SEs) are converted to UV-visible photons by the use of the scintillators. Photons are then converted to an electrical signal by a photomultiplier tube or photodiode, and the result is displayed on the screen (Figure 2.4a). Common scintillators used for electron microscopy are $Y_3Al_5O_{12}$:Ce (YAG:Ce), Y_2SiO_5:Ce (YSO:Ce), and $YAlO_3$:Ce (YAP:Ce) [12].

A Hitachi S-3400 Variable Pressure-SEM (VP-SEM) microscope was used to characterize materials investigated in the present work. Samples were mounted on an aluminum multi-sample holder with carbon tape. The holder with the samples was placed into the vacuum chamber and sealed with vacuum of 30 Pa. A working distance of 10 mm and accelerating voltage of 20 kV were used. Images of the specimen were collected at different magnifications depending on the grain sizes.

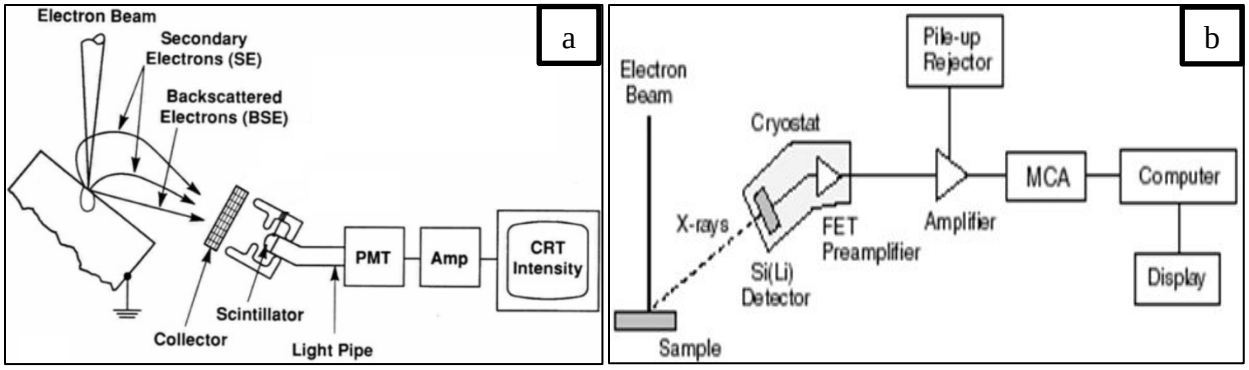

Figure 2.4. a) Electron detection in SEM; b) Schematic of EDX in an SEM [11]

Average grain size was determined using the lineal intercept method from SEM images following ASTM E 112-96. According to the tetrakaidecahedron-shaped model [13], the average grain size can be calculated as

$$\overline{D} = 1.571\frac{C}{N} \tag{2.3}$$

where $\overline{D}$ is the average grain size, C is the measuring line length in μm (based on the scale of SEM image), and N is the number of grains intercepted by the measuring line. Ten horizontal straight lines were drawn at random in each image recorded from different locations on the sample surface, all with the same magnification. A total of ca. 300 intercepts of the measuring lines with the grain boundaries were counted for each sample, and average intercept number was determined. The average intercept number was converted into length using the scale of the SEM image and then multiplied by the factor 1.571.

In addition to the aforementioned analysis, an SEM system can be used to obtain elemental composition information about the specimen by equipping it with an energy-dispersive X-ray spectrometer (EDX). When a specimen is bombarded by a high-energy electron beam, electrons from the beam will eject the inner shell electron of a specimen atom leaving a hole

behind. An outer shell electron will move to fill this hole releasing its energy in the a form of an X-ray photon with energy equal to the energy difference of the two shells, which is a characteristic of an element (hence the name “characteristic X-rays”). As the energy of the emitted X-ray is well known and different for each element, measurement of the energy and intensity of the X-rays emitted by the sample can be used to identify and quantify the elements which compose the specimen.

In the SEM, as it is shown in Figure 2.4b, the electron beam is aligned with the vertical axis of the microscope so that the detector has to be placed at a certain angle from the vertical. A lithium-drifted silicon detector, or Si(Li) diode, is commonly used in EDX systems. This detector operates at low temperature using liquid nitrogen to reduce the amount of noise (Figure 2.4b); therefore, improving the energy resolution which is typically in the range of 150-200 eV [14]. When characteristic X-rays reach the detector, they generate electron-hole (e-h) pairs in the detector material with energies at approximately 3.8 eV, which is the required energy to create e-h pair in Si(Li) diode. The external voltage applied to the Si(Li) diode separates the electron from the hole towards opposing electrodes thus generating an electrical signal. Higher-energy characteristic X-rays will generate more e-h pairs than lower-energy ones, thus, allowing a separation of characteristic X-rays by the number of pairs created and identification of the elements of the specimen.

In the present work, EDX measurements were done together with SEM imaging as discussed earlier. Area scans were performed at random locations of the specimen using the Oxford software AZtec version 2.2 with results reflecting the average of five scans on each sample. The main goal was to determine the true concentration of the dopant (Ce or Pr) and Gd/Lu ratios in the multicomponent garnets. Typically, acquisition time of 30-60 sec is sufficient

to detect the elemental composition of a specimen. However, as detection of elements depends on the signal-to-noise ratio, longer collection times were required to detect trace elements (*e.g.*, acquisition times of 600-900 sec were necessary to detect the concentration of the dopants in the samples (less than 1 at%)). Even with longer collection times, if the dopant concentration is less than 0.05 at%, it was not detected with reasonable certainty.

2.2.3 Density measurements

An important parameter for the scintillating polycrystalline ceramics is the density. Polycrystalline ceramics might contain pores which are essentially pockets of air that reduce the average density. The presence of air changes the local index of refraction relative to the bulk material and acts as effective scattering centers negatively affecting optical transparency and detection efficiency in general. One simple but efficient method of measuring density is through application of Archimedes principle.

The basis of the Archimedes principle is that an object immersed in a fluid will experience a buoyant force equal to the weight of the liquid displaced. The buoyancy force is a result of the pressure applied by the liquid against the object, where the magnitude of the pressure depends on the surface area of an object. Thus, two objects with the same mass but different volumes will experience different buoyancy forces. This means that the density of a material will affect the pressure it experiences when immersed in a liquid [15]. Measuring the difference in weight of a material in a liquid with known density is the basis of using Archimedes principle to determine the density of studied object.

In the present work, polycrystalline ceramics were saturated with water by submerging them under vacuum obtained with a mechanical vacuum pump in ultrapure water for 24 hours to evacuate any gas from pores in the material before being weighed. A comparison of the mass of

the ceramic saturated with water, M_{sat}, versus oven dried, M_{dry}, yields the density of the sample through the relation:

$$\rho_{sample} = \rho_{water} \frac{M_{dry}}{M_{sat} - M_{immersed}} \tag{2.4}$$

where $M_{immersed}$ is the mass of the sample immersed in water, measured on the Archimedes density platform (Figure 2.5). The average density value reflects five separate measurements for each polycrystalline sample and are performed by M. Marchewka as part of his Master of Science (MSc) thesis.

Figure 2.5. Universal specific gravity kit, bench model SGK-B.

2.2.4 Attenuated total reflectance Fourier transform infrared spectroscopy (ATR FTIR)

ATR FTIR is a vibrational spectroscopic technique that detects molecular vibrations through the absorption of infrared light. For temperatures above absolute zero, molecules in solids will constantly vibrate at certain frequencies. As a result, when the energy of infrared light irradiating the specimen matches the vibrational energies of the molecules, these molecules will absorb the infrared light, with the frequency pattern of absorption depending on the chemical composition and structural arrangement of the material [9, 16]. In the case of FTIR, use of the Fourier transform method allows for the collection of signal in a wide range of frequencies simultaneously [9].

An FTIR system is typically composed of an infrared (IR) light source, an IR detector, and a Michelson interferometer (Figure 2.6). The Michelson interferometer consists of a beam-splitter and two mirrors (one is fixed and the other is movable). The beam-splitter divides the infrared beam in half, with one half of the beam directed towards a moving mirror and the other half being transmitted towards a fixed mirror. Both beams are reflected back towards the splitter where the two beams are recombined into a single beam. Variation of the position of the non-stationary mirror allows for the optical path length difference between the two mirrors relative to the splitter. As a result, varying amounts of interference can be obtained. The resultant signal from the recombined single beam is known as an interferogram and contains information on all frequencies within the scan range. The interferogram undergoes a Fourier transformation which is automatically done by the software, followed by the display of the IR spectrum, typically within 4000 cm^{-1} to 400 cm^{-1} [9, 17].

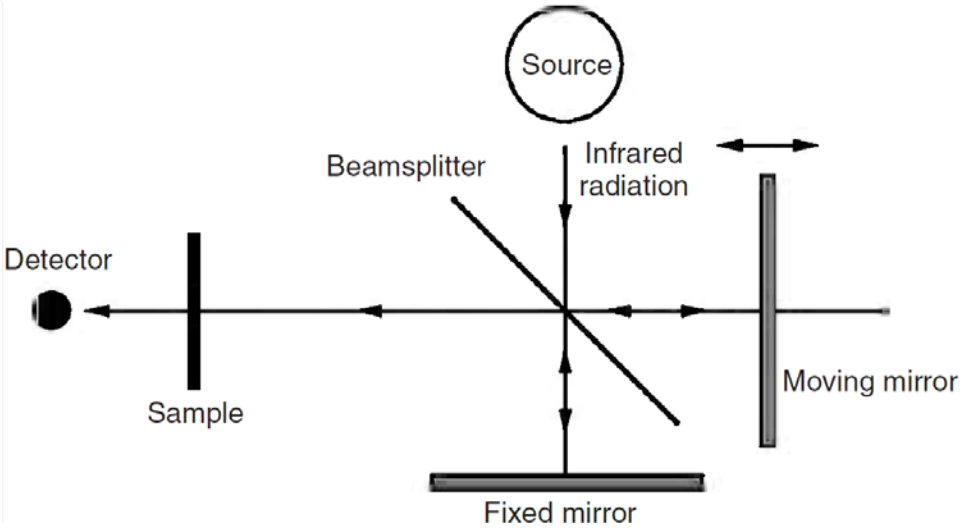

Figure 2.6. Schematic of a Michelson interferometer in transmission FTIR [9].

Attenuated Total Reflectance (ATR) FTIR is a particular technique that allows the vibrational characterization of non-transparent samples like powders or ceramics. In transmission FTIR, the detector is located behind the specimen and the IR beam is passed straight through the sample for collection. In the case of ATR FTIR spectroscopy, the infrared beam is totally internally reflected through an ATR crystal of relatively high refractive index in optical contact with the sample. The internally reflected radiation produces evanescent waves within the sample. Some of the energy of the evanescent wave is absorbed by the sample, and the reflected radiation is returned to the detector (Figure 2.7a). It is important that the sample must be in intimate contact with an ATR crystal in order to obtain reliable results [18].

In the present work, ATR FTIR measurements were performed in a single reflection mode using a Thermo-Scientific Nicolet 6700 FTIR spectrometer with a diamond crystal ATR plate (Figure 2.7b). In order to achieve intimate contact with an ATR crystal, samples were ground to a fine powder using an agate mortar and pestle. Powders were placed onto the diamond window and secured with a pressure tower to ensure good contact. The region from

400-4000 cm^{-1} was analyzed and 256 scans with a resolution of 1 cm^{-1} were collected for each measurement to ensure good statistics of the results. OMNIC software was used to obtain the data, and to apply baseline and ATR correction (in order to compensate for different wavelengths having different propagation lengths in the sample). A background spectrum was collected at the beginning of the session which was automatically subtracted by the software.

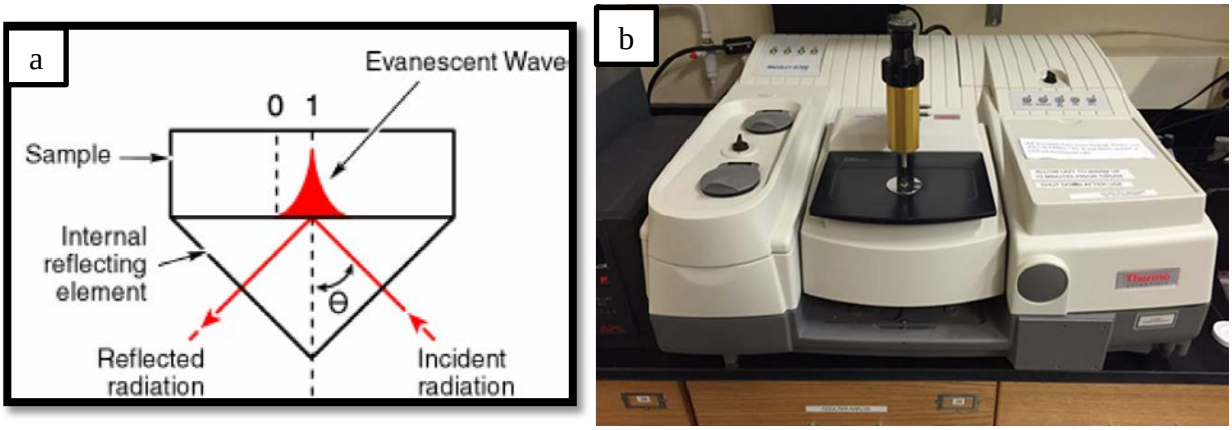

Figure 2.7. a) A schematic of a single reflection ATR; b) Thermo-Scientific Nicolet 6700 FTIR spectrometer with a diamond crystal ATR plate.

2.2.5 Ultraviolet/visible (UV/Vis) spectroscopy

The efficiency of a scintillator depends, in part, on the transparency of a material to its own light. Since scintillation is typically in the UV/Vis range of the electromagnetic spectrum, it is important to inspect the UV/Vis transparency of the material. If a scintillating material exhibits poor transparency to its own light, most of the emission will be trapped inside of the specimen and only a small fraction will be coming from the surface of the specimen; as a result, the scintillation output will be low. However, if a material has good optical transparency to its own light then emission will come not only from the surface but also from the interior.

Optical transparency is an especially important parameter for the scintillating polycrystalline ceramics as it is affected not only by the material properties (width of the band gap and the presence of absorption bands) but also by the presence of scattering centers. As it was discussed in section 2.2.3, polycrystalline ceramics might contain pores which change the local index of refraction resulting in the scattering of UV/Vis light passing through the sample and negatively affecting transparency.

The present work uses a double beam UV/Vis spectrophotometer that allows investigation of a material transparency in ultraviolet and visible range as a function of wavelength. It uses the beam intensity ratio, $I/I_{o,}$ to determine absorbance, A, or transmittance, T, as: $T = I/I_0 = \exp(-A)$ (Figure 2.8a). Optical transmittance measurements of the single crystals and polycrystalline ceramics were taken using a Perkin Elmer Lambda 950 UV/Vis/NIR spectrophotometer (Figure 2.8b). The reference sample holder was left empty for all measurements. Spectra were taken from 200 nm to 800 nm at a scan rate of 270 nm/min with a spectral resolution of 1 nm. Thickness of the compared samples was approximately the same; therefore, results were not corrected by the thickness of the samples.

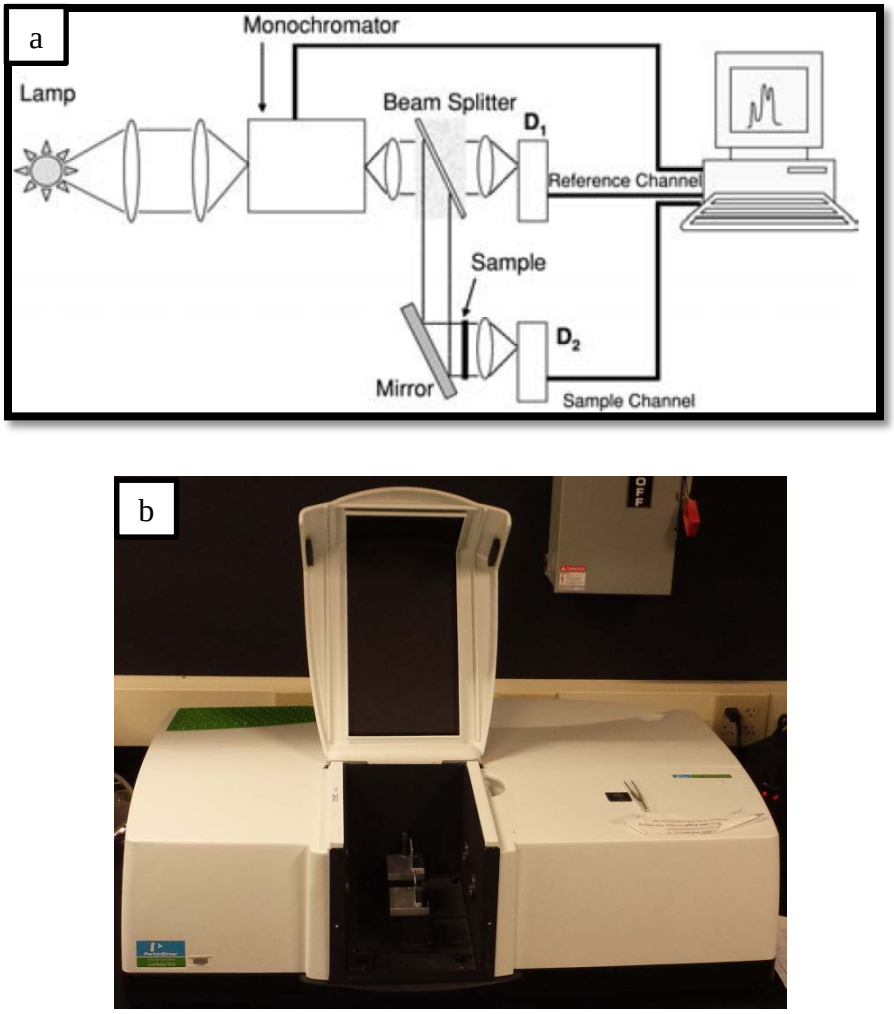

Figure 2.8. a) A schematic of a double beam UV/Vis spectrophotometer [19]; b) Perkin Elmer Lambda 950 UV/Vis/NIR spectrophotometer.

2.2.6 Photoluminescence (PL)

Luminescence corresponds to the emission of light due to excitation by some form of energy, but not as a result of material temperature (incandescence). [20].

The evaluation of the luminescence of scintillator means to assess the luminescence centers (activators) in the material. Rare earths are known to be efficient luminescence centers, with the energy of emitted photons being within UV/Vis/NIR region of the spectrum. The

reasons for different emission energies from different rare earth ions can be understood through the photophysics of the rare earths. Materials investigated in this work were doped with Ce^{3+} and Pr^{3+} ions and, thus, the photophysics of these ions are considered in more detail.

Based on the distribution and number of electrons, different types of atoms have different electron configurations and possibly different valence states. As an example, Table 2.2 shows the electron configuration of the rare earth elements, noting that Ce^{3+} and Pr^{3+} ions have only one and two electrons on their 4*f* orbitals, respectively. The presence of one or more electrons on the 4*f* orbital leads to energy level splitting due to spin and orbital angular momentum interactions. Three types of interactions affect the energy of the electrons in the orbitals as described by Hund's rules: spin-spin interaction (Hund's rule #1), orbit-orbit interaction (Hund's rule #2), and spin-orbit interaction (Hund's rule #3) [21].

Table 2.2. Electron configurations of rare-earth elements [22].

Element	Atom configuration	3+ ion configuration
Lanthanum	[Xe] $6s^2 4f^0 5d^1$	[Xe] $4f^0$
Cerium	[Xe] $6s^2 4f^1 5d^1$	[Xe] $4f^1$
Praseodymium	[Xe] $6s^2 4f^3$	[Xe] $4f^2$
Neodymium	[Xe] $6s^2 4f^4$	[Xe] $4f^3$
Promethium	[Xe] $6s^2 4f^5$	[Xe] $4f^4$
Samarium	[Xe] $6s^2 4f^6$	[Xe] $4f^5$
Europium	[Xe] $6s^2 4f^7$	[Xe] $4f^6$
Gadolinium	[Xe] $6s^2 4f^7 5d^1$	[Xe] $4f^7$
Terbium	[Xe] $6s^2 4f^9$	[Xe] $4f^8$
Dysprosium	[Xe] $6s^2 4f^{10}$	[Xe] $4f^9$
Holmium	[Xe] $6s^2 4f^{11}$	[Xe] $4f^{10}$
Erbium	[Xe] $6s^2 4f^{12}$	[Xe] $4f^{11}$
Thulium	[Xe] $6s^2 4f^{13}$	[Xe] $4f^{12}$
Ytterbium	[Xe] $6s^2 4f^{14}$	[Xe] $4f^{13}$
Lutetium	[Xe] $6s^2 4f^{14} 5d^1$	[Xe] $4f^{14}$

Hund's rule #1 reflects spin-spin interaction and states that the term with the highest value of total spin angular momentum, *S*, lies lowest in energy, which means that, for example, in the case of two electrons, the state in which their spins are parallel will be lower in energy than the state in which their spins are antiparallel. The origin of the energy difference is in the coulomb repulsion of the electrons. The fact that the spins of electrons are parallel implies a larger average distance between them than in the case of antiparallel spins. As a result, if the electrons are further apart, they will be less shielded from the nucleus by the other electrons, and, therefore, a given electron will be more exposed to the nucleus. This means that the electron in consideration will be more tightly bound and of lower energy. The total spin angular momentum quantum number for two electrons, *S*(2), is obtained by combining the individual spin quantum numbers s_1 and s_2 as following [21]:

$$S(2) = (s_1 + s_2), (s_1 + s_2 - 1), ..., |s_1 - s_2| \tag{2.5}$$

As all electrons in filled shells of an atom are spin-paired, it is only necessary to count spins in the outer unfilled orbitals to obtain values of *S* for the atom as a whole.

Hund's rule #2 reflects orbit-orbit interaction and states that for a given value of *S*, the term with the largest value of total orbital angular momentum, *L*, lies lowest in energy, which means that if the electrons are orbiting in the same direction (therefore, they have a large total angular momentum) they interact less often than when they orbit in opposite directions. Hence, on average, their mutual repulsion is lower when *L* is large. The total orbital angular momentum quantum number is calculated in a similar manner as the value of *S*. For two electrons, *L*(2), is obtained by combining the individual orbital quantum numbers l_1 and l_2 as following [21]:

$$L(2) = (l_1 + l_2), (l_1 + l_2 - 1), ..., |l_1 - l_2| \tag{2.6}$$

All filled shells of an atom have zero orbital angular momentum, thus, only electrons in the outer unfilled shells need to be counted. It is necessary to mention that, similar to the letter notation of individual orbital quantum numbers, *L* values are also replaced by letter symbols as shown in Table 2.3.

Table 2.3. Correspondence of *L* values to letter symbols.

L	0	1	2	3	4	5	6
Letter	S	P	D	F	G	H	I

Hund's rule #3 reflects spin-orbit interaction and states that for atoms with less than half-filled shells, the level with the lowest value of *J* lies lowest in energy. When the shell is more than half full, the opposite rule holds (level with the highest *J* lies lowest). Here, *J* is a quantum number reflecting the interaction between the spin and the orbital momentum. It can be understood as a magnetic field caused by the electron orbital motion interacting with the spin magnetic moment. *J* value is calculated as:

$$J = (L+S),(L+S-1),...,|L-S| \tag{2.7}$$

The combinations of *S*, *L*, and *J* are written in the form ${}^{2S+1}L_J$ and called a term symbol, which is representation of a set of energy levels in spectroscopy. The term uses the multiplicity $2S+1$, total orbital angular momentum *L*, and total angular momentum *J*. It assumes that all the spins are combined to produce *S*, all the orbital angular momenta are coupled to produce *L*, and then the spin and orbital terms are combined to produce a total angular momentum *J*.

Let us now consider the two cases of interest, Ce^{3+} and Pr^{3+} ions. In the case of Ce^{3+}, there is only one electron on the 4*f* orbital. Thus, its total spin angular momentum quantum

number is simply $S(1) = ½$. On the other hand, Pr^{3+} has two electrons on its 4*f* orbital, and, as s_1 and s_2 are equal to ½, equation (2.5) gives $S(2) = 1$ or 0, meaning that both values are permitted. According to Hund's rule #1, the energy level with $S = 1$ will be lower in energy than $S = 0$. For the electron in the *f* shell, there are 7 orbitals available each with a given orbital quantum number, as shown in Figure 2.9. Based on the analogy with equation (2.6), $L = l = 3$ for Ce^{3+} ion, which is letter F according to Table 2.3, and $L = 5, 4, 3, 2, 1$ for Pr^{3+} ion, which are letters H, G, F, D, P, respectively.

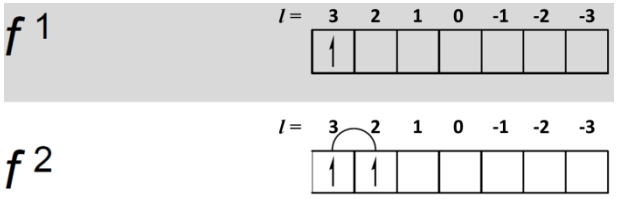

Figure 2.9. Orbitals available for an *f* electron with electrons placed for the case of Ce^{3+} (f^1) and Pr^{3+} (f^2). Individual orbital quantum numbers are shown as *l* values and orbitals are filled according to the Pauli Exclusion Principle.

Combination of *L* value with multiplicity term, $2S+1$, gives ^2F for Ce^{3+} and ^3H, ^3G, ^3F, ^3D, ^3P, ^1H, ^1G, ^1F, ^1D, ^1P for Pr^{3+}. However, in the case of Pr^{3+}, energy levels ^3G, ^3D, ^1H, ^1F, and ^1P are forbidden due to the Pauli Exclusion Principle (*e.g.* ^3G is forbidden because it corresponds to the situation of two electrons with positive spin in the same orbital of *f* shell).

The last step leads to the calculation of *J* values using equation (2.7) for each ^{2S+1}L term obtained earlier. As a result, $^{2S+1}L_J$ terms for Ce^{3+} are $^2F_{5/2}$ and $^2F_{7/2}$, and for Pr^{3+} are $^3H_4$, $^3H_5$, $^3H_6$, $^3F_2$, $^3F_3$, $^3F_4$, $^3P_0$, $^3P_1$, $^3P_2$, $^1G_4$, $^1D_2$. According to Hund's rules, the lowest energy level (ground state) will be $^2F_{5/2}$ for Ce^{3+} ion and $^3H_4$ for Pr^{3+} ion. The relative position of the other

energy levels can also be defined according to Hund's rules, and it is reflected in the so-called Dieke diagram [23] of these two ions shown in Figure 2.10.

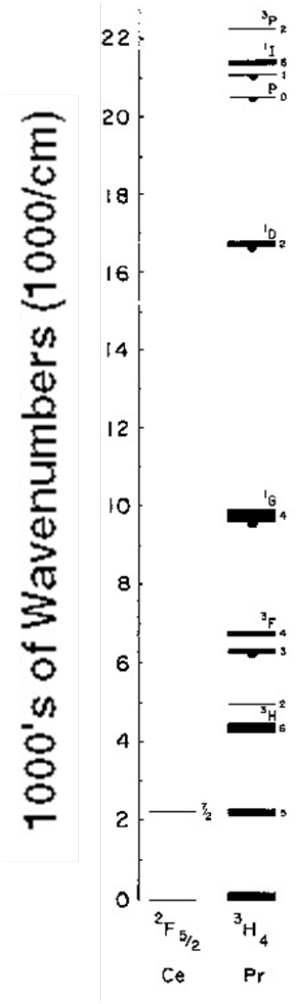

Figure 2.10. Section of a Dieke diagram [23] showing energy levels of Ce^{3+} and Pr^{3+} ions.

Additional to the spin-orbit coupling that results in energy level splitting, if an ion is placed in a certain material (e.g. Ce^{3+} in LuAG matrix), the host also effects the outer-most energy levels of the ion, resulting in crystal field splitting or, more generally, ligand field splitting [24]. In the case of Ce^{3+} and Pr^{3+}, placement of these ions in a garnet material will result

in the splitting of the 5*d* energy level, as schematically shown in Figure 2.11a for the case of Ce^{3+}. Energy level $5d_t$ (^2T_g) (notations correspond to the interaction between the ion and the crystal [24]) is usually of little concern since it is typically located in the conduction band of the host material and, therefore, does not participate in the excitation/emission transitions. On the other hand, energy levels of an activator located in the band gap are of the biggest interest for luminescent and scintillating materials as they are the ones involved in the emission of light. The coupling of the electronic levels of the activator with the vibrational modes also creates additional energy states (Figure 2.11b), allowing for excitation and emission from a range of photon energies. Once excited to a higher vibrational level, the excess energy is dissipated to the surrounding matrix through phonon generation such that the electron is now at the lowest vibrational state associated to the excited electronic state. From there, the electron de-excites to some vibrational level related to the ground state. Again, the excess energy is dissipated to the surrounding matrix through phonon generation such that the electron moves to the lowest vibrational state associated to the ground state. In such a manner, the photon emitted from the de-excitation process will have lower energy than the excitation photon (Figure 2.11b). This phenomenon is known as the Stokes shift [20]. Due to such complex behavior of luminescence centers, it is important to probe the luminescence of a material in order to obtain the excitation and emission spectra.

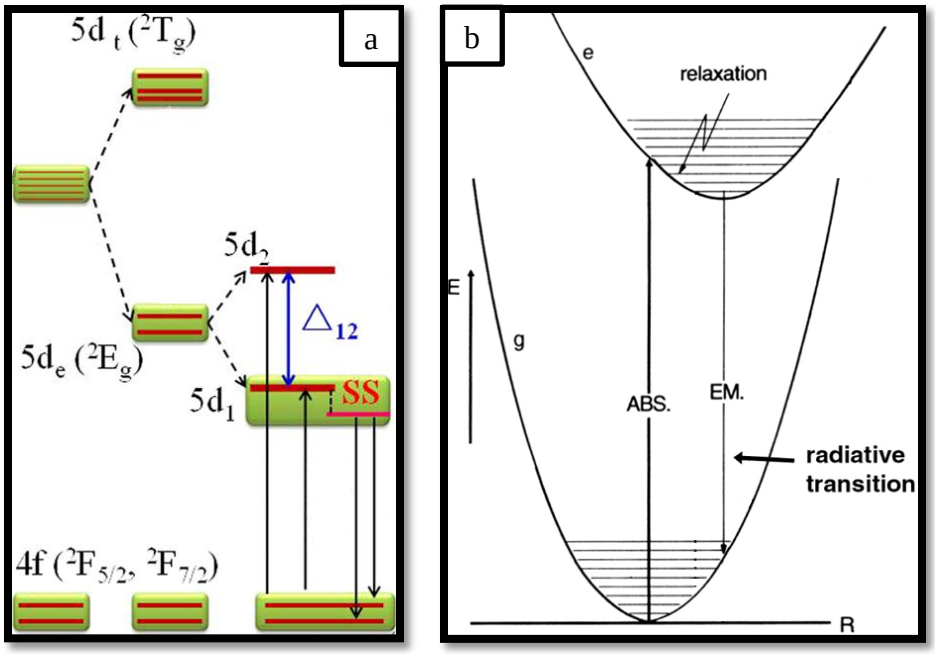

Figure 2.11. a) A schematic representation of the energy levels splitting of Ce^{3+} in a garnet matrix [25]. SS indicates Stokes shift; Δ_{12} emphasized energy difference between $5d_1$ and $5d_2$ levels. b) The absorption and emission energies in a vibrating lattice showing the Stokes shift [20]. Horizontal lines indicate vibrational energy levels.

There are several types of luminescence distinguished based on the source of excitation energy. *Photoluminescence* occurs due to excitation with UV/Vis light; *cathodoluminescence* is the result of excitation with an electron beam; *radioluminescence* is caused by ionizing radiation (gamma-rays, X-rays, α particles, etc.); *thermoluminescence* is due to the release of energy stored in material traps induced by heating; *electroluminescence* is a result of an electric current passing through a material; *triboluminescence* is emission of light produced by a mechanical disturbance; *sonoluminescence* uses passage of the acoustic waves through a liquid; and *chemiluminescence* is a result of a chemical reaction [19]. Luminescence behavior of the

materials in this work was explored by means of photoluminescence, radioluminescence, and thermoluminescence measurements.

A typical experimental arrangement to measure photoluminescence is presented in Figure 2.12a. The sample is excited with an excitation source, such as a xenon lamp, and the light generated is filtered to the proper wavelengths by the excitation monochromator. The emitted light is collected and analyzed by means of the emission monochromator, followed by a photomultiplier tube (PMT) detector connected to a computer. Both emission and excitation spectra can be registered. In emission spectra, the excitation wavelength is fixed and the emitted light is measured at different wavelengths by scanning the emission monochromator. In excitation spectra, the emission monochromator is fixed at any emission wavelength of interest while the excitation wavelength is scanned in a certain spectral range [19].

Photoluminescence measurements were conducted using a Horiba Jobin-Yvon Fluorolog-322 spectrofluorometer equipped with a xenon lamp and double monochromators for both excitation and emission (Figure 2.12b). Solid state sample holder was set to 15° relative to the excitation source. Spectra were measured using integration time of 1 sec, spectral resolution of 1 nm, and convergence slits of 1 nm. Excitation and emission ranges were varied depending on the material under investigation.

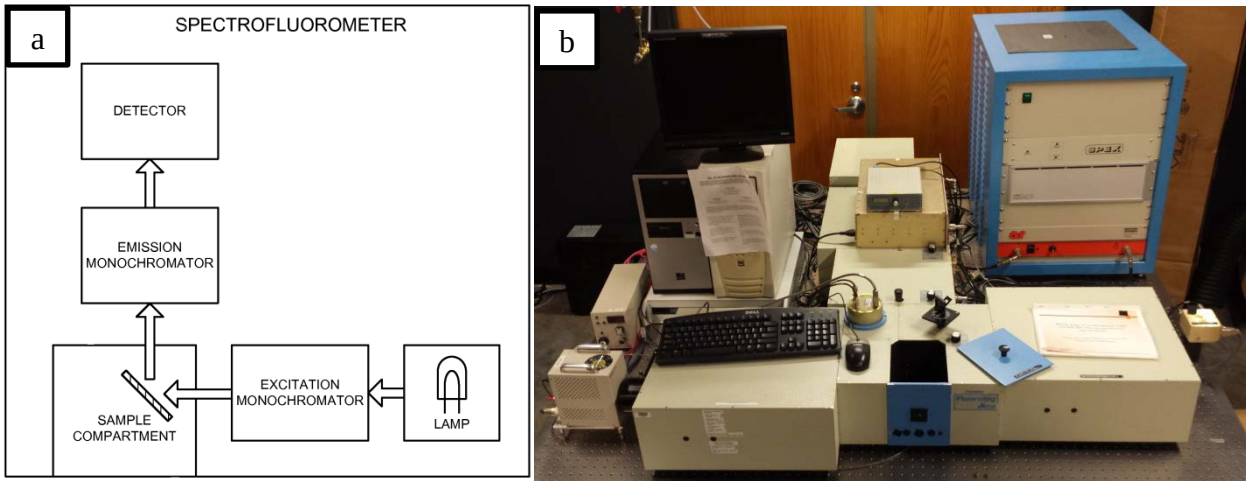

Figure 2.12. a) A schematic diagram of photoluminescence spectrofluorometer [19]. b) Horiba Jobin-Yvon Fluorolog-322 spectrofluorometer.

2.2.7 Radioluminescence (RL)

As noted above, radioluminescence is another technique to probe the luminescence of a material. Unlike photoluminescence, RL allows measurements of the emitted light using X-rays as the excitation source. The use of the high excitation energy of X-rays comparing to UV/Vis light enables simultaneous excitation of all luminescence centers in the material, including luminescent defects. As a result, additional information about emission of luminescence centers that were not originally revealed with PL can be obtained. Moreover, in many aspects, RL mimics the scintillation response of a material and one can gain insight into the scintillation response of a material by means of RL measurements.

Radioluminescence investigation is performed under X-ray excitation coming from an X-ray tube directly above the sample (see Figure 2.13). The emitted light is collected by optical fiber protected from damage by X-rays with a lead shield. The light is transported through the fiber towards a spectrograph connected to a CCD camera, analyzed, and emission spectrum is

displayed on a computer. Measurements were done using a custom-designed Freiberg Instruments Lexsyg Research spectrofluorometer equipped with a Varian Medical Systems VF-50J X-ray tube operating with a tungsten target at 40 kV and 1 mA, and an Andor Technology DU920P-BU Newton CCD camera. Spectra were not corrected for the spectral sensitivity of the system.

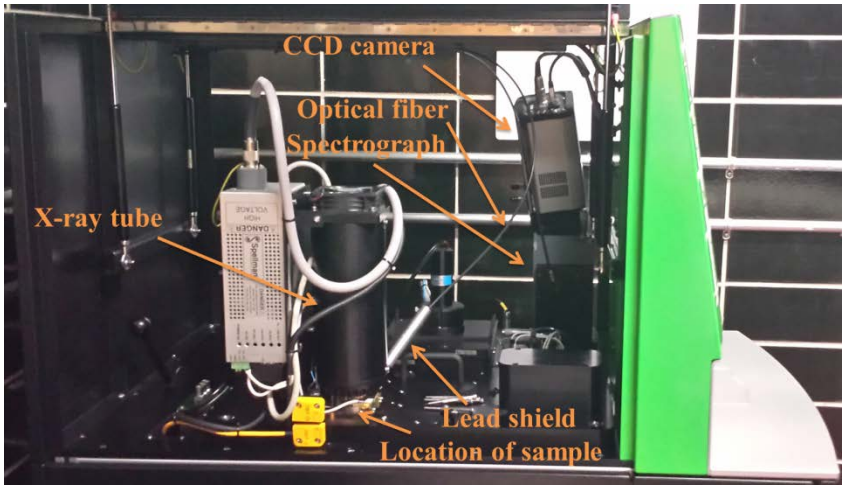

Figure 2.13. Custom-designed Freiberg Instruments Lexsyg Research spectrofluorometer.

2.2.8 Thermoluminescence (TL)

Another technique for investigating the luminescence behavior of a material is thermoluminescence – thermally stimulated emission of light after exposure to ionizing radiation [26]. The TL mechanism is described here in terms of the electron behavior, though an equivalent discussion can be applied for the hole.

If a material possesses impurities or structural defects within its lattice, it disturbs the periodicity of the crystalline structure and leads to an appearance of localized energy levels within the band gap, which are electronic manifestations of defects. As a result, an electron can

be captured from the conduction band by these levels. Several kinds of transitions are possible and are considered in Figure 2.14a.

First, the electron absorbs the incoming ionizing radiation, thus being promoted from the valence band into the conduction band (Figure 2.14a, transition (a)). Appearance of the defect centers can result in trapping the charge carrier (*e.g.*, electron) at localized energy levels within the forbidden gap (called traps; transition (b)). The charge carrier will remain trapped until given enough energy (in TL case, thermal energy) to leave the trap and return to the conduction band (transition (c) in the case of electrons), where it can travel towards the luminescence center (activator) and undergo recombination with the previously trapped hole (transition (d) and (e)) [26]. Conversely, it can be captured by the trap once again. In such a manner, TL represents a powerful tool to investigate traps of the scintillators; however, it does not allow distinguishing between electron and hole traps.

In order to understand the methods of analysis of TL measurements that are applied in the present work, a brief theoretical basis is provided. Representation of a thermoluminescence experiment is shown in Figure 2.14b, where the relationship between the intensity of emitted light, $I(t)$, and the concentration of trapped electrons, n_e, can be seen. Increase of the temperature provides thermal energy to the material and results in the release of the electrons from the traps and their recombination, decreasing the number of trapped electrons and increasing TL intensity. As traps are continuously emptied the recombination rate slows and, therefore, TL intensity decreases resulting in the characteristic TL peak. This process at constant heating rate, β, is described by the system of equations (2.8):

$$\begin{cases} p = s \cdot \exp\left(-E/kT\right) \\ I\left(t\right) = -\mathrm{d}\, n_e / \mathrm{d}\, t \\ T = T_0 + \beta t \\ \beta = \mathrm{d}\, T / \mathrm{d}\, t \end{cases} \tag{2.8}$$

where the probability per unit time, *p*, of the release of an electron from the trap of activation energy, *E*, at given temperature, *T*, is given by the Arrhenius equation; temperature is linearly increased with time, *t*; and *s*, called "frequency factor" or "attempt-to-escape frequency", represents the number of times per second that a trapped electron interacts with lattice phonons multiplied by the transitional probability. Therefore, the maximum value anticipated for *s* is the lattice vibration frequency, namely 10^{12}-10^{14} sec^{-1} [26]. Commonly, experimental results are presented in terms of the intensity of emitted light versus temperature, with a plot known as the "glow curve".

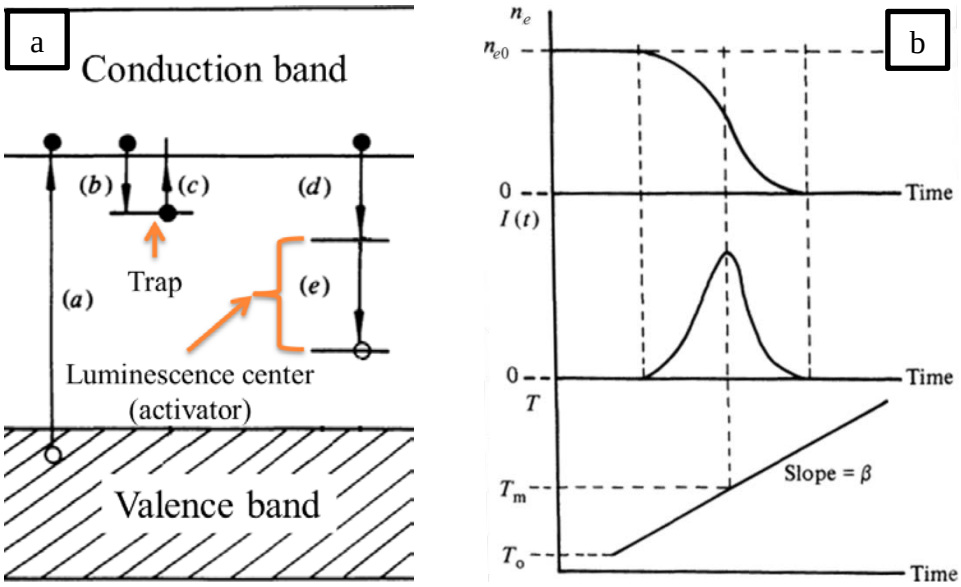

Figure 2.14. a) Common electronic transitions in inorganic scintillators: (a) ionization, (b) electron trapping, (c) electron thermal release, (d, e) radiative recombination. Electrons – solid circles, holes – open circles. b) Correlation between TL intensity and a number of electrons released from the traps and recombined [26].

Over the years different models were proposed for TL analysis [26, 27]. The most studied model is called the simple model, which relies on the assumption that the lifetime of an electron in the conduction band is much less than the lifetime of a trapped electron. In this model, two criteria for the electron released from the trap are considered: (1) the probability of electron being trapped again (retrapping) is negligible compared to the probability of recombination and the thermoluminescence mechanism is characterized by first-order kinetics [28, 29], and (2) the probability of retrapping dominates, and the thermoluminescence mechanism is characterized by second-order kinetics [26].

As a result of these assumptions, intensity of the emitted light can be expressed as

$$I(t) = np = ns\exp(-E/kT) \tag{2.9}$$

for the first-order kinetics, and

$$I(t) = n^2 s\exp(-E/kT) = ns'\exp(-E/kT) \tag{2.10}$$

for the second-order kinetics. Integration of equations (2.9) and (2.10) over time from $t=t_0$ gives intensity as a function of temperature.

$$I(T) = n_0 s\exp(-E/kT)\exp\left[-(s/\beta)\int_{T_0}^{T}\exp(-E/kT)\,dT\right] \tag{2.11}$$

$$I(T) = {n_0}^2 s\exp(-E/kT)/\left[1+(n_0 s/\beta)\cdot\int_{T_0}^{T}\exp(-E/kT)\,dT\right]^2 \tag{2.12}$$

The general-order kinetics (intermediate situation between first- and second-order) is also possible, and it is considered elsewhere [26, 27].

From equations (2.9) and (2.10), it can be understood how to distinguish first- and second-order kinetics experimentally. Analysis of the intensity dependence on the number of trapped electrons, *n*, shows that, if *n* varies, a first-order kinetic peak will remain at the same

position. On the other hand, the second-order peak will shift towards higher temperatures. Also, second-order glow-curve will exhibit higher thermoluminescence intensity during the higher temperature fraction of the peak caused by higher probability of retrapping. This is illustrated with a computed set of glow-curves in Figure 2.15.

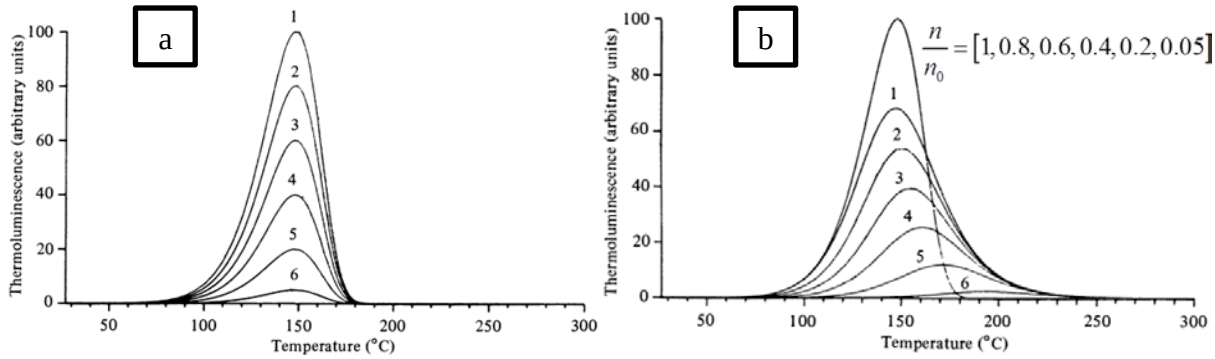

Figure 2.15. Computer-simulated a) first- and b) second-order kinetics glow-curves. The most intense first-order peak is shown for comparison. E=1.0 eV, s=10^{10} s^{-1}, β=10 °C/min. The curves are calculated for the following fractions of the traps filled prior to heating: (1) 1.0, (2) 0.8, (3) 0.6, (4) 0.4, (5) 0.2, and (6) 0.05 [26].

A variety of TL analysis methods were developed to extract parameters such as peak position, T_m, activation energy (trap depth), E, and frequency factor, s, from the glow curve. In the present work, it is shown that the traps of the investigated materials exhibit first-order kinetics (see Chapter 3) and, thus, TL glow curves were analyzed using the Randall-Wilkins model (first-order kinetics model) by means of the GlowFit software that fits experimental data using the least squares Levenberg-Marquardt method and yields the peaks position and the trap depth [30].

Thermoluminescence measurements were performed in the 50–400 °C range using a Thermo Scientific Harshaw thermoluminescence dosimeter (TLD) reader model 3500 (Figure 2.16) with a heating rate of 1 °C/s. Before each measurement, samples were annealed at 400 ^{o}C for 1 or 5 minutes to deplete all traps, and were X-ray irradiated using a Rigaku Ultima IV X-ray diffractometer (40 kV, 40 mA) for different amounts of time in order to populate the traps. The dose exiting the X-ray tube on the diffractometer was on the order of 10^7 R/hr. For RL and TL measurements, small platelets were cut from the original samples due to space limitations of the instruments sample holder.

Figure 2.16. Thermo Scientific Harshaw TLD reader model 3500.

2.2.9 Differential pulse height distribution measurements

Differential pulse height distribution measurements are used to determine the luminosity of a scintillator in relation to a known reference via analysis of the charge generated by the radiation interaction in the material [14].

The scintillation photons eject photoelectrons from a photocathode of the PMT via the photoelectric effect. Photoelectrons are then electrostatically accelerated and focused towards first dynode of the PMT. A single photoelectron ejects multiple secondary electrons from the

dynode that are accelerated and eject electrons from the second dynode. This effect cascades until electrons are collected at the anode, and the end result is that scintillation photons are converted into a measurable electrical signal. The electrical signal is collected by a multi-channel analyzer, where the channel corresponding to the maximum of the distribution is extracted (channel number of the photopeak) and used to determine the scintillator luminosity. The intensity of the electrical signal is proportional to the number of photons emitted from the scintillator and the energy of the ionizing radiation. Therefore, for the same radioactive source (and measurement conditions, *e.g.*, the gain applied to the PMT), the ratio of the electrical signal intensity between the sample and the reference provides the relative luminosity of the sample – the higher the peak channel number, the brighter the material [14]. This process is schematically represented in Figure 2.17.

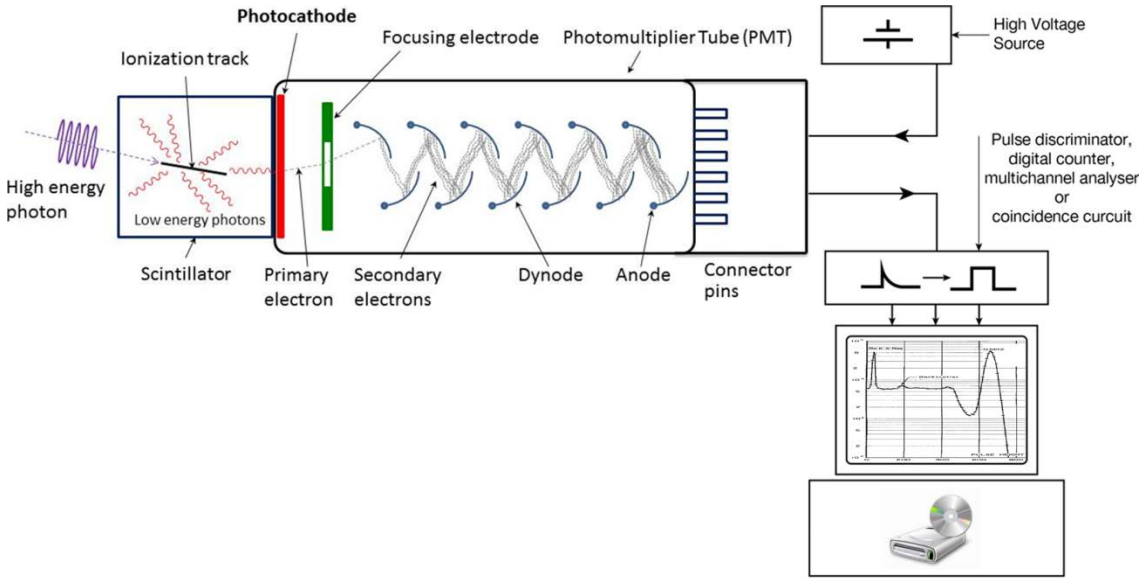

Figure 2.17. A schematic representation of differential pulse-height measurements apparatus.

Differential pulse height distribution measurements additionally allow extraction of the energy resolution of a scintillator. Energy resolution essentially reflects the amount of energy fluctuations that was recorded; as the energy resolution becomes lower, instead of showing one large peak that potentially encompasses many peaks, single defined peaks in the same energy range can be evaluated, yielding more information. It should be noted that there may only be one peak in the given spectrum, but that peak will become more defined as the energy resolution decreases. Resolution is a dimensionless quantity given in percent and is defined as the full width at half maximum (FWHM) divided by the centroid of the distribution, H_0 [14]:

$$R(\%) = \frac{\text{FWHM}}{H_0} \cdot 100\% \tag{2.13}$$

Performing measurements using a variety of γ-ray sources allows for the exploration of scintillation properties of the material such as light yield, energy resolution, and proportionality of the material response to different energies of ionizing radiation. These measurements were conducted using a Hamamatsu R6095 bialkali photocathode PMT operated at 1000 V and 2 μs shaping time inside a light-proof box (Figure 2.18), together with the necessary power supply, control and data acquisition electronics. For the polycrystalline ceramic samples provided by RMD, the PMT operated at 800 V, 1.2 μs rise time, and 0.6 μs flat top time. The setup involves coupling the sample to a photomultiplier tube with optical grease and mounting a radioactive source above the sample. Scintillation under irradiation from various γ-ray point sources (see Table 2.4) are recorded, and light yield relative to $Bi_4Ge_3O_{12}$ (BGO) single crystal was determined for the given emission of the radioactive source.

Figure 2.18. Pulse height distribution measurements apparatus with Hamamatsu R6095 bialkali photocathode photomultiplier tube.

Table 2.4. Point sources and their energies used for differential pulse height distribution measurements.

Point source	Energy, keV
^{241}Am	59.5
^{133}Ba	31.0, 81.0, 302.9, 356.0
^{22}Na	511, 1274.0
^{137}Cs	32.2, 661.7
^{57}Co	122.1, 136.5
^{54}Mn	834.9

References

[1] R.S. Silva, M.I.B. Bernardi, A.C. Hernandes, Synthesis of non-agglomerated $Ba_{0.77}Ca_{0.23}TiO_3$ nanopowders by a modified polymeric precursor method, J Sol-Gel Sci Technol, 42 (2007) 173-179.

[2] J.C.A. Santos, E.P. Silva, D.V. Sampaio, N.R.S. Souza, Y.G.S. Alves, R.S. Silva, Radioluminescence emission of YAG:RE laser-sintered ceramics, Mater Lett, 160 (2015) 456-458.

[3] T.C.d. Oliveira, M.S.d. Silva, L.M.d. Jesus, D.V. Sampaio, J.C.A.d. Santos, N.R.d.S. Souza, R.S.d. Silva, Laser sintering and radioluminescence emission of pure and doped Y_2O_3 ceramics, Ceram Int, 40 (2014) 16209-16212.

[4] X. Tian, A. Dittmar, J. Melcher, J.G. Heinrich, Sinterability studies on $K_{0.5}Na_{0.5}NbO_3$ using laser as energy source, Appl Surf Sci, 256 (2010) 5918-5923.

[5] L. Ji, Y. Jiang, Laser sintering of transparent Ta_2O_5 dielectric ceramics, Mater Lett, 60 (2006) 1502-1504.

[6] P.A. Cutler, C.L. Melcher, M.A. Spurrier, P. Szupryczynski, L.A. Eriksson, Scintillation non-proportionality of lutetium- and yttrium-based silicates and aluminates, IEEE T Nucl Sci, 56 (2009) 915-919.

[7] M.R. Marchewka, M.G. Chapman, H. Qian, L.G. Jacobsohn, Incorporation of Pr into LuAG ceramics, Opt Mater, 68 (2017) 53-57.

[8] A.A. Trofimov, C. Li, K.S. Brinkman, L.G. Jacobsohn, Luminescence investigation of Ce incorporation in garnet-type $Li_7La_3Zr_2O_{12}$, Opt Mater, 68 (2017) 7-10.

[9] Y. Leng, Materials Characterization: Introduction to Microscopic and Spectroscopic Methods, Wiley-VCH, Germany, 2013.

[10] R. Jenkins, R.L. Snyder, Introduction to X-Ray Powder Diffractometry, John Wiley & Sons, Inc., New York, 1996.

[11] J. Goldstein, D.E. Newbury, D.C. Joy, Scanning Electron Microscopy and X-Ray Microanalysis, 3rd ed., Kluwer Academic/Plenum Publishers, New York, 2003.

[12] D.B. Williams, C.B. Carter, Transmission electron microscopy: a textbook for materials science, 2nd ed., Springer, 2009.

[13] M.I. Medndelson, Average grain size in polycrystalline ceramics, J Am Ceram Soc, 52 (1969) 443-446.

[14] G.F. Knoll, Radiation Detection and Measurement, 4th ed., John Wiley & Sons, Inc, Michigan, 2010.

[15] T.L. Heath, The works of Archimedes, Cambridge University Press, London, 1897.

[16] G. Gouadec, P. Colomban, Raman Spectroscopy of nanomaterials: How spectra relate to disorder, particle size and mechanical properties, Prog Cryst Growth Ch, 53 (2007) 1-56.

[17] N.B. Colthup, L.H. Daly, S.E. Wiberley, Introduction to infrared and Raman spectroscopy, 3rd ed., Academic Press, San Diego, 1990.
[18] M.W. Urban, Attenuated Total Reflectance Spectroscopy of Polymers, American Chemical Society, Washington, DC, 1996.
[19] J. Solé, L. Bausa, D. Jaque, An Introduction to the Optical Spectroscopy of Inorganic Solids, John Wiley & Sons, Ltd, 2005.
[20] R.J.D. Tilley, Luminescence, in: Colour and the Optical Properties of Materials, John Wiley & Sons, 2011.
[21] J.W. Rohlf, Modern Physics from α to Z^0, John Wiley & Sons, 1994.
[22] G. Rayner-Canham, T. Overton, Descriptive Inorganic Chemistry, 5th ed., W.H. Freeman and Company, New York, 2010.
[23] G.H. Dieke, Spectra and Energy Levels of Rare Earth Ions in Crystals, John Wiley & Sons, 1968.
[24] F.A. Cotton, Chemical Applications of Group Theory, 3rd ed., Texas A&M University, College Station, TX, 1990.
[25] L. Chen, X. Chen, F. Liu, H. Chen, H. Wang, E. Zhao, Y. Jiang, T.-S. Chan, C.-H. Wang, W. Zhang, Y. Wang, S. Chen, Charge deformation and orbital hybridization: intrinsic mechanisms on tunable chromaticity of $Y_3Al_5O_{12}:Ce^{3+}$ luminescence by doping Gd^{3+} for warm white LEDs, Sci Rep, 5 (2015) 11514.
[26] S.W.S. McKeever, Thermoluminescence of Solids, Cambrige University Press, Cambrige, 1988.
[27] R. Chen, S.W.S. McKeever, Theory of Thermoluminescence and Related Phenomena, World Scientific, Singapore, 1997.
[28] J.T. Randall, M.H.F. Wilkins, Phosphorescence and Electron Traps. I. The Study of Trap Distributions, Proceedings of the Royal Society of London. Series A, Mathematical and Physical Sciences, 184 (1945) 365-389.
[29] J.T. Randall, M.H.F. Wilkins, Phosphorescence and Electron Traps. II. The Interpretation of Long-Period Phosphorescence, Proceedings of the Royal Society of London. Series A, Mathematical and Physical Sciences, 184 (1945) 390-407.
[30] M. Puchalska, P. Bilski, GlowFit — a new tool for thermoluminescence glow-curve deconvolution, Radiat Meas, 41 (2006) 659-664.

CHAPTER THREE

RESULTS AND DISCUSSION

3.1 Microstructure, luminescence, and scintillation of laser-sintered ceramic and single crystal $Y_3Al_5O_{12}$:Ce (YAG:Ce)

YAG:Ce polycrystalline ceramics are prepared by the modified polymeric precursor method followed by laser sintering [1]. It is important to determine whether investigated samples are actually phase-pure YAG. XRD measurements are performed to identify the crystalline structure and presence of secondary phases. The single-phase YAG cubic structure of the polycrystalline ceramic samples is confirmed, in agreement with ICDD card #00-033-0040 (Figure 3.1), and Rietveld Refinement revealed almost identical lattice parameter ($\Delta \approx 0.1$ %) for the polycrystalline ceramics (11.9992 Å) and for the single crystal (12.0089 Å). SEM micrographs of the polycrystalline sample (Figure 3.2) display the presence of various grains with average size of 2.5 µm. Defects, such as grain boundaries and pores, can also be seen.

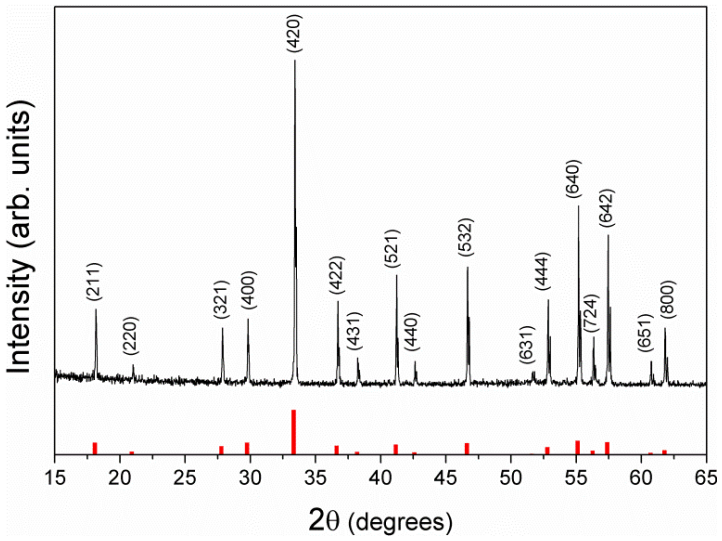

Figure 3.1. XRD results of YAG:0.3% Ce polycrystalline ceramic indexed according to ICDD #00-033-0040 (bar plot).

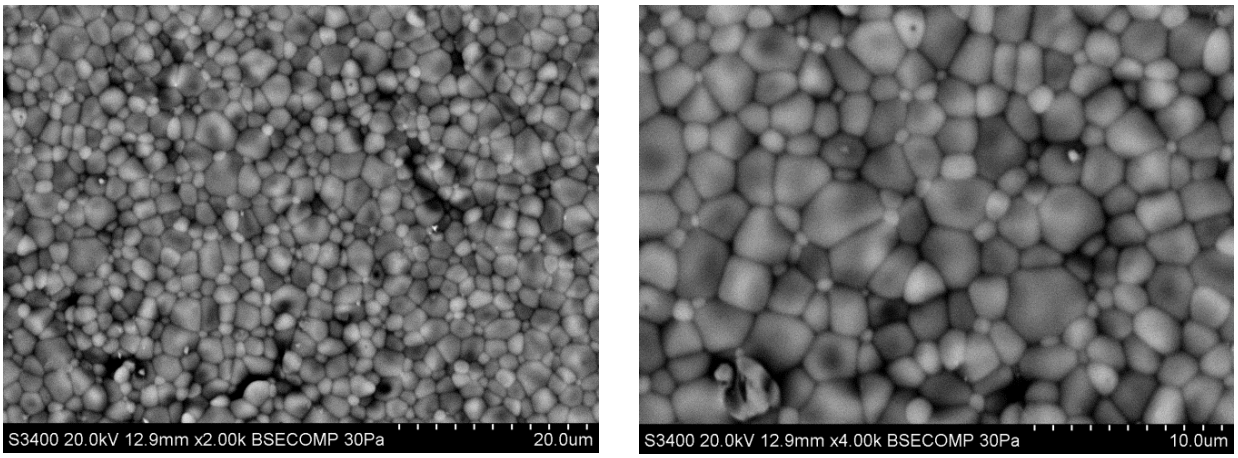

Figure 3.2. SEM micrographs of YAG:0.3%Ce polycrystalline ceramic.

Literature review, presented in Chapter I (cf. Figure 1.2), shows that the average of the most recent reports of YAG:Ce luminosity is ca. 10% higher for the single crystal than those for the polycrystalline ceramic. Americium-241 differential pulse height distributions are presented in Figure 3.3 for YAG:Ce scintillators. A Gaussian function is used to fit the photopeaks and extract the peak positions. The relative light yield is determined by normalizing the position of the peaks from the analyzed samples with the position of the same peaks, obtained with the BGO single crystal (Figure 3.4). The overall behavior shows that YAG:Ce single crystal is about 2 times brighter than BGO and several times brighter than the polycrystalline ceramics, which qualitatively correlates with the literature reports in Figure 1.2 showing that the average value of light output is higher for YAG:Ce single crystal than for polycrystalline ceramic.

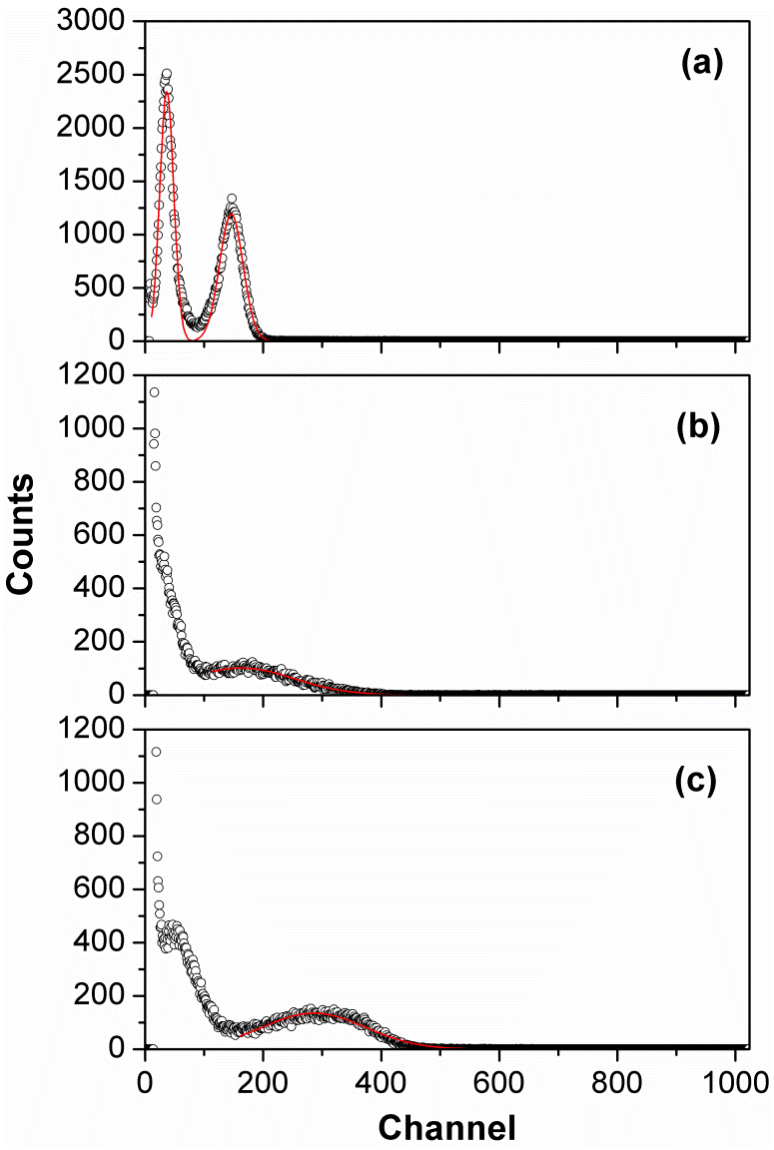

Figure 3.3. Pulse height spectra of 59.5 keV γ-rays from ^{241}Am point source. (a) YAG:Ce single crystal (gain 50), (b) YAG:0.1%Ce polycrystalline ceramic (gain 250) and (c) YAG:0.3%Ce polycrystalline ceramic (gain 250). Black circles are the experimental data; red lines are Gaussian fits. Additional photopeak, corresponding to 13.9 keV γ-rays from a ^{241}Am source can be seen at lower channels for the single crystal and YAG:0.3%Ce polycrystalline ceramic.

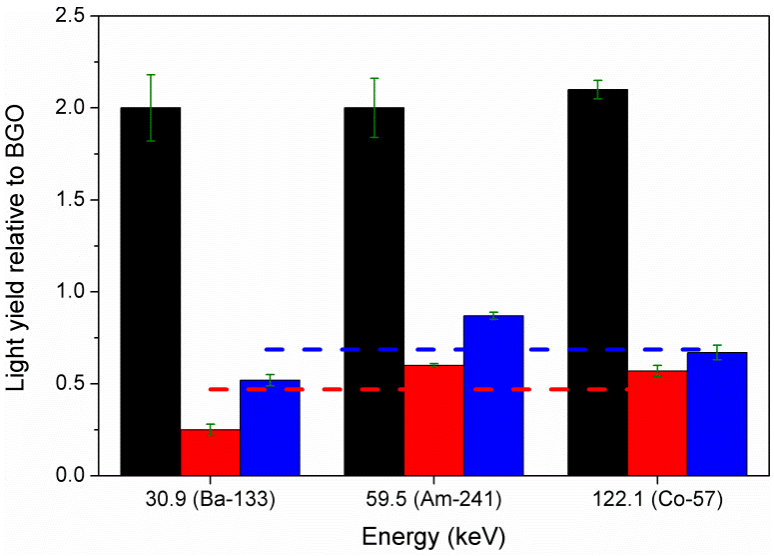

Figure 3.4. Light yield of the YAG:Ce relative to BGO crystal. YAG:Ce single crystal (black), YAG:0.1%Ce polycrystalline ceramic (red), and YAG:0.3%Ce polycrystalline ceramic (blue). Dashed lines are average values for each ceramic.

Figure 3.5 shows the ATR FTIR spectra of the samples at ambient temperature. Since absolute intensities cannot be compared due to the possible difference of contact area of the samples during the measurements, all spectra are normalized to the most intense peak at ca. 687 cm^{-1}. It is known that the unit cell of YAG:Ce consists of Al cations occupying eight octahedral sites and twelve tetrahedral sites, and Y cations placed in twelve dodecahedral sites [2]. The vibrational modes observed in the spectra in Figure 3.5 are correlated to the vibrations of these structural units. Seven superimposed peaks can be easily seen, and extracted peak positions are in good agreement with the reported values [2-5]. Vibration modes are assigned as follows: translation mode of octahedral cations at ca. 425 cm^{-1}, symmetric bends of the AlO_4 tetrahedron at ca. 448 cm^{-1}, asymmetric bends of the tetrahedron between 500-600 cm^{-1}, and asymmetric stretching modes of the tetrahedron between 600-900 cm^{-1} [4].

Systematic shift of the majority of the bands of the polycrystalline ceramics to higher frequencies by ca. 2 cm^{-1} is observed in relation to those of the single crystal. It is well-known for the garnet structure that an increase in the volume of the unit cell is related to a decrease of the frequency of the vibrational modes [4, 6]. Therefore, the atomic network within the grains composing the polycrystalline ceramics is under compressive stress. Measurements done on a series of identical samples confirm the observed shift. Interestingly, the observed shift of IR peak frequencies is approximately 0.3 % of the peak values for the single crystal, which implies a linear dependence of the frequencies on the unit cell volume, similar to previously reported results [6].

It is also important to note that the full width at half maximum (FWHM) of the majority of the bands of the polycrystalline ceramics is 3-5 cm^{-1} larger than that for the single crystal, as illustrated in the inset of Figure 3.5. The broadening of the vibration bands indicates higher structural disorder of the polycrystalline ceramics with regard to the crystal [7].

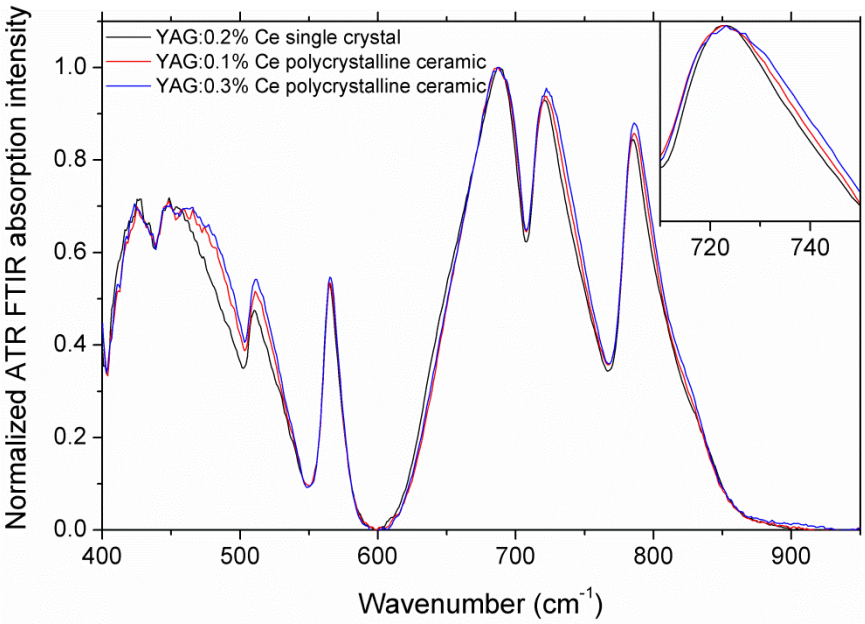

Figure 3.5. Normalized absorption ATR FTIR spectra of the YAG:Ce. The inset illustrates the difference in the band width. The peaks in the inset were matched in the intensity and peak position in order to reveal the width difference.

PL excitation (PLE) spectra monitored at 2.34 eV (530 nm) and PL emission (PL) spectra excited at 3.63 eV (342 nm) of the single crystal and polycrystalline ceramics are presented in Figures 3.6a and 3.6(b, c), respectively. Normalized PLE spectra show two excitation bands centered around 2.73 eV (450 nm) and 3.63 eV (342 nm), which are caused by the Ce^{3+} $4f \rightarrow 5d_1$ and $5d_2$ transitions, respectively [8, 9]. The fine structure between 2.6-2.9 eV of the excitation spectra is due to a variation in intensity of the xenon lamp, which results in some sharp features [9]. The broad emission band around 2.34 eV (530 nm) is well-known to be an overlap of the double band of Ce^{3+} emission $5d_1 \rightarrow 4f$ ($^2F_{5/2}$, $^2F_{7/2}$) [9, 10] (cf. the deconvolution in Figure 3.6), due to the spin-orbit coupling split of $4f$ energy level of Ce^{3+} ion. Corresponding emission bands are at 2.21 and 2.37 eV (561 and 523 nm, respectively). The split of ca. 0.17 eV is approximately the same for the single crystal and polycrystalline ceramics. The observed Stokes shift was also

similar between the single crystal (0.39 eV) and polycrystalline YAG:Ce (0.41 eV). However, the FWHM of the excitation bands was noticeably different. FWHM of the band at 2.73 eV ($4f \rightarrow 5d_1$ transition of Ce^{3+}) is 0.36 eV, 0.48 eV, and 0.55 eV for the single crystal, 0.1 % Ce ceramic, and 0.3 % Ce ceramic, respectively. FWHM of the band at 3.63 eV ($4f \rightarrow 5d_2$ transition) is 0.25 eV, 0.29 eV, and 0.31 eV for the single crystal, 0.1 % Ce ceramic, and 0.3 % Ce ceramic, respectively. The observed difference in FWHM of the bands is ascribed to the higher structural disorder of the polycrystalline scintillators in agreement with the results from ATR FTIR analysis. The resulting enhanced self-absorption in the polycrystalline ceramics was found to be ca. 1.31 (YAG:0.1%Ce) and 1.54 (YAG:0.3%Ce) times higher in the polycrystalline ceramics than in the single crystal based on the ratio of the intersection area between the PL and PLE spectra within 2.25 to 2.8 eV normalized by the area of the PL spectrum (1.86-2.8 eV).

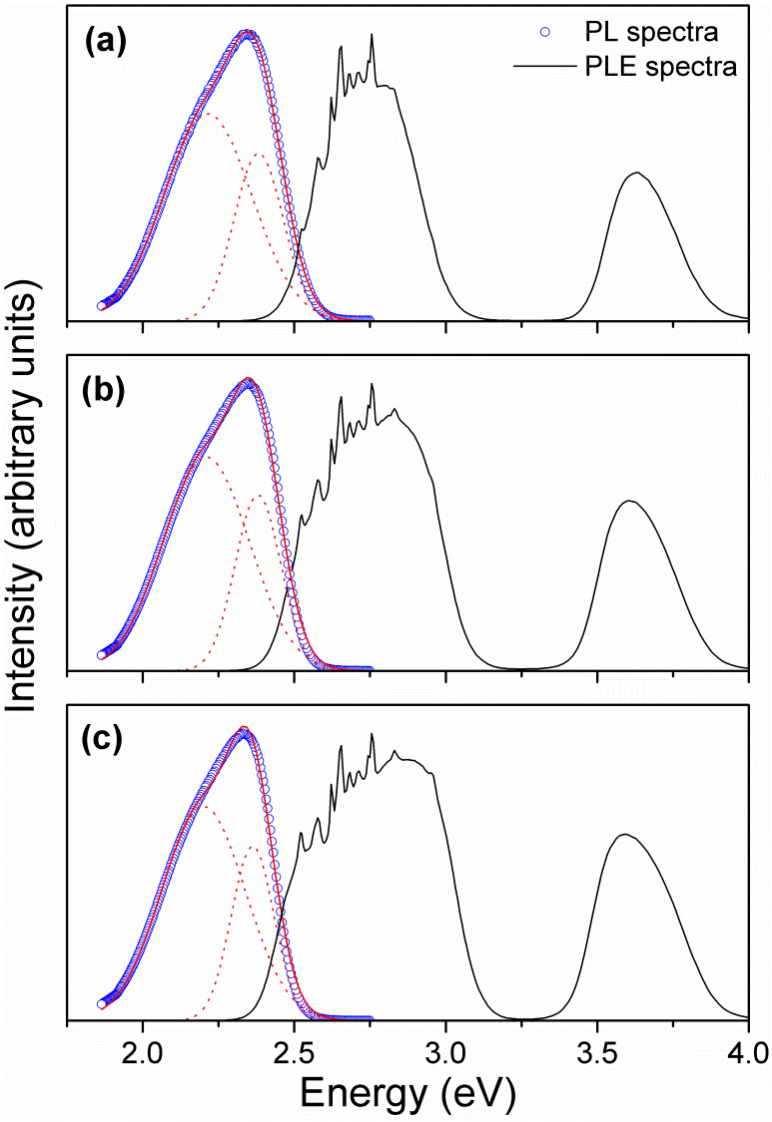

Figure 3.6. PL (blue circles) and PLE (black lines) spectra of a) YAG:Ce single crystal, b) YAG:0.1%Ce polycrystalline ceramic, and c) YAG:0.3%Ce polycrystalline ceramic. Gaussian deconvolution (red dotted lines) of PL spectra together with the best fit (red continuous lines) are also shown.

To further investigate luminescence properties, room temperature RL measurements are performed and analyzed. Normalized RL spectra of both single crystal and polycrystalline ceramics are dominated by the emission band peaked at ca. 2.34 eV which is assigned to the

emission of Ce^{3+} (Figure 3.7). The results of the deconvolution of this band with two Gaussian peaks were similar to the results of the deconvolution of the PL spectra and are not discussed further. RL measurements also revealed weaker emission beyond ca. 3 eV (inset in Figure 3.7). According to previous reports, emission region 2.5-4.5 eV can correspond to a variety of the defects in YAG system: the band centered within 3.9-4.2 eV has been assigned to the emission of excitons localized around Y_{Al} antisite defects [10-13], recombination luminescence of Y_{Al} antisite defects has been observed within 3.3-3.7 eV region [10, 11, 14, 15], emission at 3.1-3.2 eV has been attributed to the F^+-type defects [10, 11, 14, 16, 17], and a band peaking at 2.5-2.7 eV has been assigned to the F centers [14, 16, 17]. Based on the aforementioned reports on the intrinsic luminescence in the undoped YAG and YAG:Ce, RL emission observed within 3-4 eV region (Figure 3.7) has been attributed to the superimposition of the luminescence of Y_{Al} antisite defects, the F^+ centers, and possible contribution from localized excitons (LE) around Y_{Al} antisite defects (cannot be fully resolved since the measurements are limited to 4 eV). It is important to note that the emission bands formed by Y_{Al} antisite defects and F^+ centers strongly overlap with the absorption bands of Ce^{3+} ions that are centered at 2.73 and 3.63 eV (inset in Figure 3.7).

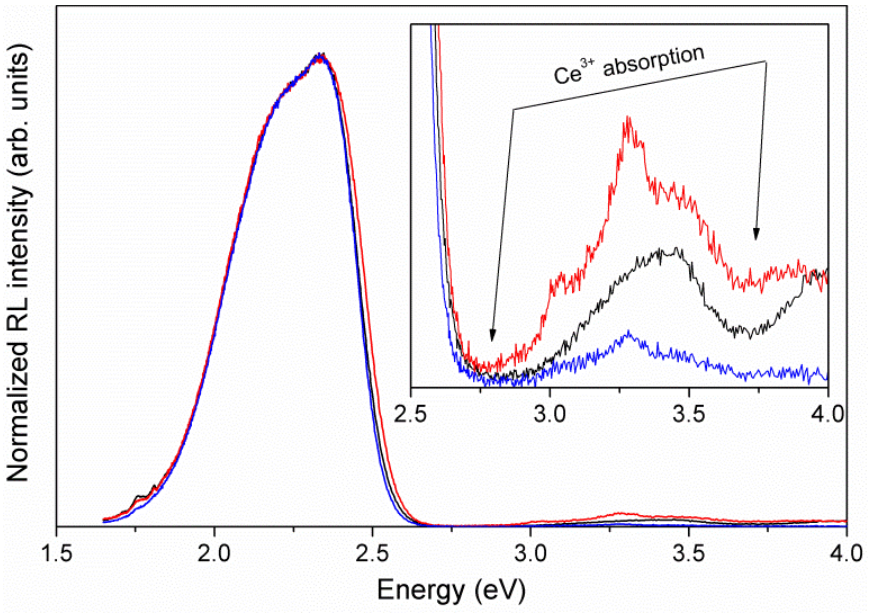

Figure 3.7. Normalized RL spectra of YAG:Ce single crystal (black), YAG:0.1%Ce polycrystalline ceramic (red), and YAG:0.3%Ce polycrystalline ceramic (blue). Inset shows a magnification of the emission in the 2.5-4.0 eV range and emphasizes the overlap with the absorption bands of Ce^{3+} in YAG.

To gain more insight into the nature of these defects, additional PL/PLE measurements are performed. All materials show a presence of the same defect-related luminescence centers with the emission at 3.21 eV (386 nm) and 2.97 eV (418 nm) and the excitation near 3.60 eV (345 nm) and 4.54 eV (273 nm) as shown in Figure 3.8. Extensive literature review of defect excitation and emission in YAG is done in order to understand the nature of these bands (see Table 3.1). Based on the available reports, emission at 2.97 eV and excitation at 4.54 eV are related to F center, emission at 3.21 eV is related to F^+ center, and excitation at 3.5-3.8 eV is an overlap of the bands related to F^+ and F^- centers. Note that the signal-to-noise ratio of the spectra of the single crystal is significantly lower than that of the polycrystalline ceramics, indicating a lower concentration of these defects in the crystal.

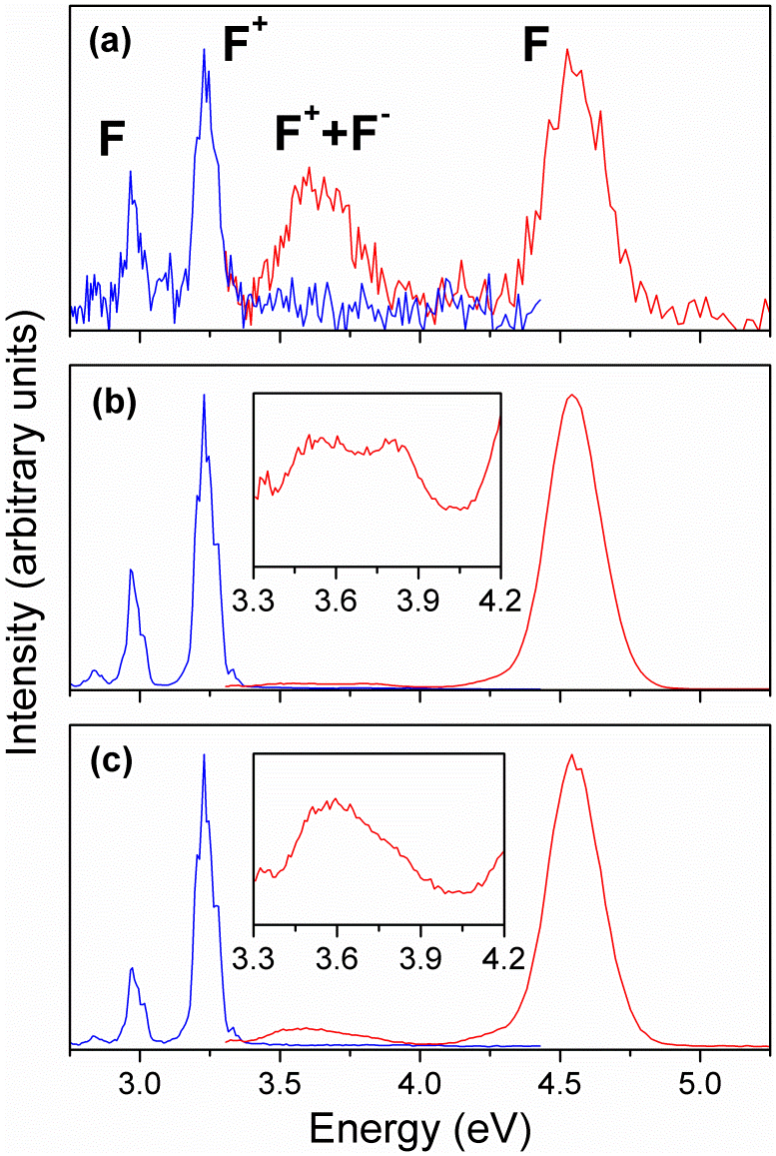

Figure 3.8. PLE spectrum monitored at 3.21 eV (386 nm; red), and PL spectrum excited at 4.54 eV (273 nm; blue) for a) YAG:Ce single crystal, b) YAG:0.1%Ce polycrystalline ceramic, and c) YAG:0.3%Ce polycrystalline ceramic.

Table 3.1. Literature review of defect excitation and emission in YAG and YAG:Ce in the order of increasing energies.

Type of material	Absorption/Excitation and defect type	Emission and defect type	Reference
Undoped crystal	1.49 eV (830 nm) → F^- 2.58 eV (480 nm) → F^-	2.67 eV (464 nm) → F 2.70 eV (460 nm) → F	[17]
Undoped crystal	–	3.095 eV (401 nm) → F^+	[16]
Undoped crystal	–	3.10 eV (400 nm) → F^+	[17, 18]
Ce-doped crystal	–	3.12 eV (398 nm) → F-type	[19]
Ce-doped nanoceramic (room temperature)	–	3.15 eV (394 nm) → F^+ 3.33 eV (372 nm) → Y_{Al}	[10]
Undoped crystal	3.35 eV (370 nm) → F^+	–	[17, 18]
Ce-doped crystal	3.35 eV (370 nm) → F^+	–	[20]
Ce-doped crystal	3.35 eV (370 nm) → F-type	–	[19]
Undoped crystal	3.44 eV (360 nm) → F^-	–	[17]
Undoped crystal	–	3.72 eV (333 nm) → Y_{Al}	[21]
Undoped crystal	–	3.88 eV (320 nm) → Y_{Al}	[15]
Ce-doped nanoceramic (room temperature)	4.13 eV (300 nm) → F^+	4.12 eV (301 nm) → LE at Y_{Al}	[10]
Ce-doped crystal	–	4.12 eV (301 nm) → LE at Y_{Al}	[19]
Undoped crystal	–	4.22 eV (294 nm) → LE at Y_{Al}	[21]

Undoped crystal (low temperature)	–	4.77 (260 nm) → self-trapped exciton	[15]
Ce-doped nanoceramic (T=8K)	4.80 eV (258 nm) → F 5.12 eV (242 nm) → F^+	–	[10]
Undoped crystal	5.17 eV (240 nm) → F^-	–	[17]
Undoped crystal	5.28 eV (235 nm) → F^+	–	[17, 18]
Ce-doped crystal	5.28 eV (235 nm) → F^+	–	[20]
Ce-doped crystal	5.28 eV (235 nm) → F^+	–	[19]
Undoped crystal	6.2 eV (200 nm) → ?	–	[18]
Undoped crystal	6.36 eV (195 nm) → F	–	[17]
Undoped crystal	6.80 eV (182 nm) → Y_{Al} 6.88 eV (180 nm) → LE at Y_{Al}	–	[21]

The results of optical transmission measurements of the polycrystalline ceramics and the single crystal are displayed in Figure 3.9. Single crystal exhibits ca. 76 % transparency up to 2.38 eV (520 nm) followed by two absorption bands matching the positions of the Ce^{3+} excitation peaks observed in PLE measurements and, therefore, corresponding to the $4f \rightarrow 5d$ electronic transitions of Ce^{3+} ions. Polycrystalline ceramics have a much poorer transparency since the samples are translucent. It is worth noting, however, that the $4f \rightarrow 5d_1$ transition of the polycrystalline samples (at ca. 2.71 eV) is at a similar position as for the single crystal, while the $4f \rightarrow 5d_2$ transition is at ca. 3.46 eV for the ceramics and at 3.63 eV for the crystal. The observed shift as well as the large absorption in the polycrystalline YAG:Ce in the 4-5 eV range is likely

due to the strong overlap with the excitation band formed by the F, F^+, and F^- centers (cf. Figure 3.8). As it was shown by PL analysis, F-type centers are present in both materials but their concentration is significantly lower for the single crystal; thus, the influence of its absorption/excitation band on the transmittance of the samples is much lower in the case of the single crystal than in the case of the polycrystalline ceramics.

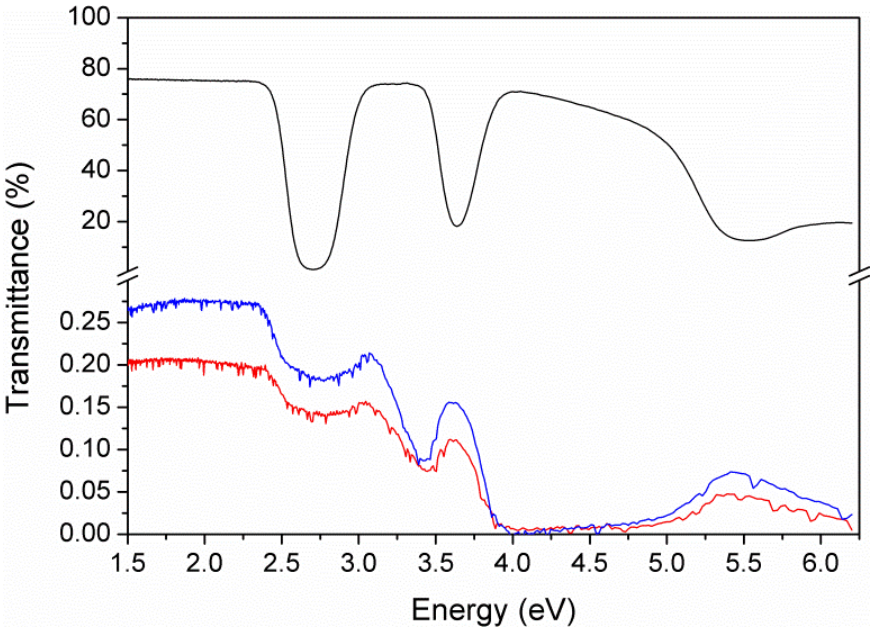

Figure 3.9. Optical transmission of YAG:Ce single crystal (black), YAG:0.1%Ce polycrystalline ceramic (red), and YAG:0.3%Ce polycrystalline ceramic (blue).

Defects in the material manifest themselves as localized energy levels within a bandgap and act as electron traps. Thermoluminescence is used in the present work to investigate the traps. Representative TL measurements of both polycrystalline ceramics and single crystal are displayed in Figure 3.10. The glow-curves are dominated by the emission within ca. 50-170 °C and 200-350 °C.

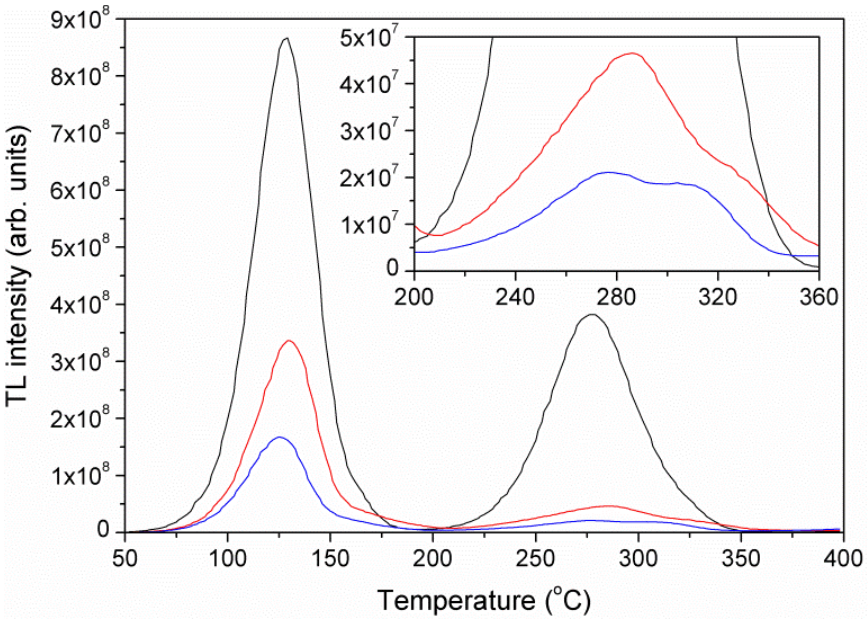

Figure 3.10. TL glow curves of YAG:Ce single crystal (black), YAG:0.1%Ce polycrystalline ceramic (red), and YAG:0.3%Ce polycrystalline ceramic (blue).

The order of kinetics of each glow peak is investigated employing X-ray irradiation with different durations, from 30 to 300 sec, together with the monitoring of the peak position. These results are shown in Figure 3.11 and reveal first-order kinetics for all glow peaks due to the lack of a systematic shift of the peak position for increasing irradiation doses [22].

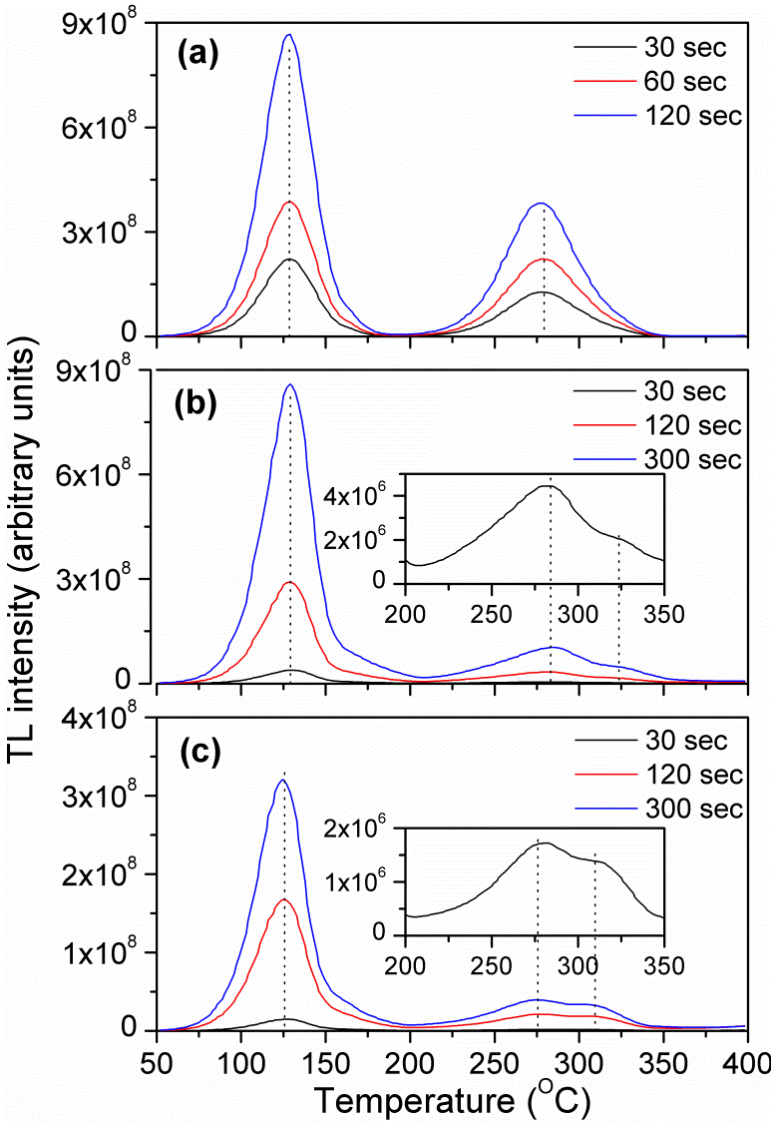

Figure 3.11. TL glow curves obtained using different X-ray irradiation time for (a) YAG:Ce single crystal, (b) YAG:0.1%Ce polycrystalline ceramic and (c) YAG:0.3%Ce polycrystalline ceramic. The vertical dotted lines are guides to the eyes only. Irradiation time of 300 sec could not be used for the single crystal due to the saturation of TLD reader.

Establishing the first-order kinetics indicates negligible probability of electron retrapping and allows further analysis using the Randall-Wilkins model [23, 24]. Four methods of TL analysis based on this model are used. The first method uses a simple expression developed by

McKeever and Chen that assumes first-order kinetics and that the trap can be described by the trap depth, E, temperature of the TL peak, T_m, and FWHM of the TL peak [25, 26]:

$$E_{McC} = 2.52 k_B T_m^2 / \mathrm{FWHM} - 2 k_B T_m \tag{3.1}$$

where k_B is Boltzmann constant. Only data for the low temperature peak are calculated as FWHM cannot be extracted for other peaks due to their strong overlap with each other. Results for 3 irradiation times are presented in Table 3.2.

In addition to E and T_m, the description of a trap requires determination of the frequency factor or "attempt-to-escape frequency", s: the number of interactions of an electron in the trap with lattice phonons per second multiplied by transition "probability" [22]. For the first-order kinetics, s can be obtained as

$$s = \frac{\beta E / k_B T_m^2}{\exp\left(-E / k_B T_m\right)} \tag{3.2}$$

where β is heating rate, which is 1 °C/sec in the present case. Values of the frequency factor are shown in Table 3.2.

Table 3.2. Parameters of the glow peaks and corresponding traps using McKeever-Chen expression.

McKeever-Chen formula												
Irradiation time, sec	YAG:0.2%Ce single crystal				YAG:0.1%Ce polycrystalline ceramic				YAG:0.3%Ce polycrystalline ceramic			
	T_m, °C	FWHM, °C	E, eV	s, sec^{-1}	T_m, °C	FWHM, °C	E, eV	s, sec^{-1}	T_m, °C	FWHM, °C	E, eV	s, sec^{-1}
30	129	36.3	0.90	$1.2x10^{10}$	128	34.7	0.94	$2.2x10^{11}$	127	35.6	0.91	$1.7x10^{10}$
60	129	36.2	0.90	$1.2x10^{10}$	–	–	–	–	–	–	–	–
120	128	35.4	0.92	$1.3x10^{10}$	129	33.7	0.97	$2.6x10^{11}$	125	34	0.94	$1.9x10^{10}$
300	–	–	–	–	129	32.9	1.00	$2.8x10^{11}$	125	33.1	0.97	$2.1x10^{10}$
Average	129	36.0	0.91	$1.2x10^{10}$	129	33.8	0.97	$2.5x10^{11}$	126	34.2	0.94	$1.9x10^{10}$

The second method is based on the decomposition of glow curves by means of the GlowFit software. The software fits experimental data using the least squares Levenberg-Marquardt method and yields the peak position and the trap depth [27], which can be further extended to calculate the *s* parameter using eq. (3.2). Figure 3.12 illustrates the best fit results for the 120 sec irradiation time, while Table 3.3 summarizes the peak positions, T_m, trap depth, E, and frequency factor, s, obtained from the best fit analysis of all samples and irradiation times. Comparison of the present result of TL peak positions to the literature on TL of YAG:Ce (Figure 3.13) validates the possibility of four types of traps being present in the investigated samples.

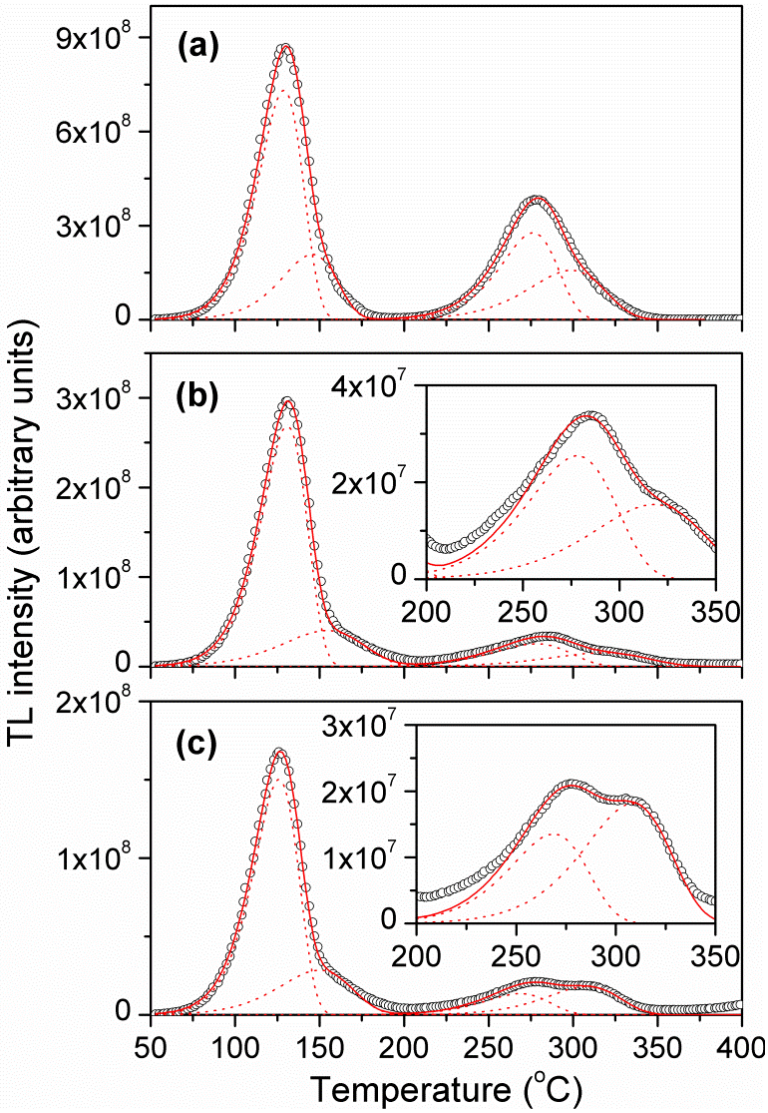

Figure 3.12. Decomposition of glow curves (black circles) of (a) YAG:Ce single crystal, (b) YAG:0.1%Ce polycrystalline ceramic and (c) YAG:0.3%Ce polycrystalline ceramic X-ray irradiated for 120 sec. The continuous red lines are the best fits obtained using GlowFit software; the dotted red lines are the fit of the individual glow peaks.

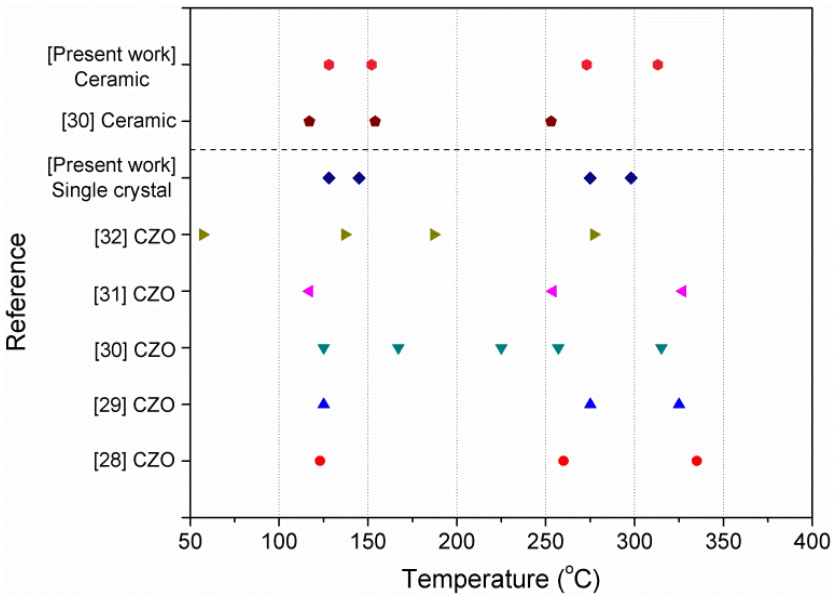

Figure 3.13. Comparison of the present results of TL peak positions to the literature on TL of YAG:Ce [28-32]. Only reports using 1 °C/sec heating rate are presented since T_m is a function of the heating rate. CZO is Czochralski grown single crystal.

Table 3.3. Parameters of the traps using glow curve fitting. Standard deviation is extracted based on the results for 3 irradiation times.

GlowFit curve analysis								
YAG:0.2%Ce single crystal			YAG:0.1%Ce polycrystalline ceramic			YAG:0.3%Ce polycrystalline ceramic		
T_m, °C	E, eV	s, sec^{-1}	T_m, °C	E, eV	s, sec^{-1}	T_m, °C	E, eV	s, sec^{-1}
128	1.03±0.01	$6.55x10^{11}$± $7.3x10^{10}$	130	1.02±0.01	$3.52x10^{11}$± $5.6x10^{10}$	126	1.00±0.02	$3.21x10^{11}$± $2.8x10^{10}$
145	0.88±0.03	$2.38x10^{9}$± $9.6x10^{8}$	154	0.66±0.06	$5.14x10^{6}$± $7.42x10^{6}$	149	0.64±0.04	$2.71x10^{6}$± $2.73x10^{6}$
275	1.50±0.04	$3.62x10^{12}$± $1.4x10^{12}$	278	1.17±0.05	$3.31x10^{9}$± $2.67x10^{9}$	270	1.24±0.02	$2.03x10^{10}$± $1.1x10^{10}$
298	1.21±0.08	$2.06x10^{9}$± $8.9x10^{8}$	318	1.08±0.11	$7.49x10^{7}$± $9.3x10^{7}$	310	1.30±0.07	$7.97x10^{9}$± $9.5x10^{8}$

The third method uses a combination of the McKeever-Chen expression and GlowFit decomposition. Using T_m and FWHM of the decomposed glow-curves, the method yields almost identical trap depth values and, consequently, similar *s* values to those obtained by glow curves fitting (cf. Table 3.3).

The fourth method is known as multiple heating rates method or peak position method and is based on the dependence of T_m on the heating rate β. Using several heating rates and noting the value of the T_m each time, the plot of $\ln\left(T_m^2/\beta\right)$ against $1/T_m$ can be made and a straight line of slope E/k and intercept $\ln\left(E/sk\right)$ are obtained [33]. As a result, both *E* and *s* can be extracted (Figure 3.14). Applying four different heating rates (β = 1, 2, 3, 5 °C/sec), the values of *E* and *s* are calculated and are shown in Table 3.4.

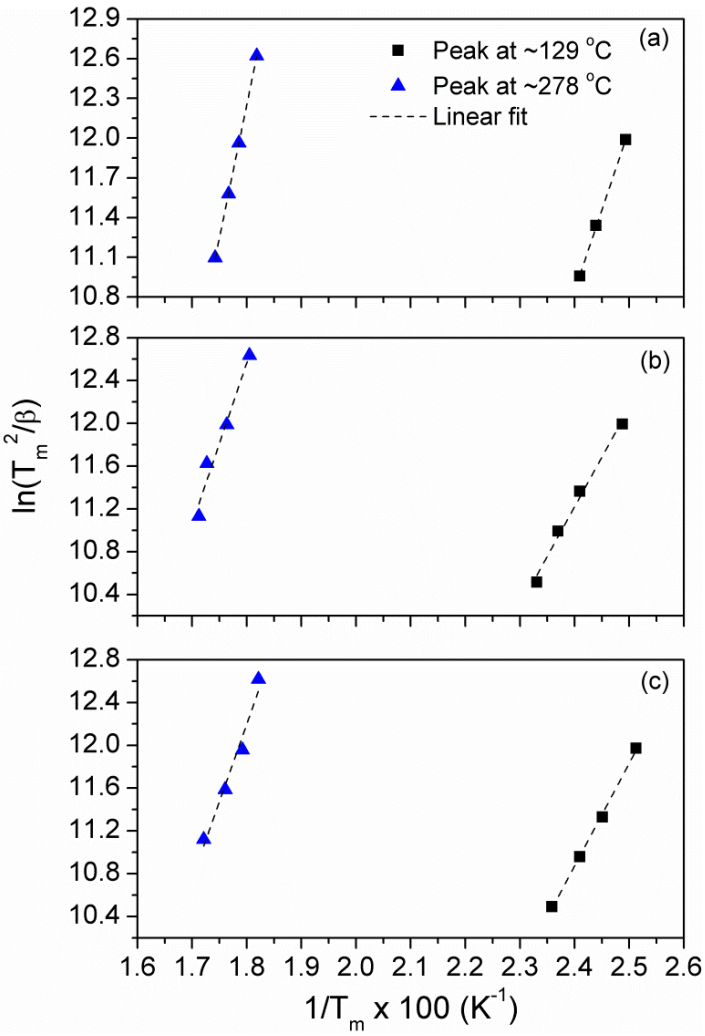

Figure 3.14. Experimental points and fits for TL glow peaks using method of multiple heating rates. (a) YAG:0.2%Ce single crystal, (b) YAG:0.1%Ce polycrystalline ceramic and (c) YAG:0.3%Ce polycrystalline ceramic.

Table 3.4. Parameters of the traps using multiple heating rates method.

Multiple heating rates analysis						
	YAG:0.2%Ce single crystal		YAG:0.1%Ce polycrystalline ceramic		YAG:0.3%Ce polycrystalline ceramic	
	E, eV	*s*, sec^{-1}	*E*, eV	*s*, sec^{-1}	*E*, eV	*s*, sec^{-1}
Peak at ~129 °C	1.05	$1.21x10^{12}$	0.80	$5.87x10^{8}$	0.83	$1.84x10^{9}$
Peak at ~278 °C	1.73	$4.71x10^{14}$	1.30	$3.03x10^{10}$	1.25	$1.50x10^{10}$

The temperature range investigated (above room temperature) allows probing of the so-called “deep” traps, which activation energy, *E*, is typically between 0.8-1.2 eV. On the other hand, the attempt-to-escape frequency, *s*, value is limited by the magnitude of the lattice vibration frequency, namely 10^{12}-10^{14} sec^{-1} [22]. It can be seen from Tables 3.2, 3.3, and 3.4 that the applied TL analysis methods give larger values of *E* for high temperature traps (200-350 °C) and reasonable values for low temperature traps (50-170 °C); however, the majority of *s* values are not within the expected frequency range. Based on the observed behavior, one might expect additional traps or even a distribution of traps present in the inspected temperature range that cannot be resolved with the discussed methods. Potential analysis methods that could allow the extraction of more realistic *E* and *s* values are T_m-T_{stop} method and method of multiple heating rates with heating rate range between 0.1-1 °C. Unfortunately, these measurements cannot be performed with the current equipment.

Nevertheless, the TL analysis suggests that trap depth *E* is smaller for the polycrystalline ceramic than for the single crystal, indicating shallower traps in the polycrystalline YAG:Ce when compared to the single crystal.

Overall, a comparative investigation between polycrystalline ceramics and single crystal YAG:Ce scintillators revealed the following reasons for the lower performance of the polycrystalline ceramics:

- Lower optical transparency
- Higher level of structural disorder
- Higher luminescence self-absorption

Additionally, TL analysis suggested that polycrystalline ceramics have shallower traps than single crystal.

In order to further extend this analysis and highlight other reasons undermining the performance of polycrystalline scintillators, Ce-doped $Lu_3Al_5O_{12}$ is investigated as a structural analogy to YAG:Ce.

3.2 Comparative investigation of transparent ceramic and single crystal $Lu_3Al_5O_{12}$:Ce (LuAG:Ce) scintillators

Similar to YAG:Ce performance, literature review on LuAG:Ce presented in Chapter I (cf. Figure 1.3) shows that the average luminosity is ca. 20% higher for the single crystal than for polycrystalline ceramics. Luminosity is evaluated for the present samples relative to a BGO single crystal using several gamma-ray point sources (^{133}Ba, ^{137}Cs, ^{241}Am, ^{57}Co, ^{22}Na). These measurements are illustrated in Figure 3.15 for ^{22}Na. The relative light yield of the polycrystalline ceramic and single crystal as a function of gamma-ray energy is shown in Figure 3.16. Overall behavior shows that LuAG:Ce single crystal is ca. 20% brighter than BGO and ca. 2 times brighter than the polycrystalline ceramics, which qualitatively correlates with the literature reports in Figure 1.3 showing that the average value of light output is higher for LuAG:Ce single crystal than for polycrystalline ceramic. Both samples also present linear response as a function of energy.

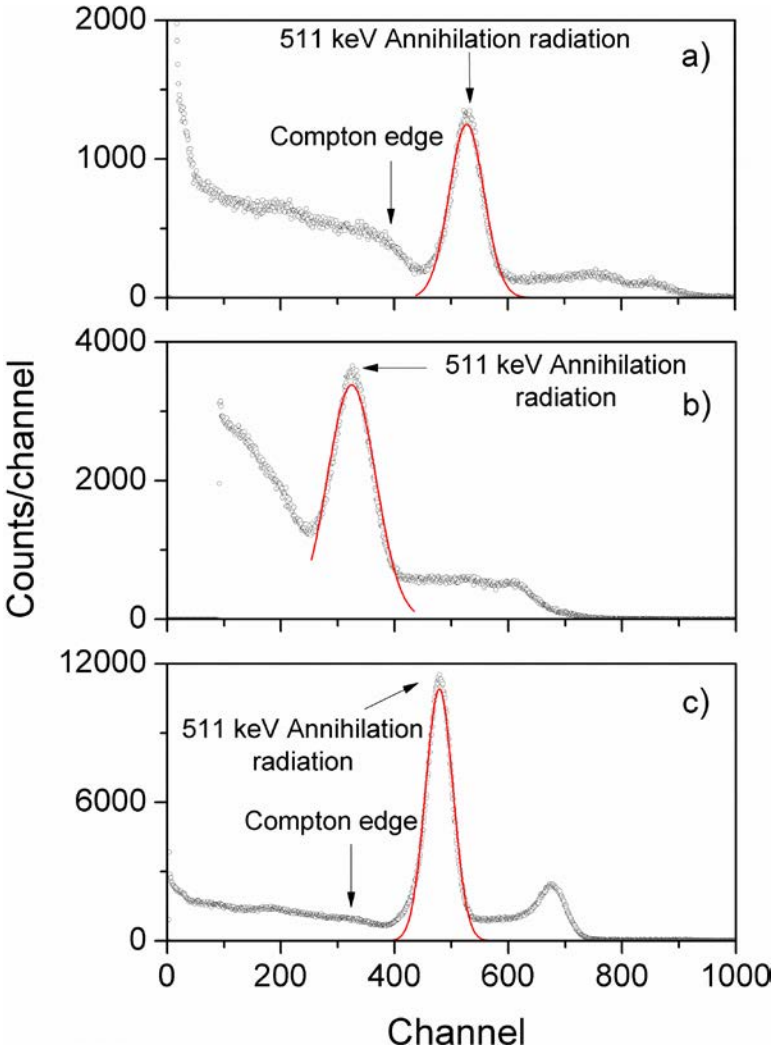

Figure 3.15. Pulse height spectra of γ-rays from ^{22}Na point source. (a) LuAG:Ce single crystal, (b) LuAG:Ce polycrystalline ceramic and (c) BGO single crystal. Black circles are the experimental data; red lines are Gaussian fits.

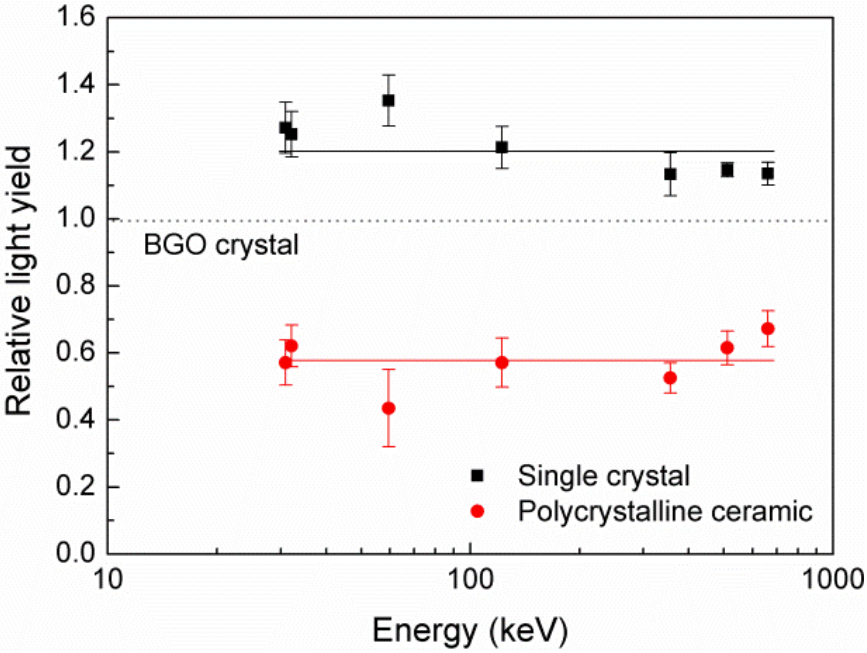

Figure 3.16. Light yield of LuAG:Ce single crystal (black squares) and polycrystalline ceramic (red circles) normalized to the light yield of a BGO crystal for each γ-ray energy used. The continuous lines indicate the average value.

The microstructure was investigated by means of infrared spectroscopy using ATR FTIR measurements. Figure 3.17 presents the spectra of the polycrystalline ceramic and single crystal normalized to the most intense peak at ca. 700 cm^{-1}. The structure of LuAG:Ce is composed of octahedral and tetrahedral sites occupied by Al and dodecahedral sites occupied by Lu (and Ce). The vibrational modes observed in the spectra in Figure 3.17 are correlated to the vibrations of these structural units. The absorption band at 410 cm^{-1} is assigned to the translational mode of the octahedral cations, the band at 445 cm^{-1} is a symmetric bend of the AlO_4 tetrahedra, the bands within ca. 470-600 cm^{-1} are the asymmetric bends of the tetrahedra, and the bands within 600-900 cm^{-1} are the asymmetric stretching modes of the tetrahedra [2, 34]. Broadening is observed in the majority of the bands of the polycrystalline ceramic relative to those of the single

crystal, with the FWHM of its bands being 4-5 cm^{-1} wider than for the crystal, as illustrated in the inset of Figure 3.17. These results indicated concurrent distortion of all three types of structural units. This could be understood by the shared nature of oxygen ions in the garnet structure, with each oxygen ion being bonded to two dodecahedra, one octahedron, and one tetrahedron, wherein tetrahedra and octahedra share edges with the dodecahedra [6].

Additionally, it is known for the garnet structure that an increase in the volume of the unit cell is related to a decrease of the frequency of the vibrational modes [4, 6], but no systematic shift of the bands of the polycrystalline ceramic is observed in relation to those of the single crystal. The ATR FTIR measurements probe a large number of grains and grain boundaries, but the results are dominated by the absorption of the grains due to the considerably larger volume of the grains in comparison with the volume of the grain boundaries. Consequently, these results showed the atomic network within the grains to be under identical conditions to those within the single crystal. The broadening of the absorption bands is, therefore, ascribed to variations of the interionic distances restricted to within the grain boundaries and indicates the presence of some level of structural disorder confined to the grain boundaries.

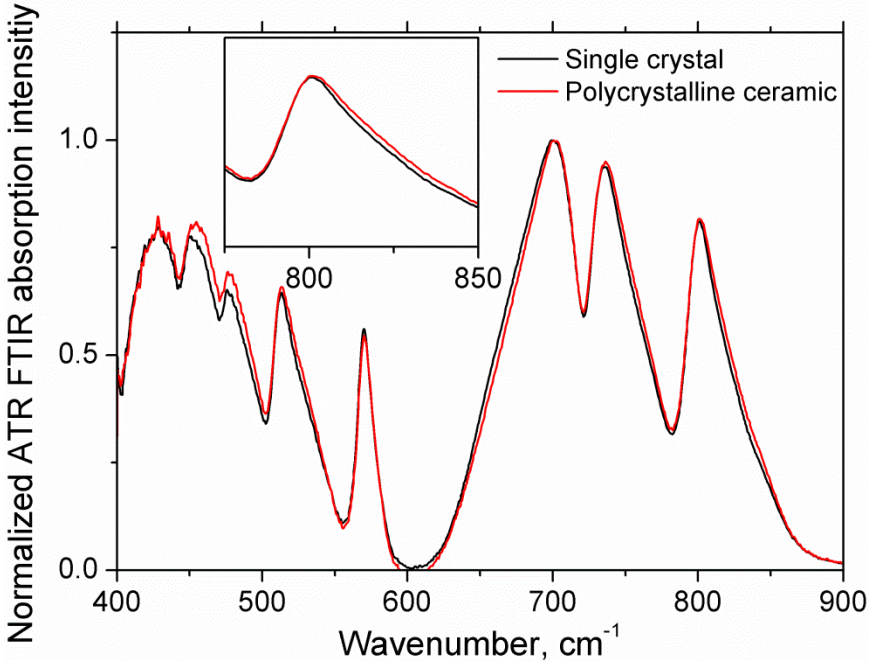

Figure 3.17. Normalized absorption ATR FTIR spectra of the LuAG:Ce single crystal and polycrystalline ceramic normalized to the most intense peak. The inset illustrates the difference in band width between the single crystal and polycrystalline ceramic.

Since the single crystal and polycrystalline ceramic are both visually transparent, their optical properties are investigated in detail. The results of optical transmission measurements are presented in Figure 3.18. Materials have absorption bands centered at about 2.76 and 3.55 eV (449 and 349 nm, respectively) that were assigned to the Ce^{3+} $4f \rightarrow 5d_1$ and $5d_2$ transitions, respectively [35]. Both samples also exhibit high optical transparency down to about 500 nm (2.48 eV) with transmission of the polycrystalline ceramic being lower (72%) than that of the single crystal (82%), most likely due to residual porosity after sintering. This is supported by the identification of residual porosity by means of positron annihilation spectroscopy measurements of several oxide polycrystalline ceramics either sintered at high temperatures or sintered and hot isostatically pressed (HIPed) [36, 37].

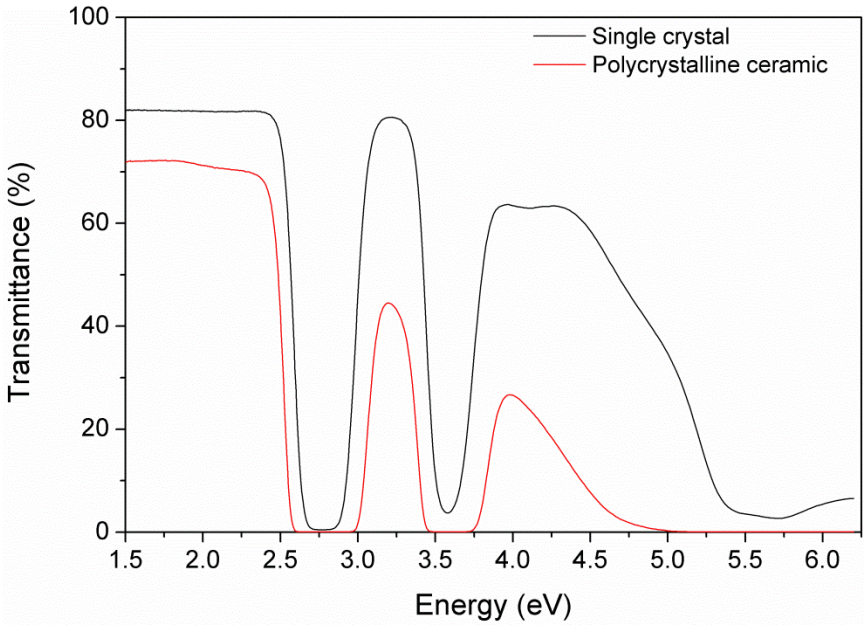

Figure 3.18. Optical transmission of LuAG:Ce single crystal and polycrystalline ceramic.

PLE spectra monitored at 2.43 eV (510 nm) and PL spectra excited at 3.53 eV (351 nm) of the single crystal and polycrystalline ceramic are presented in Figures 3.19a and 3.19b, respectively. The excitation bands match the position of the absorption bands observed in the optical transmission spectra (Figure 3.18) and are assigned to the $4f \rightarrow 5d_{1,2}$ electronic transitions of Ce^{3+}. The fine structure superimposed to the excitation band between 2.6-2.9 eV has been assigned to the sharp features from the Xe lamp used as the excitation source [9]. The FWHM of the PLE bands is ca. 1.3 times broader for the polycrystalline ceramic than for the single crystal due to inhomogeneous broadening, *i.e.* the $4f \rightarrow 5d$ transition is not shielded from the crystalline field thus presenting different spectroscopic characteristics depending on the local environment of the Ce^{3+} ion. The resulting enhanced self-absorption in the polycrystalline ceramic is found to be ca. 1.8 times higher than in the single crystal based on the ratio of the intersection area between the PL and PLE spectra within 2.4-2.8 eV divided by the total area of the PL spectrum.

PL spectra are composed of a broad band centered at around 2.43 eV. This band is deconvoluted into two Gaussian bands centered at 2.30 and 2.49 eV (Figures 3.19a and 3.19b). These bands are assigned to the $5d_1 \rightarrow 4f$ ($^2F_{5/2}$, $^2F_{7/2}$) transitions, with the ground state split into two levels due to spin-orbit coupling. The same split of ca. 0.18 eV is observed in both samples, as expected by the highly localized nature of the spin-orbit interaction not being affected by the local environment of the Ce^{3+} ions. A Stokes shift of ca. 0.34 eV is found in both the crystal and the polycrystalline ceramic. No difference in position and FWHM of the Gaussian bands is observed between the single crystal and the polycrystalline ceramic.

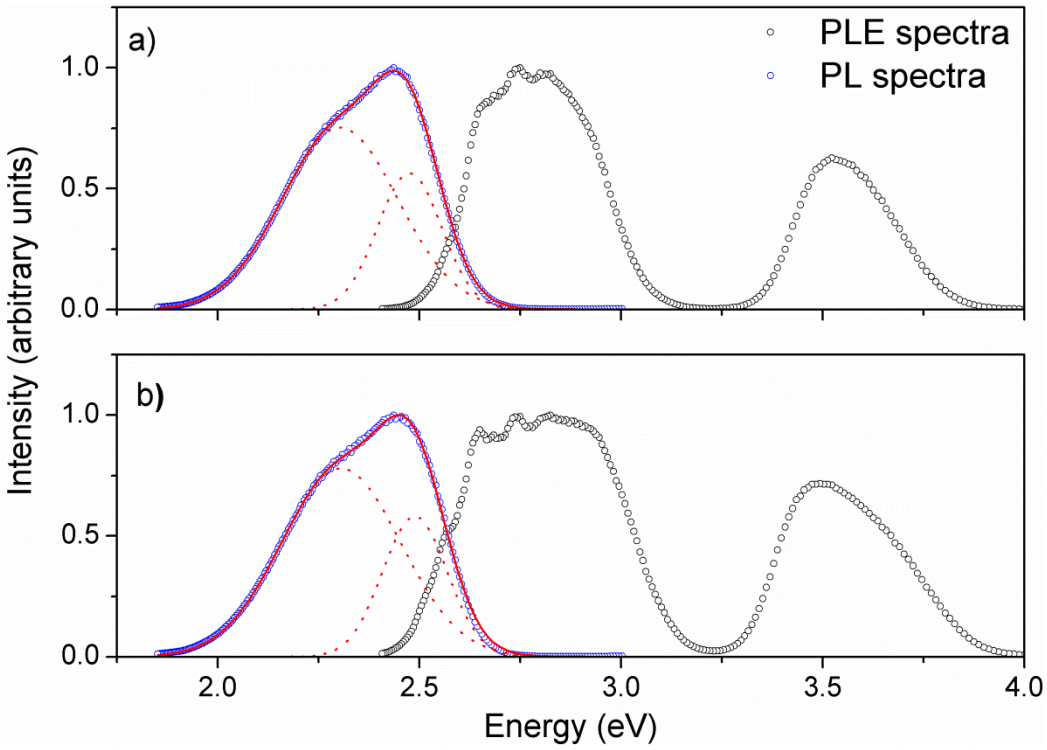

Figure 3.19. PL (blue circles) and PLE (black circles) spectra of a) single crystal, and b) polycrystalline ceramic. Gaussian deconvolution (red dotted lines) of PL spectra together with best fit (red continuous lines) are also shown.

Further investigation of luminescent properties is done by means of radioluminescence. RL spectra present an intense band peaked at ca. 2.43 eV that is assigned to the emission of Ce^{3+} (Figure 3.20a for the single crystal and Figure 3.20b for the polycrystalline ceramic). The results of the deconvolution of this band with two Gaussian bands are similar to the results of the deconvolution of the PL spectra and are not discussed further. RL measurements also revealed weaker emissions above ca. 3 eV. It has been noticed that the absorption bands of Ce^{3+} ions centered at 2.76 and 3.55 eV form two "peaks" in this region of the RL spectra [12, 38]. These "peaks", however, do not necessary correspond to individual defects but are the result of the partial absorption of the emission band of the defects by the Ce^{3+} ions [38, 39]. Accordingly, the observed drop of RL intensity centered at ca. 3.6 eV in the present RL spectra (Figures 3.20c and 3.20d) is explained by the absorption band of Ce^{3+} ions (*i.e.*, the $4f \rightarrow 5d_1$ transition), as shown in Figure 3.21, where the optical transmission and RL spectra of polycrystalline ceramic and single crystal are superimposed.

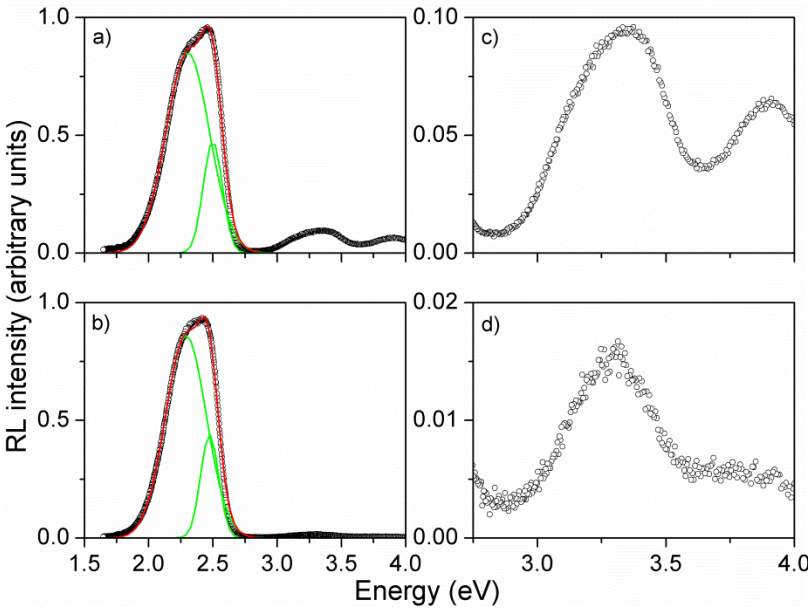

Figure 3.20. RL spectra (black circles) together with Gaussian deconvolution (green lines) and best fit (red lines) for the single crystal (a and c), and polycrystalline ceramic (b and d). Figures (c) and (d) highlight the weaker defect-related emission.

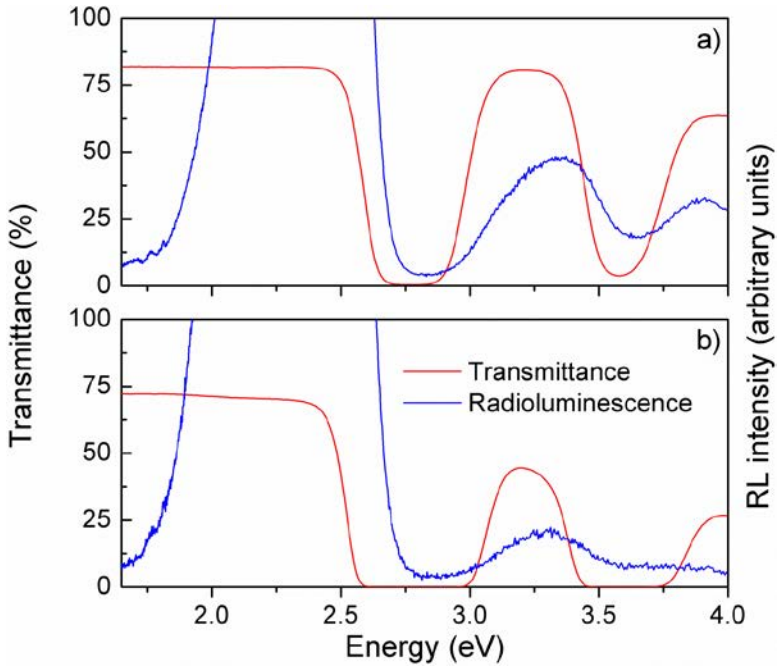

Figure 3.21. Superimposition of RL results (blue lines) and optical transmission results (red lines) for the a) single crystal, and b) polycrystalline ceramic.

According to previous investigations of LuAG, emission bands centered at 3.10 and 3.15 eV have been assigned to an F^+-type defect [40, 41], while emission at 2.99 eV has been related to the presence of oxygen vacancies [42]. Emission at 3.25 and 3.45 eV has been attributed to Ce occupying an Al site (Ce_{Al}), and emission at ca. 3.18 eV was related to Ce_{Al} perturbed by a defect in a nearby Lu site [43]. Emission bands within 4.13-4.28 eV have been attributed to the emission of excitons localized around Lu_{Al} antisite defects [12, 21, 44]. Moreover, a broad emission band within ca. 2.75-5.25 eV superimposed to the bands above has been assigned to the luminescence of Lu_{Al} antisite defects [12, 21, 38, 41]. According to a literature survey, the presence of F^+-type, Ce_{Al}, perturbed Ce_{Al}, and Lu_{Al} defects are compatible with the present results. While it is not possible to identify the presence of individual defects because spectra deconvolution is unreliable, RL results are used to quantify the relative concentration of defects in two samples by assuming the intensity of the RL band to be proportional to the concentration of the defects. Due to the difficulties in making absolute intensity measurements, the total intensity of the defect-related emission (2.85-4.0 eV) is normalized to the intensity of the Ce^{3+} band (1.65-2.85 eV) in each respective spectrum. This analysis shows a much weaker relative intensity of the defect-related band in the case of the polycrystalline ceramic (2 % of the Ce^{3+} band) compared to the single crystal (14 % of the Ce^{3+} band). Normalizing these results to the cerium concentration in each of the samples (the cerium concentration in the polycrystalline ceramic is 1.5 times the concentration in the single crystal), it was estimated that there are 11 times more luminescent defects in the single crystal than in the polycrystalline ceramic.

In order to obtain complementary data on defect-related emissions, additional PL and PLE measurements were performed. PLE measurements monitored at 2.95 eV and PL measurements excited at 3.53 eV are shown in Figures 3.22a and 3.22b for the single crystal and polycrystalline

ceramic, respectively. The PLE spectra are composed of three distinct bands at 3.43, 4.13, and 4.62 eV, and the PL spectra had a broad band peaked at 3.12 eV with a shoulder at 2.97 eV. Literature review of defect-related excitation and emission in LuAG is done in order to understand the nature of these bands (see Table 3.5). Based on these results, emission at 3.12 eV together with the excitation band at 3.43 eV are assigned to F^+-type center, while the 2.97 eV band is assigned to an unknown defect related to oxygen vacancies, in agreement with results reported for Czochralski-grown LuAG:Ce single crystals [42]. PL measurements excited at 4.13 and 4.62 eV yielded similar spectra as those excited at 3.43 eV. The band at 4.62 eV is found in good agreement with an unidentified excitation band at ca. 4.65 eV observed in an undoped Czochralski-grown LuAG single crystal annealed in H_2 atmosphere [40]. To the best of our knowledge, the excitation band at 4.13 eV has not been previously reported in the literature.

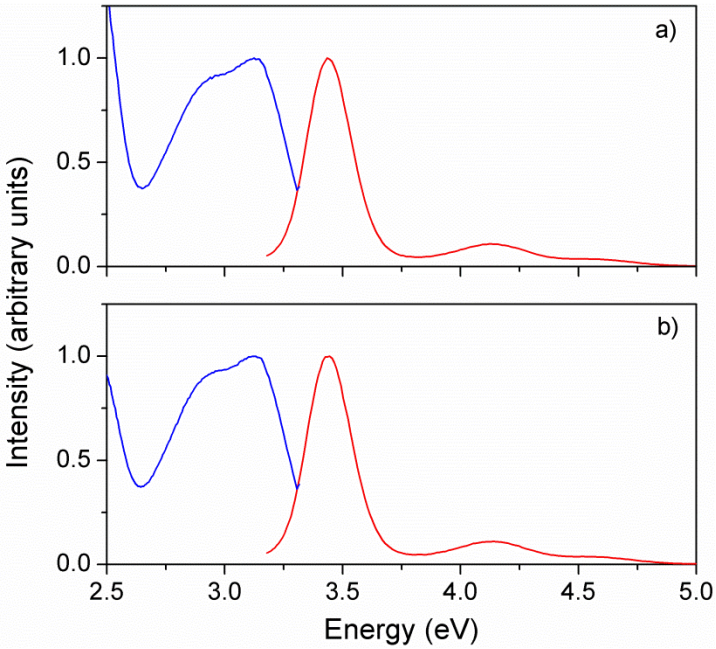

Figure 3.22. PLE spectrum monitored at 2.95 eV (420 nm; red), and PL spectrum excited at 3.53 eV (351 nm; blue) for a) single crystal and b) polycrystalline ceramic.

Table 3.5. Literature review of defect excitation and emission in LuAG and LuAG:Ce at room temperature in the order of increasing emission energy.

Type of material	Absorption/Excitation and defect type	Emission and defect type	Reference
Ce-doped crystal	3.32 eV (373 nm), 3.72 eV (333 nm), 4.29 eV (289 nm), 4.68 eV (265 nm) → V_O	2.61 eV (475 nm), 2.99 eV (415 nm) → V_O	[42]
Ce-doped nanoceramic	–	3.10 eV (400 nm) → F^+	[41]
Undoped crystal	3.40 eV (365 nm), 5.30 eV (234 nm), 6.10 eV (203 nm) → F^+	3.15 eV (394 nm) → F^+	[40]
Ce-doped ceramic (Lu-rich)	–	3.26 eV (380 nm) → Lu_{Al}	[45]
Ce-doped crystal	–	3.32 eV (374 nm) → ?	[12]
Ce-doped nanoceramic	–	3.65 eV (340 nm) → ?	[41]
Ce-doped crystal	–	3.70 eV (335 nm) → Lu_{Al}	[21]
Ce-doped ceramic	–	3.76 eV (330 nm) → Lu_{Al}	[35]
Ce-doped crystal	–	3.77 eV (329 nm) → Lu_{Al}	[12]
Ce-doped crystal	–	3.90 eV (318 nm) → Lu_{Al}	[38]
Ce-doped crystal	–	4.13 eV (300 nm) → LE at Lu_{Al}	[44]
Ce-doped crystal	–	4.22 eV (294 nm) → LE at Lu_{Al}	[21]
Ce-doped crystal	–	4.28 eV (290 nm) → LE at Lu_{Al}	[12]
Ce-doped nanoceramic	–	4.43 eV (280 nm) → ? 4.77 (260 nm) → unknown defect related to V_O	[41]

Further comparison between LuAG:Ce single crystal and ceramic scintillators is done by means of thermoluminescence. TL measurements of LuAG:Ce bulk single crystals grown by the micro-pulling and Czochralski methods as well as of LuAG:Ce single-crystalline films prepared by the liquid phase epitaxy (LPE) method have been reported previously. On the other hand, to the best of author's knowledge, results and analysis shown in the present work is the first TL investigation of a LuAG:Ce transparent polycrystalline ceramic. The summary of all the glow peaks, including present work, for measurements above room temperature [42, 46-51] is presented in Figure 3.23. Interestingly, not all the same glow peaks were observed in all samples. Within the temperature range of 15 ^{o}C or less, some glow peaks were consistently reported. Within 45-50 ^{o}C [46-49], 79-88 ^{o}C (present work and [47-49]), and 269-284 ^{o}C (present work and [47-49]), glow peaks were consistently observed in the samples prepared by Czochralski and micro-pulling methods, and within 97-110 ^{o}C (present work and [42, 50]) in samples prepared by Czochralski and LPE methods. All the glow peaks observed in the polycrystalline ceramic were also consistently observed in the samples prepared by Czochralski method (present work and [48, 49]). A larger number of glow peaks were consistently reported for the samples prepared by micro-pulling and Czochralski methods (typically 5-6 peaks [46-49]) than for the single-crystalline films (2 or 4 peaks [50, 51]) and the polycrystalline ceramic (2 peaks). Results by Douissard *et al.* [50] also showed that the number of glow peaks and the peak position are not affected by the Ce content, at least within 5-10 mol%. A possible source of discrepancy in the peak position of results reported from the single crystalline film studies is the heating rate, not reported in [50, 51] (all other results were obtained with a 1 ^{o}C/sec heating rate). Overall, these results suggested that different traps are created by different fabrication methods.

It is noted that in all cases but the present work, the number of peaks was extracted by visual analysis only with many of the reported glow peaks being considerably broad, especially for the samples prepared by LPE method. This approach allows for the presence of weaker glow peaks to go undetected by visual analysis. The present work involves a series of TL analysis methods, including the aforementioned visual analysis combined with McKeever-Chen model, decomposition by means of GlowFit software, and a combination of these two methods.

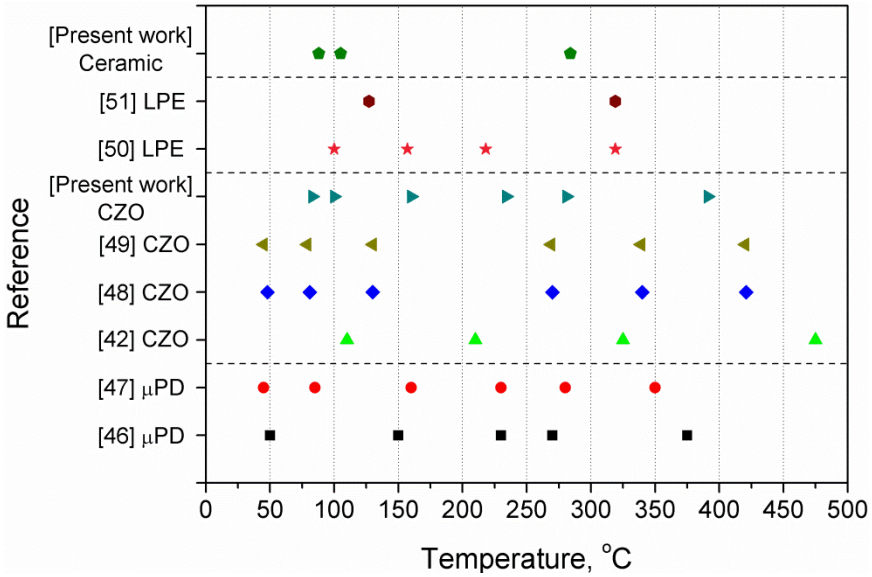

Figure 3.23. Comparison of the present results of TL peak positions to the literature on TL of LuAG:Ce [42, 46-51].

Representative results of mass-normalized TL measurements are shown in Figure 3.24. The glow curves are dominated by the emission within ca. 180-340 ^{o}C, together with glow peaks within 50-120 ^{o}C and 340-400 ^{o}C. Before analysis, TL results are corrected for luminescence (RL) thermal quenching by suitable linear best fits of the integral RL response as a function of temperature shown in the right inset of Figure 3.24. As a result, mass-normalized integrated TL

intensity is found to be ca. 1.6 times larger for the ceramic than that for the single crystal; however, this is explained by means of the difference in cerium concentration, which is 1.5 times larger for the ceramic than for the single crystal.

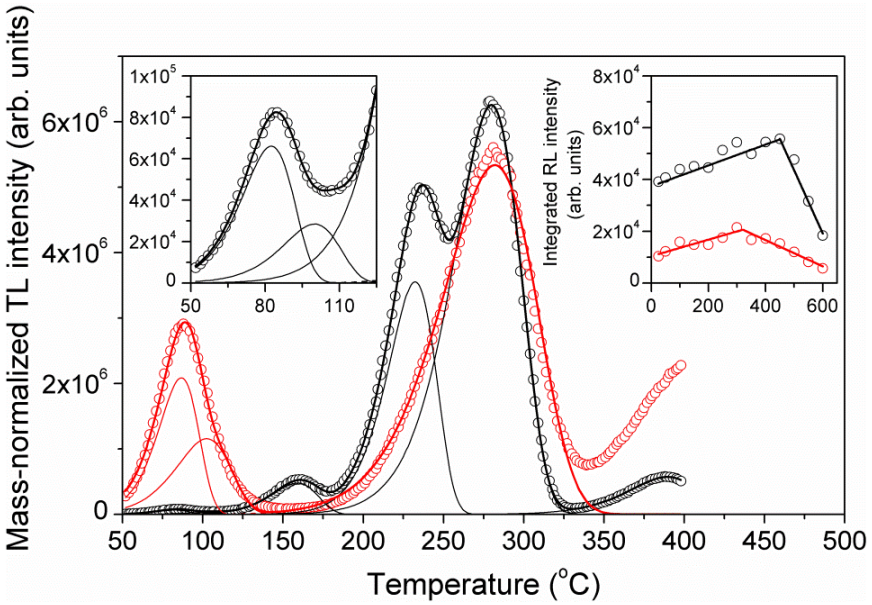

Figure 3.24. Mass-normalized TL glow curves of LuAG:Ce single crystal (black circles) and polycrystalline ceramic (red circles). The continuous lines are the best fit obtained with GlowFit software, and the dotted lines are the fit of the individual glow peaks. Left inset shows the glow curve and the results of the fitting procedure for the single crystal within 50-125 °C; right inset shows integral RL response as a function of temperature.

The order of kinetics of each glow peak is investigated employing X-ray irradiation with different durations, from 30 to 300 seconds, together with monitoring of the peak position. These results are shown in Figure 3.25 and reveal all glow peaks to have first-order kinetics due to the lack of a systematic shift of the peak position for increasing irradiation doses.

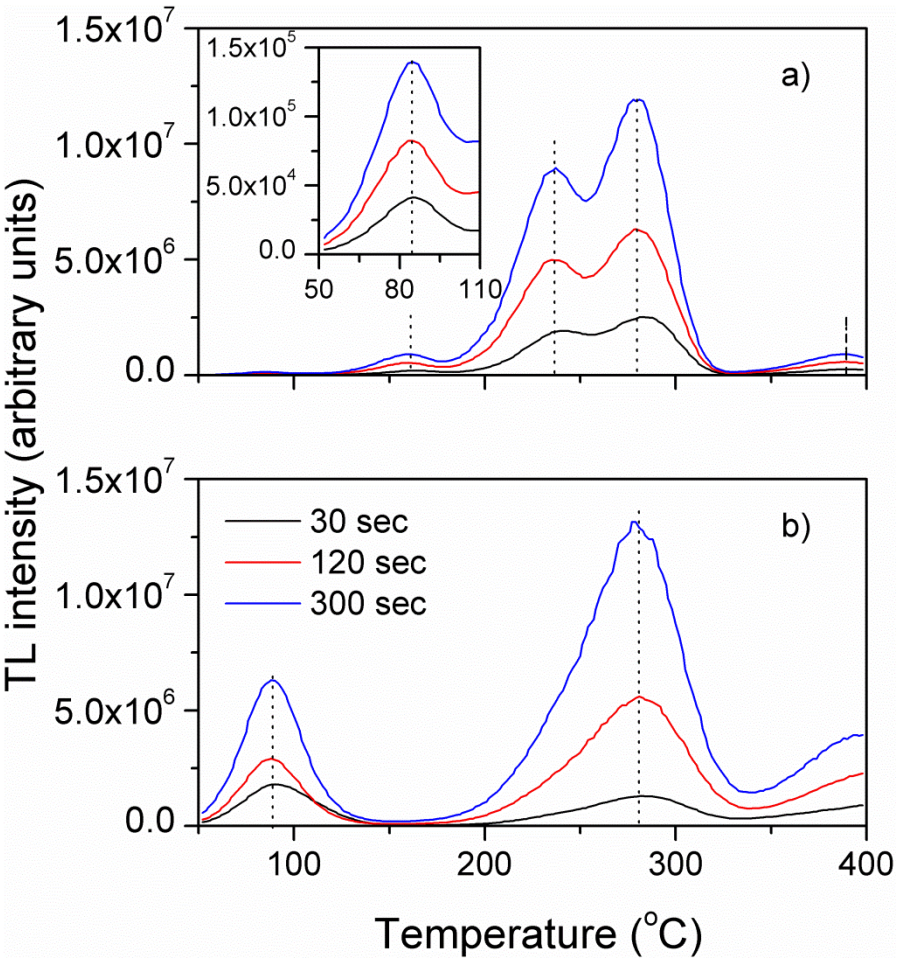

Figure 3.25. TL glow curves of a) single crystal, and b) polycrystalline ceramic obtained after irradiation with X-ray for different times. The vertical dotted lines are provided for clarity.

The glow curves are further analyzed using the aforementioned methods based on the first order of kinetics. The first method applies the expression (3.1) developed by McKeever and Chen [25, 26] and eq. (3.2) using visually extracted peak position, T_m, and FWHM of the experimental glow peaks. The results are presented in Table 3.6, where only values for the polycrystalline ceramic are calculated since FWHM cannot be extracted for the glow peaks of the single crystal.

Table 3.6. Parameters of the glow peaks and corresponding traps using McKeever-Chen expression.

McKeever-Chen formula			
	LuAG:Ce polycrystalline ceramic		
	FWHM, °C	*E*, eV	*s*, sec^{-1}
Peak at ~88 °C	38.4	0.72	$7.22x10^{8}$
Peak at ~280 °C	67.3	0.91	$5.66x10^{6}$

The second method of analysis is decomposing the experimental data with the GlowFit software [27]. The highest temperature glow peak of the polycrystalline ceramic cannot be fit with the software because its position is beyond the operational range of the TL reader. The best fit procedure confirmed the absence of glow peaks at 160 and 237 ^{o}C for the polycrystalline ceramic, and revealed the presence of two glow peaks within 50-120 ^{o}C for both samples. Figure 3.24 illustrates the best fit results for the 120 sec irradiation (continuous lines) for both the single crystal and the polycrystalline ceramic while Tables 3.7 and 3.8 summarize the peak positions, T_m, trap depth, *E*, and *s* values calculated based on eq. (3.2) for all irradiation times.

The third method uses eq. (3.1) with FWHM and T_m extracted from the fitting of each glow peak for the calculation of the trap depth. This analysis could not be done for the highest temperature glow peak because FWHM could not be determined. Tables 3.9 and 3.10 summarize the peak positions, T_m, trap depth, *E*, and calculated based on eq. (3.2) *s* values for all irradiation times.

Table 3.7. Summary of the analysis of glow curves of LuAG:Ce polycrystalline ceramic using GlowFit software for different irradiation times. "?" indicates values that could not be calculated; "-" indicates the glow peak was absent.

Irradiation time (s)	**Peak at ~88 °C**			**Peak at ~105 °C**			**Peak at ~160 °C**			**Peak at ~234 °C**			**Peak at ~281 °C**			**Peak at ~391 °C**		
	T_m (^{o}C)	E (eV)	s (sec^{-1})	T_m (^{o}C)	E (eV)	s (sec^{-1})	T_m (^{o}C)	E (eV)	s (sec^{-1})	T_m (^{o}C)	E (eV)	s (sec^{-1})	T_m (^{o}C)	E (eV)	s (sec^{-1})	T_m (^{o}C)	E (eV)	s (sec^{-1})
30	87	0.87	$1.2x10^{11}$	104	0.69	$9.4x10^{7}$	-	-	-	-	-	-	284	0.88	$3.0x10^{6}$	>400	?	?
120	89	0.88	$1.4x10^{11}$	107	0.67	$4.1x10^{7}$	-	-	-	-	-	-	285	0.90	$4.5x10^{6}$	>400	?	?
300	88	0.88	$1.5x10^{11}$	104	0.70	$1.3x10^{8}$	-	-	-	-	-	-	282	0.93	$9.7x10^{6}$	>400	?	?
Average	88	0.88	$1.4x10^{11}$	105	0.69	$8.8x10^{7}$	-	-	-	-	-	-	284	0.90	$5.7x10^{6}$	>400	?	?

Table 3.8. Summary of the analysis of glow curves of LuAG:Ce single crystal using GlowFit software for different irradiation times.

Irradiation time (s)	**Peak at ~88 °C**			**Peak at ~105 °C**			**Peak at ~160 °C**			**Peak at ~234 °C**			**Peak at ~281 °C**			**Peak at ~391 °C**		
	T_m (^{o}C)	E (eV)	s (sec^{-1})	T_m (^{o}C)	E (eV)	s (sec^{-1})	T_m (^{o}C)	E (eV)	s (sec^{-1})	T_m (^{o}C)	E (eV)	s (sec^{-1})	T_m (^{o}C)	E (eV)	s (sec^{-1})	T_m (^{o}C)	E (eV)	s (sec^{-1})
30	84	1.04	$4.5x10^{13}$	100	0.99	$1.9x10^{12}$	163	1.13	$7.9x10^{11}$	237	1.44	$1.1x10^{13}$	282	1.27	$1.6x10^{10}$	391	1.75	$8.8x10^{11}$
120	83	1.01	$1.3x10^{13}$	100	1.03	$7.0x10^{12}$	159	1.10	$4.6x10^{11}$	233	1.45	$1.8x10^{13}$	280	1.24	$9.3x10^{9}$	390	1.73	$6.4x10^{11}$
300	83	1.02	$2.5x10^{13}$	101	1.06	$1.7x10^{13}$	159	1.08	$2.6x10^{11}$	233	1.48	$3.7x10^{13}$	280	1.30	$3.4x10^{10}$	393	1.52	$1.3x10^{10}$
Average	83	1.02	$2.8x10^{13}$	100	1.03	$8.6x10^{12}$	160	1.10	$5.0x10^{11}$	234	1.45	$2.2x10^{13}$	281	1.27	$2.0x10^{10}$	391	1.67	$5.1x10^{11}$

Table 3.9. Summary of the analysis of glow curves of LuAG:Ce polycrystalline ceramic using combination of GlowFit software and McKeever-Chen formula for different irradiation times. "?" indicates values that could not be calculated; "-" indicates the glow peak was absent.

Irradiation time (s)	**Peak at ~88 °C**			**Peak at ~105 °C**			**Peak at ~160 °C**			**Peak at ~234 °C**			**Peak at ~281 °C**			**Peak at ~391 °C**		
	FWHM (^{o}C)	*E* (eV)	*s* (sec^{-1})	FWHM (^{o}C)	*E* (eV)	*s* (sec^{-1})	FWHM (^{o}C)	*E* (eV)	*s* (sec^{-1})	FWHM (^{o}C)	*E* (eV)	*s* (sec^{-1})	FWHM (^{o}C)	*E* (eV)	*s* (sec^{-1})	FWHM (^{o}C)	*E* (eV)	*s* (sec^{-1})
30	33.3	0.87	$1.2x10^{11}$	40.8	0.68	$6.7x10^{7}$	-	-	-	-	-	-	67.4	0.89	$3.7x10^{6}$	>400	?	?
120	34.1	0.89	$1.9x10^{11}$	40.6	0.69	$7.8x10^{7}$	-	-	-	-	-	-	69.2	0.88	$2.9x10^{6}$	>400	?	?
300	33.3	0.89	$2.1x10^{11}$	41.1	0.70	$1.3x10^{8}$	-	-	-	-	-	-	65.8	0.92	$7.2x10^{6}$	>400	?	?
Average	33.6	0.88	$1.7x10^{11}$	40.8	0.69	$9.2x10^{7}$	-	-	-	-	-	-	67.5	0.90	$4.6x10^{6}$	>400	?	?

Table 3.10. Summary of the analysis of glow curves of LuAG:Ce single crystal using combination of GlowFit software and McKeever-Chen formula for different irradiation times. "?" indicates values that could not be calculated.

Irradiation time (s)	**Peak at ~88 °C**			**Peak at ~105 °C**			**Peak at ~160 °C**			**Peak at ~234 °C**			**Peak at ~281 °C**			**Peak at ~391 °C**		
	FWHM (^{o}C)	*E* (eV)	*s* (sec^{-1})	FWHM (^{o}C)	*E* (eV)	*s* (sec^{-1})	FWHM (^{o}C)	*E* (eV)	*s* (sec^{-1})	FWHM (^{o}C)	*E* (eV)	*s* (sec^{-1})	FWHM (^{o}C)	*E* (eV)	*s* (sec^{-1})	FWHM (^{o}C)	*E* (eV)	*s* (sec^{-1})
30	24.8	1.06	$8.8x10^{13}$	34.2	0.95	$5.4x10^{12}$	34.0	1.14	$1.0x10^{12}$	35.8	1.45	$1.4x10^{13}$	49.6	1.28	$2.0x10^{10}$	?	?	?
120	25.4	1.02	$1.4x10^{13}$	27.4	1.04	$9.6x10^{12}$	34.2	1.11	$6.1x10^{11}$	36.6	1.46	$2.3x10^{13}$	48.8	1.24	$9.3x10^{9}$	?	?	?
300	25.3	1.03	$2.2x10^{13}$	30.6	1.08	$3.2x10^{13}$	34.9	1.09	$3.5x10^{11}$	35.1	1.49	$4.6x10^{13}$	47.3	1.31	$4.3x10^{10}$	?	?	?
Average	25.2	1.04	$4.1x10^{13}$	30.7	1.02	$1.6x10^{13}$	34.4	1.11	$6.5x10^{11}$	35.8	1.47	$2.8x10^{13}$	48.6	1.28	$2.4x10^{10}$	?	?	?

For all of the discussed methods, the acceptable ranges of values of *E* and *s* are 0.8-1.2 eV and 10^{12}-10^{14} sec^{-1}, respectively. It can be seen that most of the *E* values in the Tables 3.6-3.10 are within acceptable range; however, most of the *s* values significantly deviate from the expected range. This can be understood by looking at the dependence of the FWHM of the glow peaks on the peak temperature. Using eq. (3.1), function FWHM (*T*) can be plotted for different energy values, as shown in Figure 3.26. Comparing the experimental values of FWHM with expected values from Figure 3.26, one can see that in most of the cases experimental values do not match the extracted ones (*e.g.*, experimental glow peak at ca. 88 °C of the polycrystalline ceramic (red circles in Figure 3.24) has FWHM = 36.9 °C, while range of calculated FWHM at this temperature is 24.4-31.8 °C; glow peak at ca. 105 °C of the polycrystalline ceramic revealed by means of deconvolution has FWHM = 40.8 °C, while range of calculated FWHM at this temperature is 26.6-35.9 °C). This confirms a possibility of additional traps or even a distribution of traps present in the inspected temperature range that cannot be resolved, similar to a discussion on YAG:Ce. Additional TL methods using different methods of analysis need to be performed, which is not available with the current equipment.

Nonetheless, TL analysis applied in the present work suggests that LuAG:Ce polycrystalline ceramic has lower activation energy of the traps than that of the single crystal, as shown in Figure 3.27.

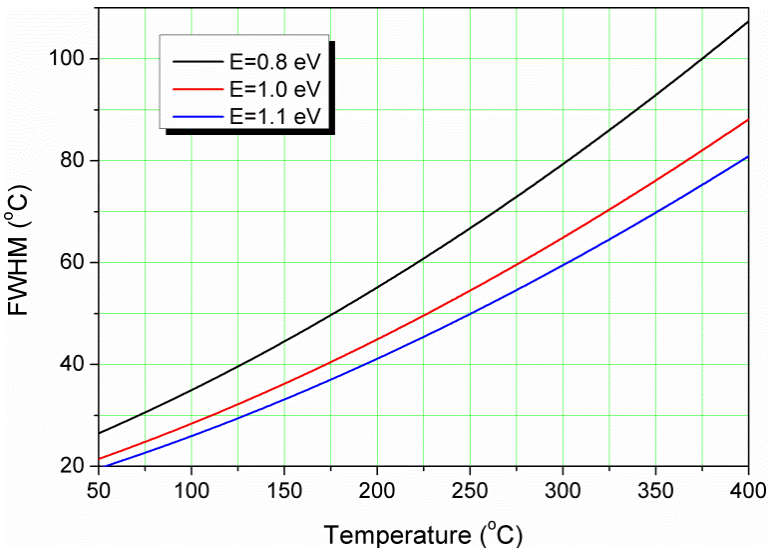

Figure 3.26. Dependence of the FWHM of the glow peaks on the peak temperature, according to eq. (3.1).

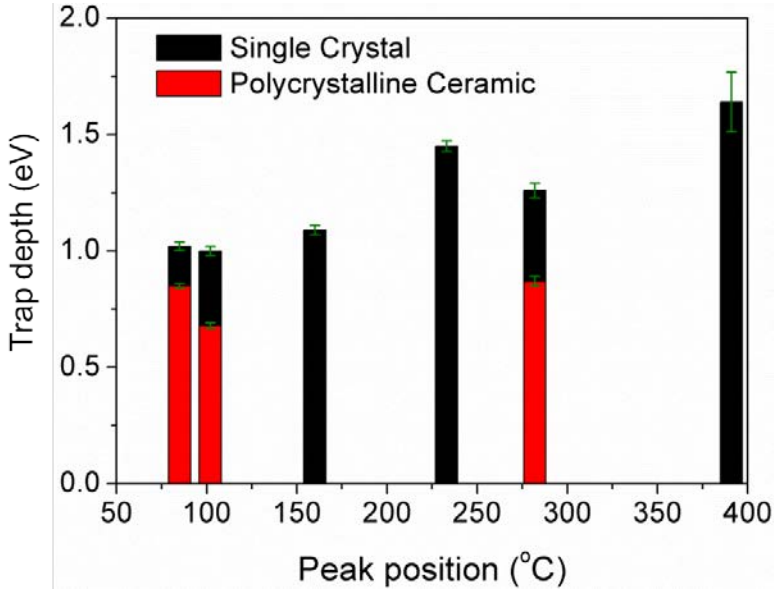

Figure 3.27. Activation energy, *E*, of the traps in LuAG:Ce single crystal and polycrystalline ceramic for different peak positions, T_m.

Overall comparative investigation between polycrystalline ceramic and single crystal LuAG:Ce scintillators reveals following reasons for the lower performance of the polycrystalline ceramics:

- Lower optical transparency
- Higher level of structural disorder
- Higher luminescence self-absorption

TL analysis suggests that the polycrystalline ceramic have shallower traps than the single crystal.

To evaluate how these factors depend on the particular dopant and fabrication of the garnet scintillators, Pr-doped LuAG sintered at several different temperature is investigated.

3.3. Microstructure and optical and luminescence properties of $Lu_3Al_5O_{12}$:Pr (LuAG:Pr)

LuAG:Pr polycrystalline ceramics fabricated at different sintering temperatures (1400, 1500, 1600, 1700 °C) are prepared by M.R. Marchewka as part of his MSc thesis. For completeness, density, grain size, and XRD results obtained by M.R. Marchewka are briefly presented here. The dependence of the relative density of the polycrystalline ceramics on the sintering temperature is determined according to Archimedes method. Achievement of high density is one of the crucial fabrication aspects for scintillating ceramics, as it is responsible for the stopping power (efficiency of the absorption of ionizing radiation) of a scintillator, as well as transparency of the material to the emitted light. The investigated polycrystalline ceramics exhibit linear dependence of the density on sintering temperature, achieving a highest value of 93.2±2.2% of the theoretical density at 1700 °C (Figure 3.28A).

Average grain size measurements are based on SEM images and calculated according to ASTM E 112-96 [52, 53]. Increase of the average grain size from 0.38 to 1.9 μm is observed for samples sintered from 1400°C to1700°C (Figure 3.28B). These grain size values are found to be in agreement with those reported in the literature [54-56]. Additionally, by means of EDX analysis, the concentration of Pr in the polycrystalline ceramics was estimated to be 0.18±0.012 at.% [57].

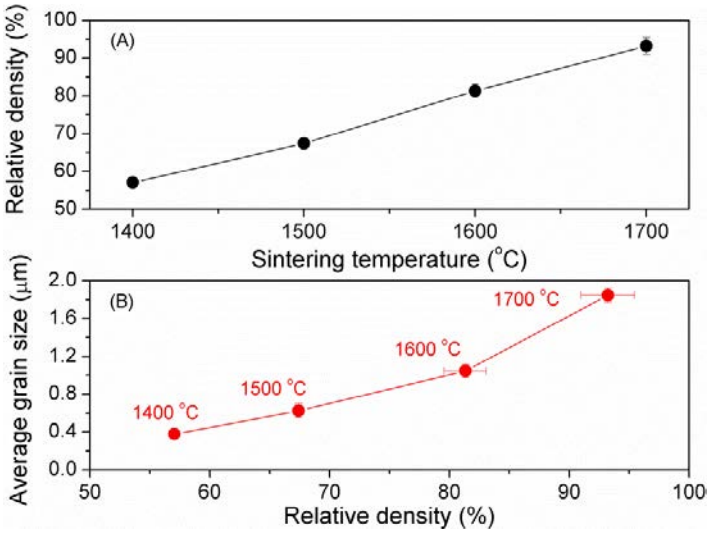

Figure 3.28. (A) Evolution of the density of LuAG:Pr polycrystalline ceramic as a function of sintering temperature; (B) Average grain size as a function of the relative density. Horizontal error bars show the variation of the relative density.

Diffractograms of LuAG:Pr polycrystalline ceramics, obtained by means of XRD, were matched to PDF (Powder Diffraction File) card no. 01-073-1368, confirming that the cubic garnet phase has been obtained in all sintered samples. The possibility of the formation of the unwanted, secondary phases like Pr_2O_3 and $PrAlO_3$ was also investigated by performing detailed scans of 2θ values within the region between 16° and 36° (Figure 3.29A) where the most intense

peaks of these secondary phases would be. The presence of the secondary phases was not detected, and the reduction of the amorphous phase as sintering temperature increases from 1400°C to 1700°C was observed. Furthermore, comparison of the width of XRD peaks at different sintering temperatures shows narrowing of observed peaks as a function of increasing temperature (Figure 3.29B), which reveals lower structural disorder in the polycrystalline ceramics sintered at higher temperatures. Additionally, the lattice parameter as a function of the sintering temperature was calculated based on the XRD results. The lattice parameter value was found to increase for higher sintering temperatures until reaching the reported value for LuAG, according to PDF card no. 01-073-1368 (Figure 3.29C). The increase of the lattice parameter towards the PDF reported value reveals the relaxation of the atomic network through the relief of residual compressional stress for higher sintering temperatures.

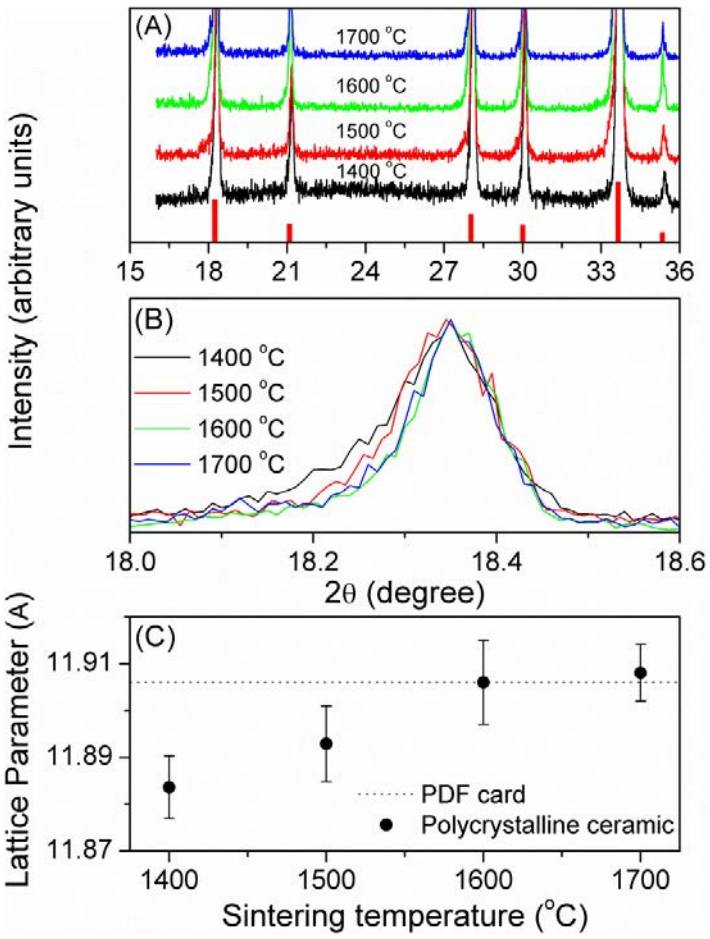

Figure 3.29. (A) XRD investigation of LuAG:Pr polycrystalline ceramics as a function of sintering temperature. PDF card no. 01-073-1368 is shown as red bars at the bottom of the figure; (B) Comparison of the width of the XRD peak at different sintering temperatures. The right sides of the peaks are matched in order to highlight the difference in width; (C) Lattice parameter of polycrystalline LuAG:Pr as a function of sintering temperature.

Infrared spectroscopy is used to gain further insights into the microstructure of LuAG:Pr by means of ATR FTIR measurements. Figure 3.30 presents the spectra of the polycrystalline ceramics and the single crystal normalized to the most intense peak at ca. 700 cm^{-1}. The vibrational modes observed in the spectra are identical to those discussed for LuAG:Ce and are

assigned accordingly. It is noted that the increase of the sintering temperature changes the shape and relative intensity of the ATR FTIR spectra of the polycrystalline ceramics towards the spectrum of the single crystal with the specimen sintered at 1700 °C having the majority of the peaks with the same or similar shape, intensity, and position to the reference LuAG:Pr single crystal. The observed changes indicate modifications within the structural units of the polycrystalline ceramics, with the increase of the sintering temperature leading to the change of the polycrystalline ceramic structure towards the direction of highly ordered crystal structure. This conclusion is also supported by results for the lattice parameter as a function of sintering temperatures, as discussed earlier.

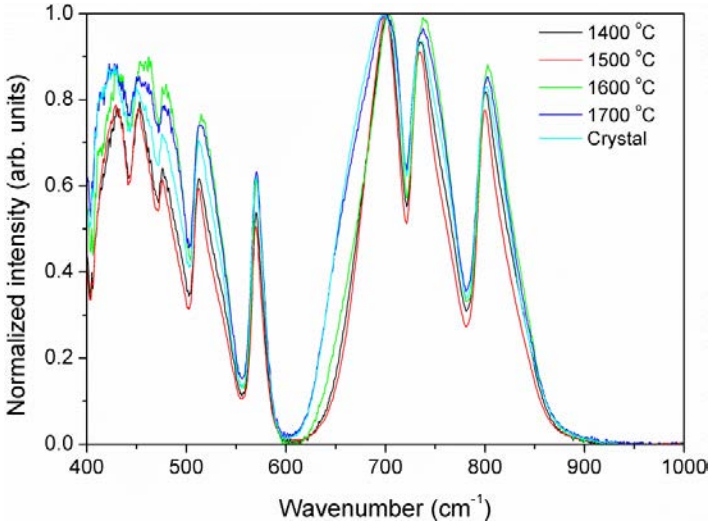

Figure 3.30. ATR FTIR spectra of LuAG:Pr single crystal and polycrystalline ceramics fabricated at various sintering temperatures.

Optical transmission measurements of the polycrystalline ceramics fabricated at different sintering temperatures are shown in Figure 3.31. Fabrication temperature clearly affects transmission of ceramics in the visible and ultraviolet regions. It is observed that the increase of

the sintering temperature is advantageous in increasing the transparency of the resultant material. The highest temperature investigated (1700 °C) allows for the resolution of the two absorption bands at ca. 255 nm (4.86 eV) and 295 nm (4.20 eV), which are assigned to *4f* ($^3H_4$) → *5d*$_{1,2}$ transitions of Pr^{3+} [58, 59]. The numerous sharp absorption bands in the range of 420-500 nm (2.48-2.95 eV) and 570-620 nm (2.00-2.18 eV) can be observed from the sample sintered at as low as 1500 °C with the absorption becoming more pronounced as the temperature increases. These bands are assigned to multiple *4f* → *4f* electronic transitions of the Pr^{3+} dopant [54, 58].

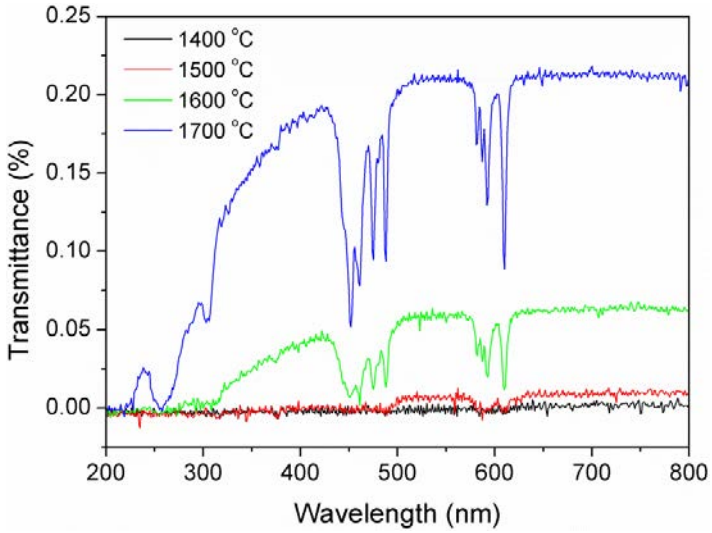

Figure 3.31. Transmission spectra of LuAG:Pr polycrystalline ceramics fabricated at various sintering temperatures.

4f → *5d* and *4f* → *4f* absorption bands observed in the transmission spectra result in an excitation of Pr^{3+} in the LuAG matrix that eventually leads to de-excitation of the dopant and emission of light. This emission is explored by means of radioluminescence. Figure 3.32A presents normalized RL spectra of the single crystal and polycrystalline ceramics obtained with the use of different sintering temperatures. All investigated samples show the clear presence of *5d* → *4f* transitions (ca. 2.7–4.4 eV) and *4f* → *4f* transitions (ca. 1.65–2.7 eV) [55, 60].

Evaluation of the ratio of integrated intensities of emission from aforementioned transitions (Figure 3.32B) shows that the increase of the sintering temperature favors *5d* → *4f* transitions relative to *4f* → *4f* transitions. This phenomenon can be understood by comparing the energies and nature of the *4f* and *5d* levels of Pr^{3+} ion in the host material. *4f* levels are shielded from the influence of the surrounding host matrix, which results in the minimization of the crystal field influence on the *4f* → *4f* transitions. On the other hand, since *5d* levels lack shielding provided by outer electrons, the *5d* → *4f* transitions are greatly affected by the chemical and crystallographic nature of the host [61]. Thus, the relief of the residual stress in the atomic network and decrease of the structural disorder that were shown to progressively happen for higher sintering temperatures is expected to affect *5d* → *4f* transitions relatively more than the *4f* → *4f* transitions, asymptotically approaching the ratio for the single crystal.

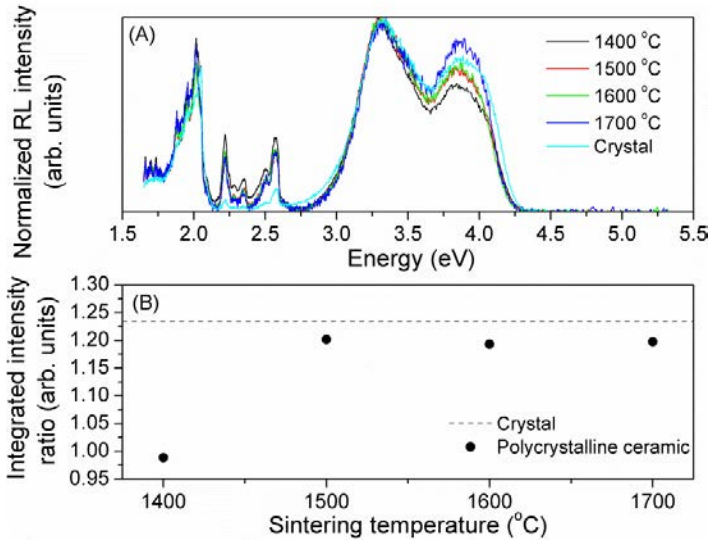

Figure 3.32. (A) RL spectra of LuAG:Pr normalized to the most intense peak at ca. 3.3 eV; (B) Ratio of the integrated intensities of emission from *5d* → *4f* transitions (integrated from ca. 2.72-5.38 eV) to *4f* → *4f* transitions (integrated from ca. 1.65–2.72 eV) of Pr^{3+} as a function of sintering temperature.

Further investigation of *5d* → *4f* transitions of Pr^{3+} using deconvolution of the experimental RL spectra with Gaussian bands revealed the four existing transitions from the *5d* state to $^3F_{3(4)}$, $^3H_6$, $^3H_5$, $^3H_4$ *4f* states, with maxima at 3.26±0.01 eV, 3.41±0.02 eV, 3.84±0.01 eV, 4.04±0.02 eV, respectively (Figures 3.33A-E) [59, 62, 63]. These results suggest that the sintering temperature does not affect the position or number of observed *5d* → *4f* transitions; however, change of the sintering temperature might affect the relative intensity of these transitions. This possibility is explored by evaluating integrated intensities of *5d* → $^3F_{3(4)}$ (black squares), *5d* → $^3H_6$ (red circles), *5d* → $^3H_5$ (blue triangles), and *5d* → $^3H_4$ (purple rhombus) transitions relative to the total integrated RL intensity of *5d* → *4f* transitions of Pr^{3+} (Figure 3.33F). The *5d* → $^3F_{3(4)}$ transition is the least affected transition, with the relative intensity ratio staying almost constant with sintering temperature and coinciding with the value obtained for the single crystal (black dash line). On the contrary, the fabrication of LuAG:Pr polycrystalline ceramics at higher sintering temperatures affects *5d* → $^3H_{6(5,4)}$ transitions changing their relative intensity towards respective values for the single crystal. This behavior reflects the changes observed within the microstructure (*i.e.*, higher density, lower residual stress of the atomic network, lower structural disorder) as it relaxes to the single crystal.

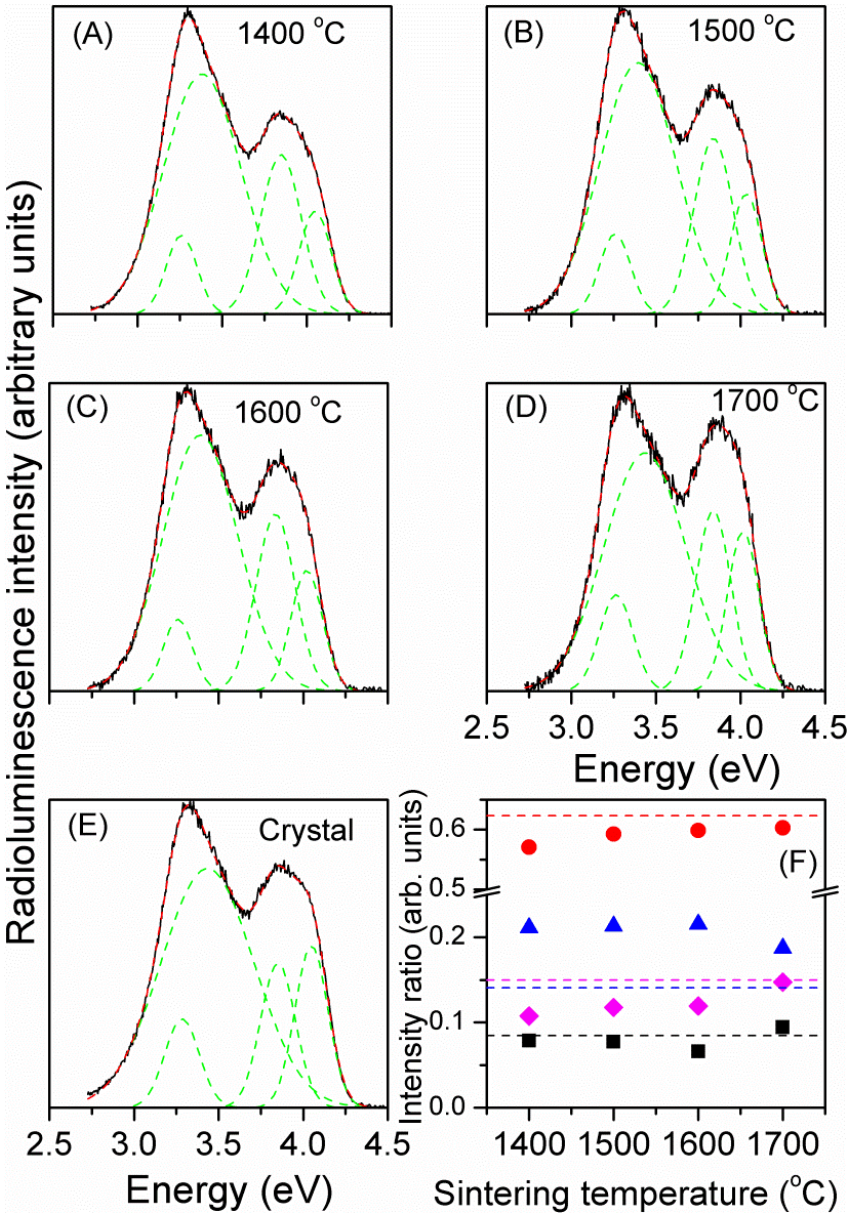

Figure 3.33. RL spectra (black curves) of polycrystalline ceramics sintered at (A) 1400 °C, (B) 1500 °C, (C) 1600 °C, (D) 1700 °C, and (E) RL spectra of the single crystal together with the best fit of each spectrum (red curves) and the individual Gaussian bands (green curves) used in the deconvolution. Only $5d \rightarrow 4f$ transitions are shown. (F) Integrated intensities of $5d \rightarrow {}^3F_{3(4)}$ (black squares), $5d \rightarrow {}^3H_6$ (red circles), $5d \rightarrow {}^3H_5$ (blue triangles)), and $5d \rightarrow {}^3H_4$ (purple rhombs) transitions relative to the total integrated intensity. Values of the ratios for the single crystal are shown as dash lines of the corresponding color.

In order to gain further insight into the effect of the sintering temperature, luminescence is investigated under UV excitation (photoluminescence). Figure 3.34 shows excitation and the corresponding emission spectra of the investigated LuAG:Pr. In Figure 3.34A, the emission bands between 2.75-4.25 eV correspond to $5d \rightarrow 4f$ transitions, which were already observed by means of RL, with a very minor contribution from $4f \rightarrow 4f$ transitions around 2.54 eV. Excitation bands that lead to this emission are located around 4.26 eV and 4.99 eV and are assigned to the two lowest $4f\ (^3H_4) \rightarrow 5d_{1,2}$ transitions of Pr^{3+}, respectively [59]. It is interesting to note that the position of the higher-energy excitation band (at 4.99 eV) appears to be independent of the sintering temperature, while the lower-energy excitation band continuously shifts from ca. 4.32 eV to 4.20 eV as the temperature increases.

Besides $5d \rightarrow 4f$ transitions, Pr^{3+} also exhibits $4f \rightarrow 4f$ transitions, which are presented in Figure 3.34B. Emission bands can be seen from 1.61 eV to 2.65 eV and are identified in Table 3.11 [60]. Peak positions are the same for all samples and independent of the sintering temperature due to the shielding of *4f* levels [61]. The temperature seems to have an effect on the intensity of the emission bands, increasing the intensity for higher temperatures. This is, most probably, related to the improved microstructure at higher sintering temperatures that resulted in the decrease of possible light loss pathways, increasing the emission intensity. $4f \rightarrow 4f$ excitation bands are observed between 2.6-3.0 eV, where the most intense band is located at 2.74 eV and corresponds to $^3H_4 \rightarrow {}^3P_2$ transition [64]. It is also noted that the excitation spectra have bands between 4.0-5.0 eV, which are a minor contribution from $4f \rightarrow 5d$ transitions, as well as, a band between 3.0-3.75 eV, which is due to defects and is further investigated.

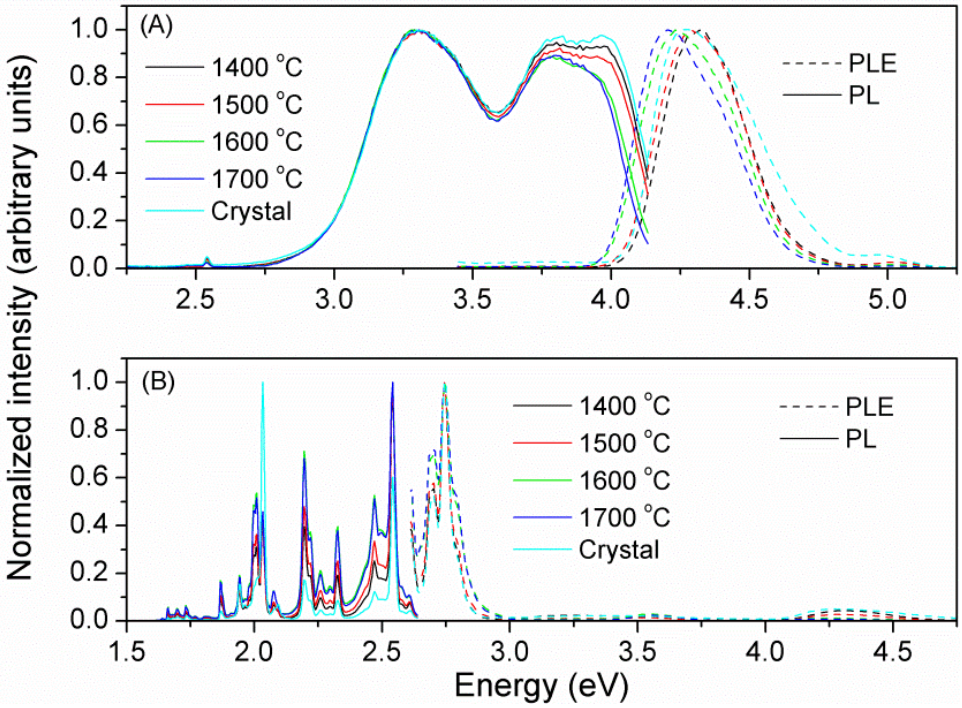

Figure 3.34. Normalized emission (PL; solid lines) and excitation (PLE; dashed lines) spectra of LuAG:Pr polycrystalline ceramics and single crystal. (A) Spectra corresponding to *4f* → *5d* and *5d* → *4f* transitions of Pr^{3+}. PLE spectra were monitored at 3.31 eV, and PL spectra were excited at 4.28 eV; (B) Spectra corresponding to *4f* → *4f* transitions of Pr^{3+}. PLE spectra were monitored at 2.54 eV, and PL spectra were excited at 2.74 eV.

Table 3.11. *4f → 4f* transitions observed in PL measurements of LuAG:Pr [60].

Energy (eV)	Transition
1.66	$^3P_0 \rightarrow {}^3F_4$
1.70	?
1.73	$^3P_1 \rightarrow {}^3F_4$
1.77	$^1D_2 \rightarrow {}^3H_5$
1.80	$^3P_1 \rightarrow {}^3F_3$
1.88	$^3P_2 \rightarrow {}^3F_4$
1.94	$^3P_0 \rightarrow {}^3F_2$
1.96	$^3P_2 \rightarrow {}^3F_3$
2.00	$^3P_1 \rightarrow {}^3F_2$
2.01	$^3P_0 \rightarrow {}^3H_6$
2.03	$^1D_2 \rightarrow {}^3H_4$
2.07	$^3P_1 \rightarrow {}^3H_6$
2.19	$^3P_2 \rightarrow {}^3H_6$
2.22	?
2.26	($^3P_0 \rightarrow {}^3H_5$) ?
2.33	$^3P_1 \rightarrow {}^3H_5$
2.47	$^3P_2 \rightarrow {}^3H_5$
2.54	$^3P_0 \rightarrow {}^3H_4$
2.61	$^3P_1 \rightarrow {}^3H_4$

In order to understand the origin of the unknown excitation band between 3.0-3.75 eV in Figure 3.34B, its peak position is used to obtain PL spectra and corresponding PLE spectra (Figure 3.35). PL is dominated by the band with the maximum at ca. 2.95 eV and a contribution from *4f → 4f* emission between 1.69–1.91 eV. Sharp features observed at 2.51–2.72 eV matched well the positions of *4f → 4f* absorption bands, meaning that there is energy transfer between the *4f → 4f* transitions of Pr^{3+}. The corresponding PLE spectra show excitation bands at ca. 3.30 eV and between 4.0–5.25 eV. The latter corresponds to the *4f → 5d* transitions of Pr^{3+} and shows that there is an energy transfer from Pr^{3+} to the observed defect. This situation is highly

unfavorable for the scintillation process as it results in a light loss and decreases the efficiency of LuAG:Pr as a scintillator. Thus, it is important to identify the aforementioned defect. It is reported for LuAG:Pr, that the F^+-type centers absorb at ca. 3.31 eV [65, 66], which is close to the position of the observed excitation band. However, the emission band of F^+-type center in the undoped LuAG is shown to be at ca. 3.15 eV [40], which does not match the observed defect emission. Based on the analogy with LuAG:Ce, the most probable candidate appeared to be an oxygen vacancy. The most intense PLE band related to the oxygen vacancies in LuAG:Ce was reported to be at ca. 3.32 eV [42, 67], and the emission bands were located at ca. 2.99 eV and 2.61 eV [42]. The first two bands (at 3.32 eV and 2.99 eV) are fairly close to the positions observed in the present investigation (3.30 eV and 2.95 eV, respectively) and the 2.61 eV band might partially be suppressed by reabsorption from $4f \rightarrow 4f$ excitation bands and, as a result, appeared only as a tail of the main emission peak at 2.95 eV. Based on these results, emission at 2.95 eV together with the excitation band at 3.30 eV was related to the presence of oxygen vacancies.

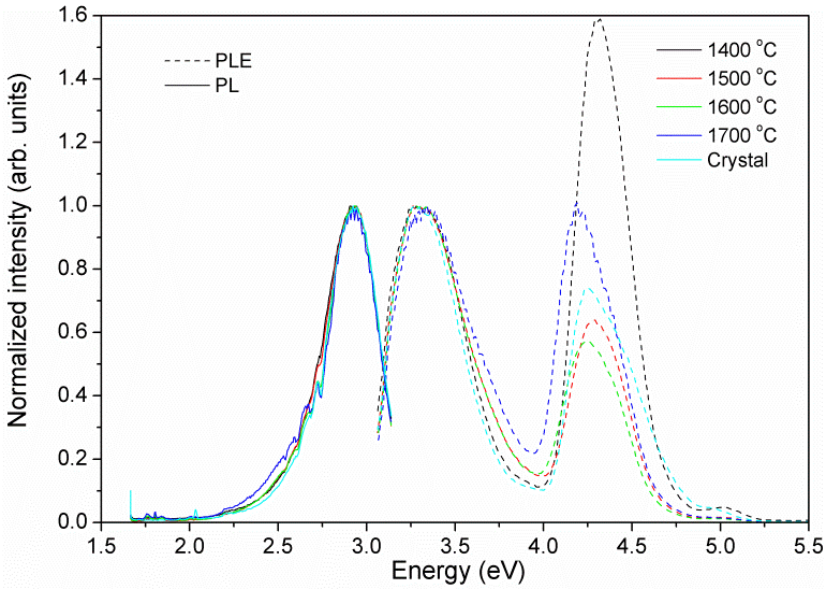

Figure 3.35. Normalized emission (PL; solid line) and excitation (PLE; dashed line) spectra of defects in LuAG:Pr polycrystalline ceramics and single crystal. PLE spectra were monitored at 2.95 eV, and PL spectra were excited at 3.30 eV.

Further, the effect of the sintering on the defects in LuAG:Pr is investigated by means of thermoluminescence. Figure 3.36 compares normalized glow curves of the polycrystalline ceramics and the single crystal. The glow curves from the polycrystalline samples are dominated by a band centered at 225 °C. It can be seen that FWHM of this glow peak is ca. 46.6 °C, and the expected range of FWHM for the peak at this temperature is 45.5-60.9 °C, which indicates that the peak is composed of a single band. The glow curve of the single crystal presents a dominant peak at 245 °C, a shoulder at 165 °C, and a shoulder at 285 °C, which seems to be absent in the case of the polycrystalline ceramics, as well as a band at 93 °C, which is similar to the peak of the polycrystalline ceramics. Additional bands can be seen above about 330 °C but due to limitations of the thermal range of the TL reader, it was not possible to execute a reliable analysis.

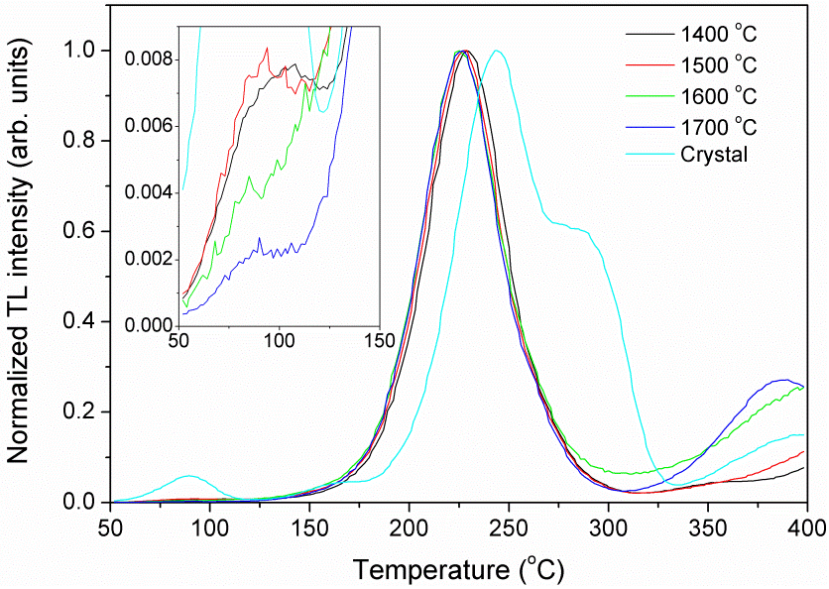

Figure 3.36. Normalized TL glow curves of the single crystal and the polycrystalline ceramics sintered at different temperatures. The inset highlights peak in the region of 50–150 °C.

Since the polycrystalline samples are opaque and, therefore, the light is coming only from the surface of the material, the TL glow curves were normalized by the surface area of the polycrystalline ceramics to allow for comparison. While TL results cannot specifically identify the nature of the traps involved, the change of the peak intensity can correspond to the change of the concentration of the traps. In Figure 3.37, typical glow curves from polycrystalline LuAG:Pr sintered at different temperatures (Figure 3.37A) are shown together with the average glow curve area value for each temperature (Figure 3.37B). Essentially, no changes are observed in the shape of the glow curves, which suggests that the higher sintering temperatures do not lead to the creation of new types of traps. Overall, there is a strong decrease in intensity trending toward saturation for sintering temperatures above 1400 °C. Thus, the use of high sintering temperatures is beneficial for LuAG:Pr polycrystalline scintillators by reducing the total concentration of traps.

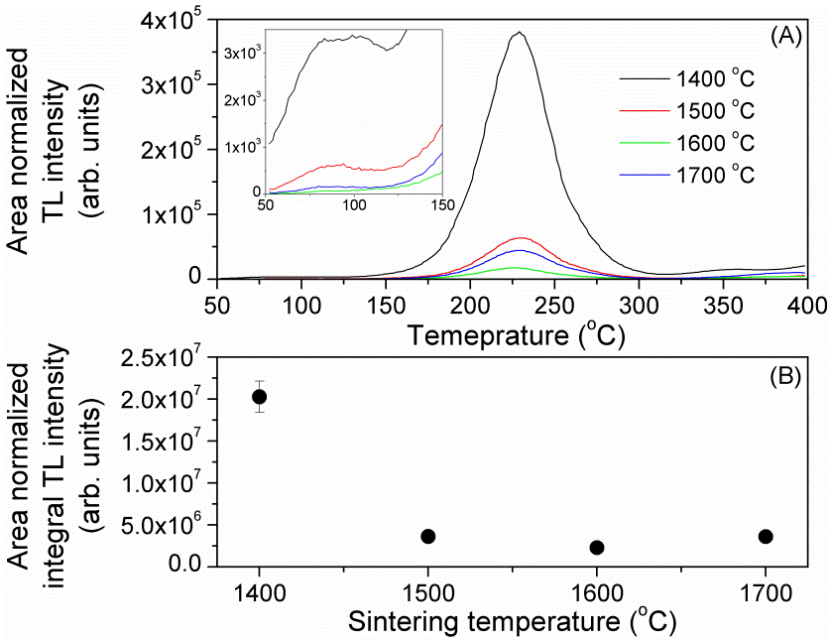

Figure 3.37. (A) Surface area-normalized TL glow curves of the polycrystalline LuAG:Pr sintered at different temperatures. The inset highlights the peak in the region of 50–150 °C. (B) Surface area-normalized integral TL intensity as a function of sintering temperature.

3.4. Microstructure and luminescence of $(Gd,Lu)_3(Ga,Al)_5O_{12}$:Ce (GLuGAG:Ce) polycrystalline ceramic scintillators with various Gd/Lu ratios

In addition to simple garnets, multicomponent garnets were investigated, namely, Ce-doped $(Gd_x,Lu_{3-x})(Ga,Al)_5O_{12}$ (GLuGAG:Ce) with various Gd/Lu ratios.

SEM micrographs of the polycrystalline samples are displayed in Figure 3.38. Features such as grains, grain boundaries, and pores can be easily seen. EDX results confirm the progressive incorporation of gadolinium as the nominal Gd/Lu ratio is increased, as shown in Figure 3.39a. A minor amount of calcium (ca. 0.25 at%) was also detected in “sintered only” samples.

The relationship between the microstructure of GLuGAG:Ce and the Gd/Lu ratio is emphasized through the evaluation of the change in the average grain size. As shown in Figure 3.39b, the increase of Gd/Lu ratio results in the linear increase of average grain size from 1.28 μm (x = 0) to 3.67 μm (x = 0.9) for the “sintered only” samples, and up to 8.73 μm (x = 3.0) for the HIPed samples.

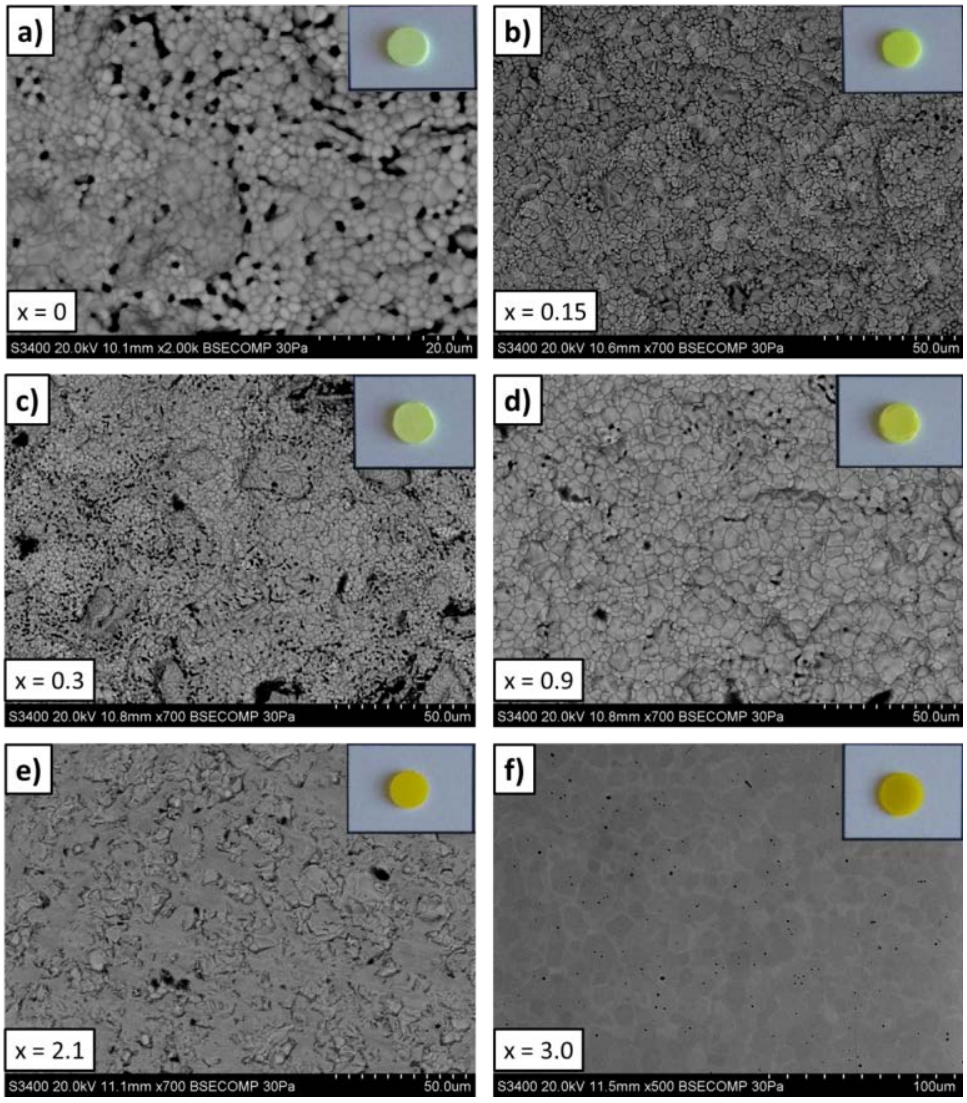

Figure 3.38. SEM micrographs of GLuGAG:Ce polycrystalline ceramics taken with different magnification.

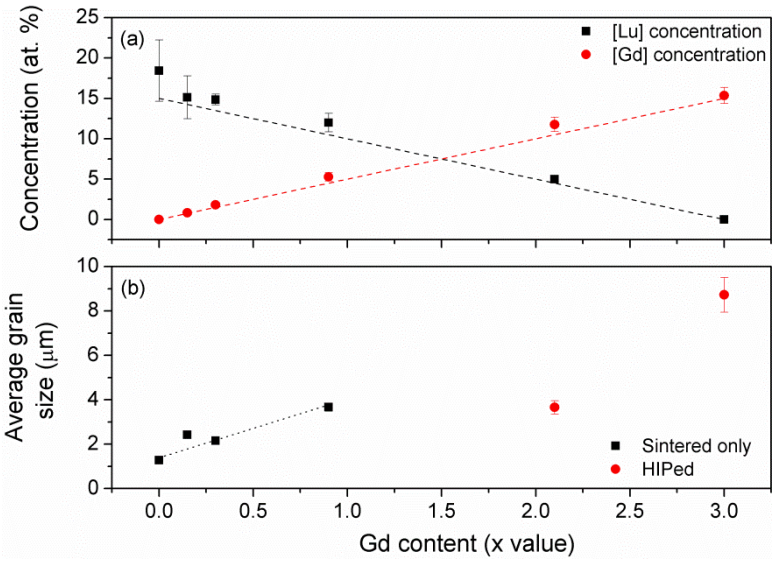

Figure 3.39. (a) EDX evaluation of Gd and Lu content in GLuGAG:Ce polycrystalline ceramics. Dashed lines show stoichiometric amount of Gd and Lu for a given nominal Gd content. (b) Evolution of the average grain size of the samples as a function of Gd content. Dotted line provided for clarity.

Figure 3.40a shows the single cubic garnet structure of all GLuGAG:Ce polycrystalline ceramics together with the standard ICDD data of the $Lu_3Al_5O_{12}$ (LuAG; card #01-073-1368) and $Gd_3Al_5O_{12}$ (GAG; card #01-073-1371). Additionally, XRD data show a shift of the diffraction peaks towards lower values of the 2θ angle with increasing Gd/Lu ratio (Figures 3.40b and 3.41a). This is a sign of a continuous expansion of the lattice due to the accommodation of Gd^{3+}, which has a larger ionic radius (1.053 Å for the coordination number (CN) of VIII) relative to that of Lu^{3+} (0.977 Å; CN = VIII) [68]. Calculations of the lattice constant as a function of Gd content confirms the expansion (Figure 3.41b).

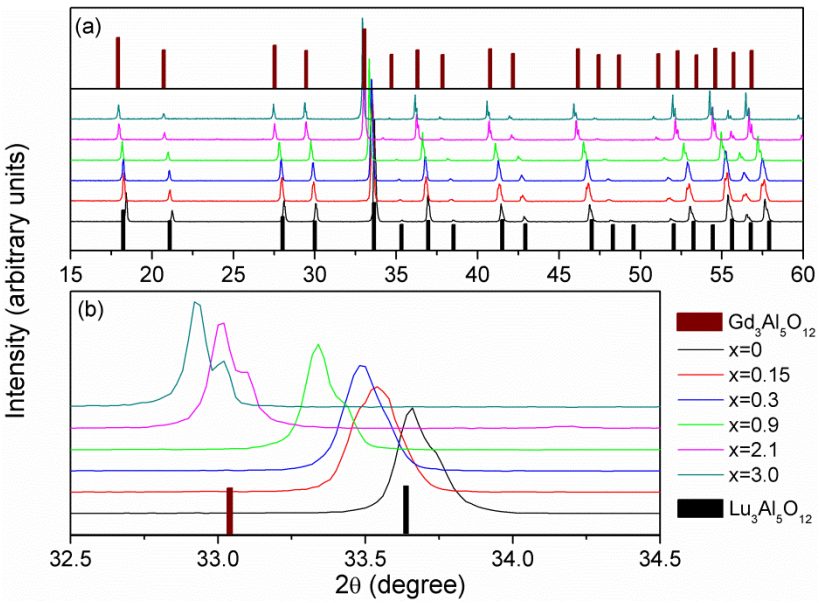

Figure 3.40. (a) XRD results of GLuGAG:Ce polycrystalline ceramics together with ICDD #01-073-1368 (black bar plot for $Lu_3Al_5O_{12}$) and #01-073-1371 (brown bar plot for $Gd_3Al_5O_{12}$); (b) Diffraction peak shift of GLuGAG:Ce at different Gd/Lu ratios.

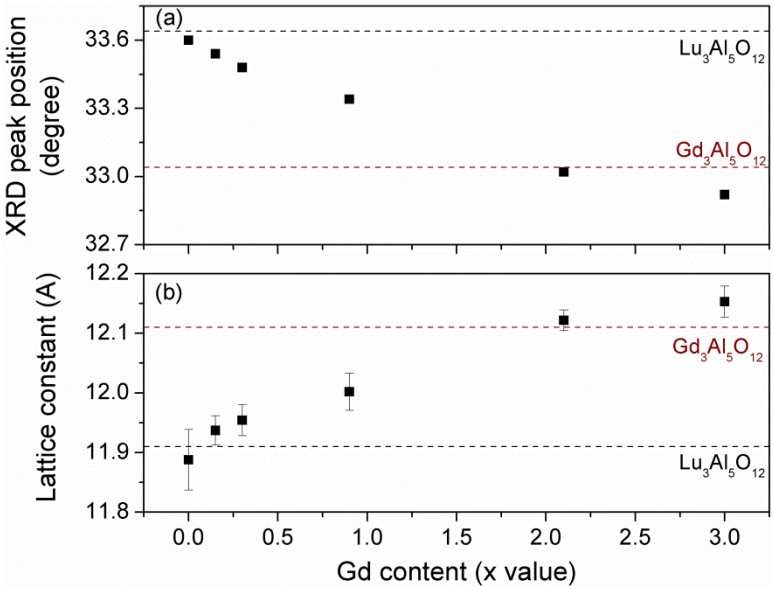

Figure 3.41. (a) The peak position shift of the most intense diffraction peak and (b) change of the lattice constant of GLuGAG:Ce at different Gd/Lu ratios. Dotted lines show the standard ICDD data values for LuAG and GAG.

Figure 3.42 shows the ATR FTIR spectra of the mixed garnet samples at ambient temperature. GLuGAG garnet unit cell consists of Al and Ga cations centered in eight octahedral sites and twelve tetrahedral sites and the rare-earth (RE) cations (Lu or Gd) occupying twelve dodecahedral sites [2, 4]. It can be seen from Figure 3.42 that the vibrational modes of LuAG:Ce ceramic (dotted line; shown for comparison) are more separated and better resolved than that of the GLuGAG:Ce polycrystalline ceramics. This is so because, in the case of $(Gd,Lu)_3(Al,Ga)_5O_{12}$ compounds, the structural distortion is induced in the polyhedra (dodecahedra, octahedra, and tetrahedra) by the substitution of Lu with Gd ions and Al with Ga ions. However, based on the analogy with YAG and LuAG [2, 4, 6], the vibrational modes can be assigned as follows: an overlap of a translation mode of octahedral cations and a symmetric bend of the tetrahedra between 400-450 cm^{-1}, the asymmetric bends of the tetrahedra between 450-560 cm^{-1}, and the asymmetric stretching modes of the tetrahedra between 560-900 cm^{-1}.

Additionally, it can be seen from Figure 3.42 that the substitution of Lu with Gd ions shifts the peak positions of the IR modes towards lower frequencies (redshift). This behavior is in agreement with the results of the recent investigation of vibrational properties of $(Gd,Y)_3Ga_5O_{12}$ compounds [69]. As it was discussed in the previous sections, the vibrational modes observed in Figure 3.42 are mainly related to the motion of the Al and Ga tetrahedral; however, the dodecahedra shares edges with both tetrahedral and octahedral. Consequently, substitution of Lu with Gd ions results in the expansion of the dodecahera and is accompanied by distortion of the tetrahedra. In such a manner, variation of the Gd/Lu ratio affects the position of the vibrational modes and results in frequency dependence on the unit cell volume calculated using the lattice parameter obtained earlier, as shown in Figure 3.43. All vibrational modes exhibit linear redshift

as a function of the increasing cell volume with the more pronounced shift for the modes at higher frequencies (note the slope of the linear fits in Figure 3.43).

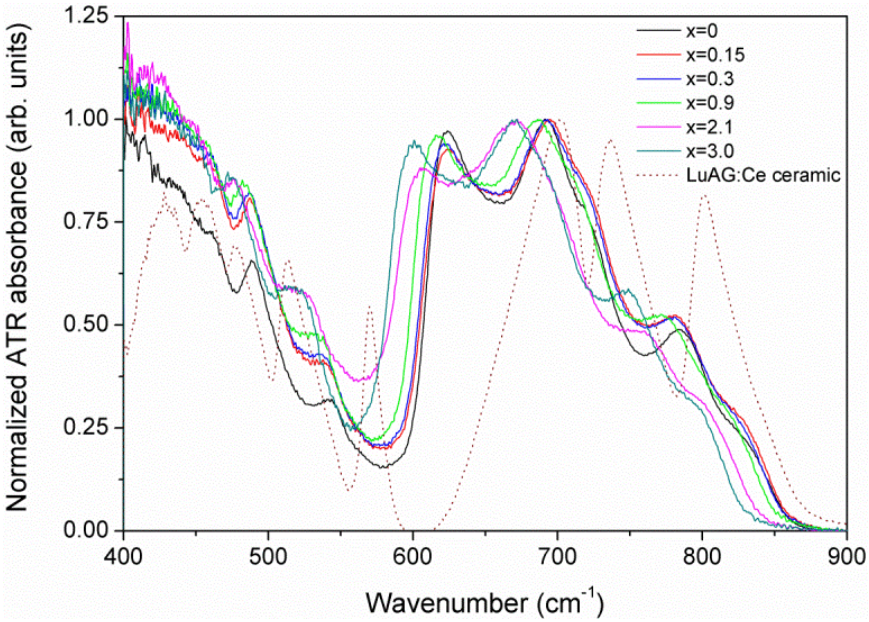

Figure 3.42. Absorption ATR FTIR spectra of GLuGAG:Ce polycrystalline ceramics normalized to the peak between 650-700 cm^{-1}. Spectrum of LuAG:Ce ceramic investigated in the present work is shown for comparison.

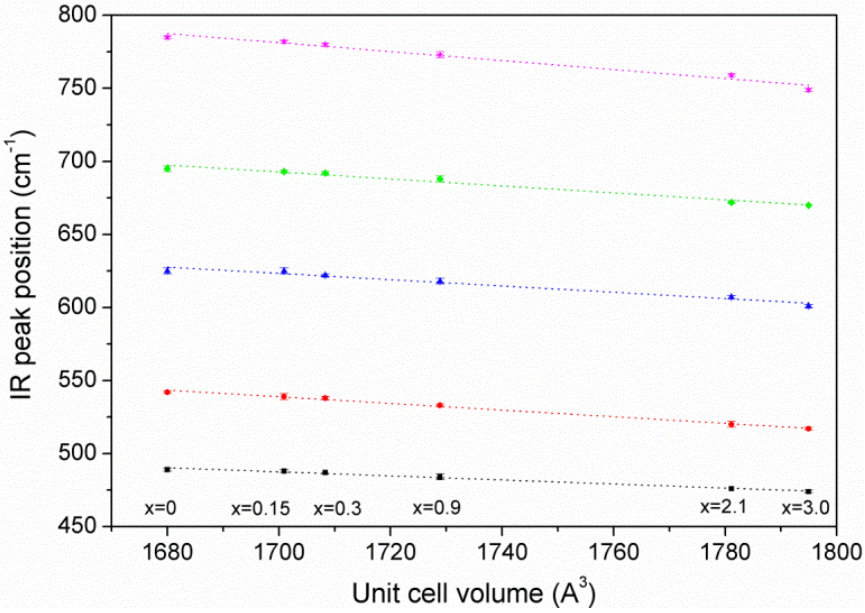

Figure 3.43. Dependence of the peak position of the resolved IR modes on the unit cell volume of GLuGAG:Ce polycrystalline ceramics. Dotted lines show linear fit of the experimental data.

The results of optical transmission measurements of the polycrystalline ceramics are presented in Figure 3.44. The increase of the level of transparency from "sintered only" samples to sintered and HIPed samples indicates densification of the samples. Absorption bands corresponding to Ce^{3+} ions can be resolved between 400-500 nm (2.48-3.10 eV) and ca. 350 nm (3.54 eV) corresponding to the $4f \rightarrow 5d_1$ and $5d_2$ transitions, respectively. An additional Ce^{3+} absorption band related to a transition to the highest 5*d* level is located around 200-230 nm (5.4-6.2 eV) [70, 71]. Another absorption band between 230-330 nm (3.76-5.39 eV) was commonly observed in the investigations of Ce-doped mixed garnets co-doped with Ca and was ascribed to the charge transfer (CT) transition from O^{2-} levels at the top of the valence band towards Ce^{4+} [72-77]. The presence of Ca^{2+} ions results in the increase of the stable Ce^{4+} fraction due to charge compensation. In the present work, materials are not intentionally co-doped with Ca but, as it is discussed earlier, EDX analysis reveals presence of some amount of Ca in the samples. Thus, it

is reasonable to assign the absorption between 230-330 nm (3.76-5.39 eV) to the CT transition between Ce^{4+} and O^{2-}.

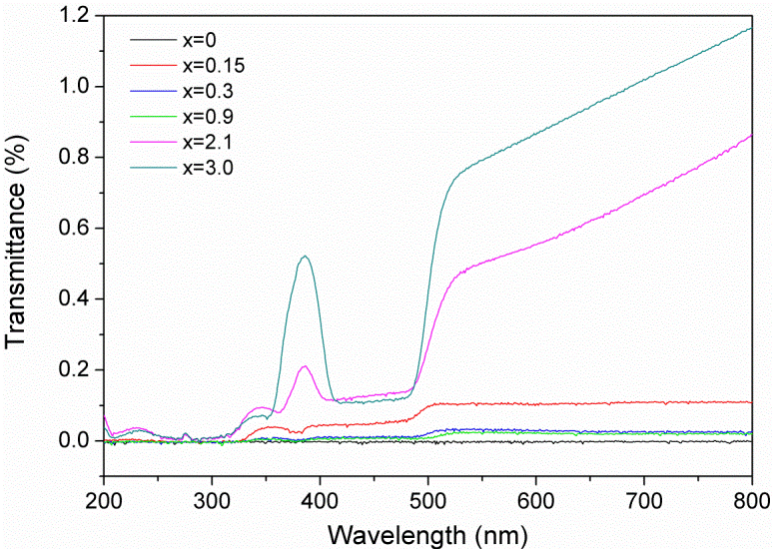

Figure 3.44. Transmission of GLuGAG:Ce polycrystalline ceramics at different Gd/Lu ratios.

PLE spectra of GLuGAG:Ce polycrystalline ceramics at different Gd/Lu ratios are presented in Figure 3.45a. Broad excitation bands in the 2.35-3.25 eV (380-530 nm) and 3.25-3.85 eV (320-380 nm) ranges are related to the $4f \rightarrow 5d_1$ and $5d_2$ transitions of Ce^{3+}, respectively [71, 78, 79]. The weak peaks at ca. 3.96 eV (313 nm), 4.03 eV (308 nm), and 4.10 eV (302 nm) are caused by the $4f \rightarrow 4f$ transitions of Gd^{3+} cations ($^8S_{7/2} \rightarrow {}^6P_{7/2}$, $^6P_{5/2}$, $^6P_{3/2}$ transitions, respectively) [80] which is an indication of the energy transfer between Ce^{3+} and Gd^{3+} ions. The fine structure between 2.5-2.9 eV is due to the fine structure of the emission spectrum of the xenon lamp [9].

It can be seen in Figure 3.45 that the increase of the Gd content causes the shift of the $4f \rightarrow 5d_2$ transition of Ce^{3+} towards higher energies. Recent theoretical calculations based on the chemical shift model [81] show that when Gd/Lu ratio is increased, the crystal field strength is

also increased due to the larger Gd^{3+} cations, as shown in Figure 3.46. As a result, crystal field splitting of the 5*d* level of Ce^{3+} becomes larger. Consequently, the energy distance between the $5d_1$ and $5d_2$ levels increases bringing $5d_1$ level closer and moving $5d_2$ level farther from the 4*f* energy level of Ce^{3+}, as schematically shown in Figure 3.46. In turn, the 4*f* energy level is essentially unaffected by the variations in the crystal field due to the shielding from the electrons of the outer orbitals of cerium. In such a manner, since the energy difference between the 4*f* and $5d_2$ levels increases with Gd content, the $4f \rightarrow 5d_2$ excitation band shifts towards higher energies as shown in Figure 3.45b. The observed behavior is in a good agreement with that reported for the single crystalline film (SCF) [70] and powder [79] of similar compositions.

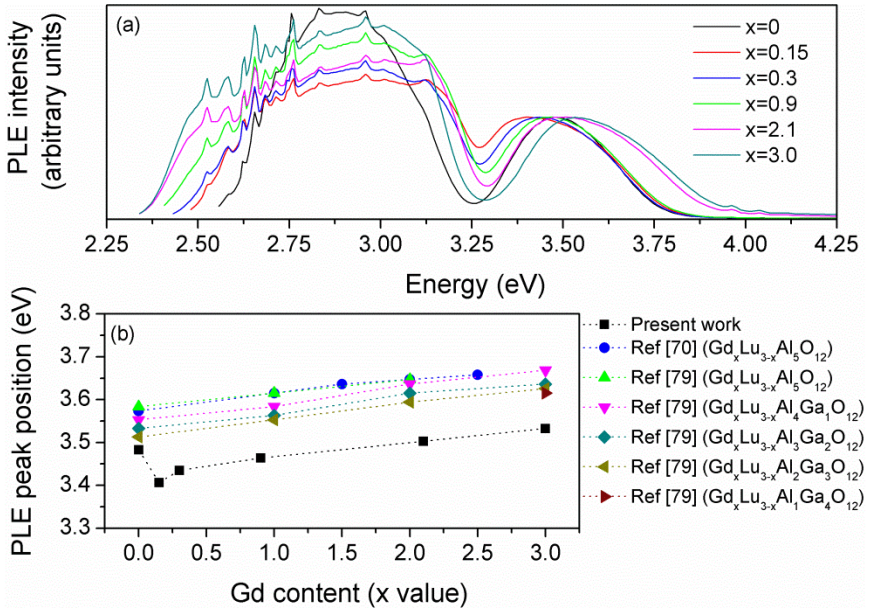

Figure 3.45. (a) Ce^{3+} related PLE of GLuGAG:Ce polycrystalline ceramics with different Gd/Lu ratios; (b) Dependence of the peak position of the Ce^{3+} $4f \rightarrow 5d_2$ excitation on Gd content in comparison to the SCF [70] and powder [79] of similar compositions.

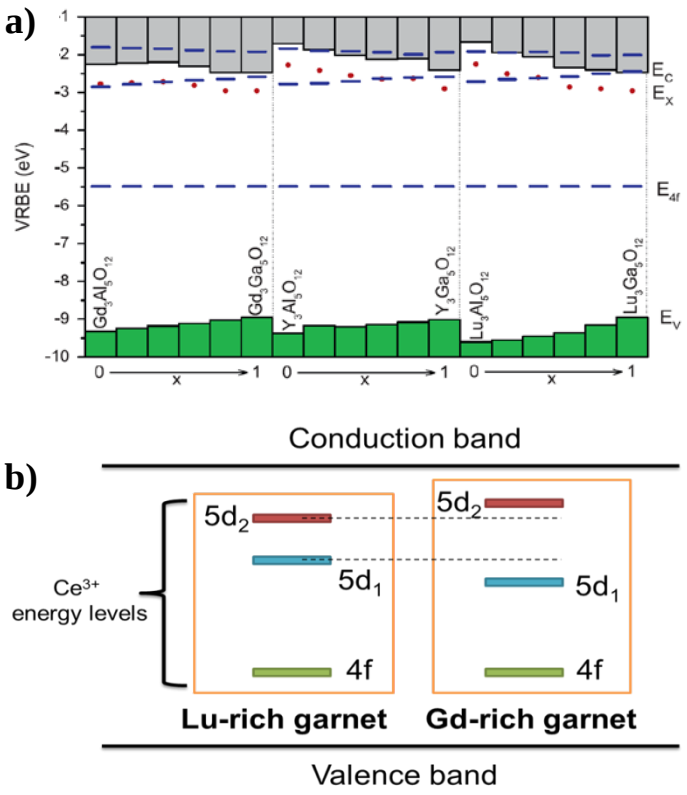

Figure 3.46. (a) The binding energy (VRBE) for electrons in the 4*f* ground state and first two excited 5*d* states of Ce^{3+} in the $RE_3(Al_{1-x}Ga_x)_5O_{12}$ garnet compounds [81] (b) Schematic representation of the increase of Gd/Lu ratio on Ce^{3+} levels in garnets.

PL spectra of GLuGAG:Ce polycrystalline ceramics at different Gd/Lu ratios are shown in Figure 3.47a. The observed broad emission is related to the $5d_1 \rightarrow 4f$ transition of Ce^{3+} which is an overlap between $5d_1 \rightarrow 4f$ ($^2F_{5/2}$) and $4f$ ($^2F_{7/2}$) transitions [9, 10] due to spin-orbit coupling splitting in Ce^{3+} ions. Similar to the behavior of the excitation bands, the shift of the emission peak position towards lower energies as a function of Gd content (Figure 3.47b) is related to the increase in the crystal field splitting that causes the $5d_1$ level to move closer to the 4*f* energy level (cf. Figure 3.46). This behavior is in agreement with that reported for SCFs [70] and single crystals [78] of similar compositions. The nature of the shoulder centered around 1.85-1.9 eV is discussed later.

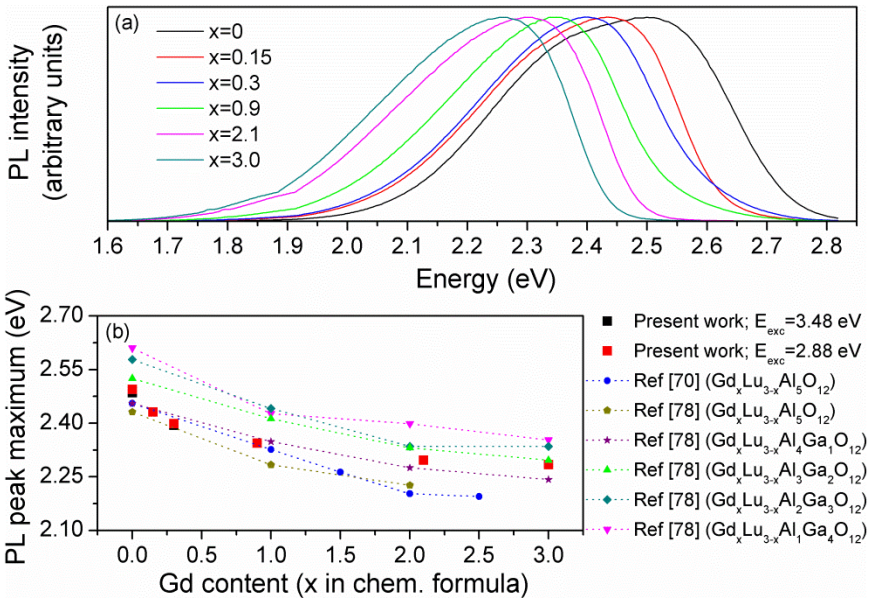

Figure 3.47. (a) Ce^{3+} related PL of GLuGAG:Ce polycrystalline ceramics with different Gd/Lu ratios; (b) Dependence of the peak position of the Ce^{3+} $5d_1 \rightarrow 4f$ emission on Gd content in comparison to the SCF [70] and single crystal [78] of similar compositions.

Besides Ce^{3+} related transitions, Gd^{3+} transitions are also observed, as already noted in Figure 3.45a. More detailed PLE and PL of Gd^{3+} in GLuGAG:Ce polycrystalline ceramics are shown in Figure 3.48a. Two emission lines at 3.96 eV (313 nm) and 4.03 eV (308 nm) are observed under 4.53 eV (274 nm) excitation and ascribed to the $^6P_{7/2}$ and $^6P_{5/2} \rightarrow {}^8S_{7/2}$ transitions in the Gd^{3+} ion, respectively [80, 82]. PLE spectra monitored at 3.96 eV (313 nm) revealed three excitation lines at 4.43 eV (280 nm), 4.48 eV (277 nm), and 4.53 eV (274 nm) related to the $^8S_{7/2} \rightarrow {}^6I_J$ transitions of Gd^{3+} [72, 82]. Positions of the discussed emission and excitation bands are independent of Gd content as expected since all of the aforementioned lines are part of the $4f \rightarrow 4f$ transitions of Gd^{3+} and, thus, virtually unaffected by the changes in the surrounding crystal field of the host material due to shielding provided by the outer electrons of the ion. On the other hand, variation in the intensity of Gd^{3+} lines is observed as a function of Gd/Lu ratio, and the

dependence is evaluated in Figure 3.48b through PL intensity integration over the 3.75-4.25 eV range. PL integrated intensity curve exhibits a maximum at x = 0.3, and the overall phenomenon is typically called “concentration quenching” [83]. First, the increase of Gd concentration leads to an increase of the emission intensity since more Gd^{3+} ions can be excited and emit light. Simultaneously, the increase of the concentration results in the decrease of the average distance between the ions. As a result, when the amount of Gd^{3+} becomes above the critical value (x ≈ 0.3, in the present case), energy migration between Gd^{3+} ions starts to dominate over radiative de-excitation. In such a manner, the excitation energy is transferred over a large number of Gd^{3+} ions and eventually gets transferred to a killer center and is non-radiatively relaxed to the ground state.

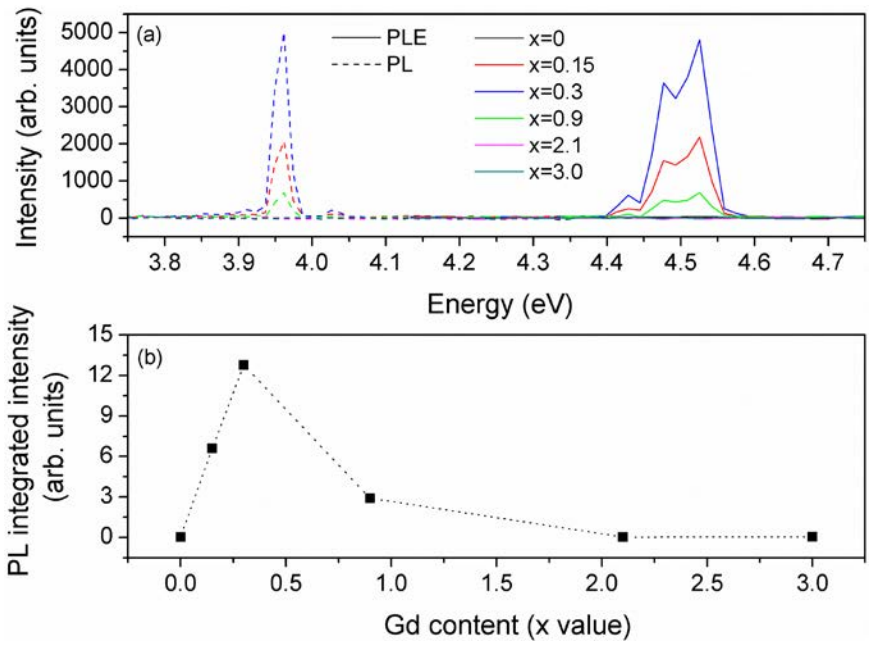

Figure 3.48. (a) Gd^{3+} related PLE (solid lines; E_{em} = 3.96 eV) and PL (dashed lines; E_{ex} = 4.53 eV) of GLuGAG:Ce polycrystalline ceramics with different Gd/Lu ratios; (b) Concentration quenching of Gd^{3+} emission in GLuGAG:Ce polycrystalline ceramic.

In order to explore the presence of potential defects in GLuGAG:Ce polycrystalline ceramics, further investigation of PL and PLE was performed. Additional luminescence from GLuGAG:Ce with x = 0-0.9 is revealed in the 3-5 eV range (Figure 3.49). A luminescence center with a broad emission at 3.26 eV (380 nm) and an excitation around 3.65 eV (340 nm), as shown in Figure 3.49a, is assigned to the F^+ centers according to [72, 73, 75]. An emission and excitation observed at 3.02 eV (410 nm) and 3.32 eV (373 nm), respectively, as shown in Figure 3.49b, are reported in the investigation of LuAG:Ce to be related to the presence of oxygen vacancies (V_O) [42, 67]. The observed defect-related bands cannot be resolved in the case of GLuGAG:Ce with x = 2.1 and 3.0 due to strong overlap with the emission/excitation bands of another luminescence center to be discussed later.

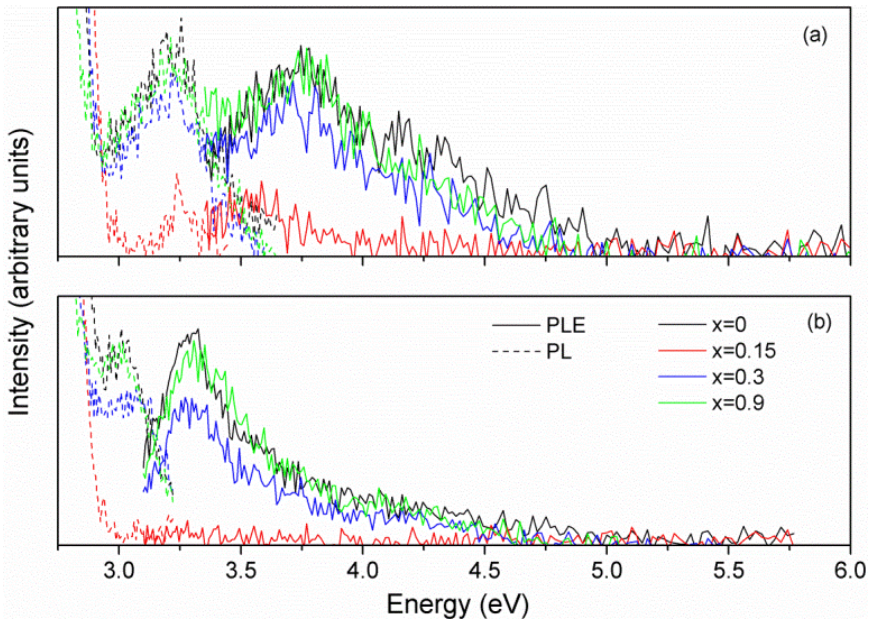

Figure 3.49. (a) F^+ related PLE (solid lines; E_{em} = 3.26 eV) and PL (dashed lines; E_{ex} = 3.72 eV) and (b) V_O related PLE (solid lines; E_{em} = 3.02 eV) and PL (dashed lines; E_{ex} = 3.32 eV) of GLuGAG:Ce polycrystalline ceramics with different Gd/Lu ratios.

Additionally to the Ce^{3+} and Gd^{3+} ions, that are intentionally incorporated in the investigated materials, transitions related to the Eu^{3+} and Nd^{3+} are also detected by means of photoluminescence (Figure 3.50). As it is noted in Figure 3.47a, Ce^{3+} emission band is accompanied by a shoulder centered ca. 1.85-1.9 eV. Investigation of the PLE and PL spectra in the 1.5-2.25 eV region (Figure 3.50a) revealed excitation and emission lines assigned to the $4f \rightarrow 4f$ transitions of Eu^{3+} [84, 85]. The emission within 1.70-1.85 eV (670-725 nm) is due to multiple $^5D_0 \rightarrow {}^7F_4$ lines, the band at 1.95 eV (636 nm) corresponds to the $^5D_0 \rightarrow {}^7F_3$ transition, and emission at 2.03 eV (610 nm) is ascribed to $^5D_0 \rightarrow {}^7F_2$. In the case of the PLE spectra, excitation lines at 2.11 eV (588 nm) and 2.14 eV (579 nm) are due to $^7F_1$ and $^7F_0 \rightarrow {}^5D_0$ transitions of Eu^{3+}, respectively. In the case of Nd^{3+}, its characteristic $4f \rightarrow 4f$ transitions are observed in 2.75-5.0 eV (Figure 3.51b) and 1.35-2.25 eV (Figure 3.50c) ranges [86-88]. PL and PLE seen in Figure 3.50b are ascribed as follows: emission lines at 3.24 eV (383 nm) are an overlap between $^2P_{3/2} \rightarrow {}^4I_{9/2}$ and $^4D_{3/2} \rightarrow {}^4I_{11/2}$ transitions, emission at 2.96 eV (419 nm) is $^2P_{3/2} \rightarrow {}^4I_{11/2}$ transition, and excitation at 4.68 eV (265 nm) is $^4I_{9/2} \rightarrow {}^2F_{5/2}$ transition overlapped with $^8S_{7/2} \rightarrow {}^6I_J$ lines of Gd^{3+} [86]. $^8S_{7/2} \rightarrow {}^6P_J$ excitation lines of Gd^{3+} can also be seen in 3.90-4.15 eV range. Investigation of the PL and PLE close to near-IR range confirmed the presence of Nd^{3+}, as shown in Figure 3.50c. Emission in 1.35-1.55 eV (800-920 nm) range is related to $^4F_{3/2,\ 5/2} \rightarrow {}^4I_{9/2}$ transitions [85, 88], and presence of excitation line at 2.11 eV ($^7F_{1,0} \rightarrow {}^5D_0$ transitions of Eu^{3+}) indicates the energy transfer between Eu^{3+} and Nd^{3+} ions. Note that the PL and PLE spectra in Figures 3.50b and 3.50c are only shown for the sample with x = 2.1 for clarity and the same discussion applies to the other compositions investigated in this work.

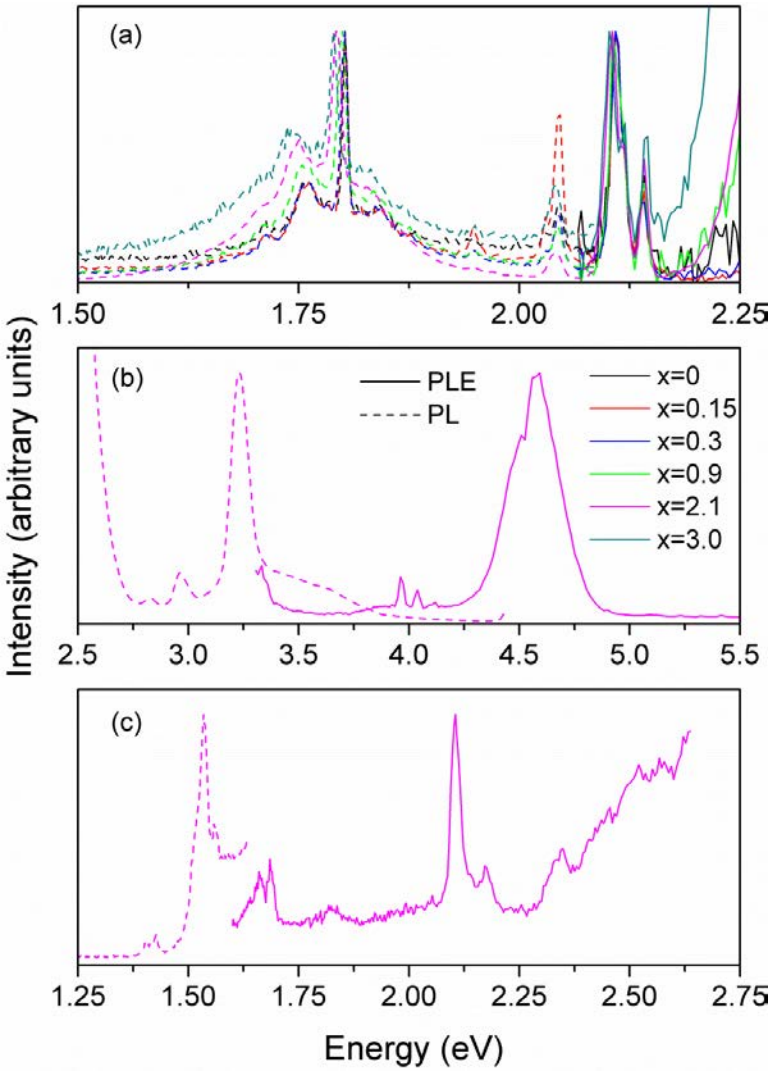

Figure 3.50. (a) Eu^{3+} related PLE (solid lines; E_{em} = 1.80 eV) and PL (dashed lines; E_{ex} = 2.11 eV) and (b) and (c) Nd^{3+} related PLE (solid lines; (b) E_{em} = 3.24 eV; (c) E_{em} = 1.53 eV) and PL (dashed lines; (b) E_{ex} = 4.68 eV; (c) E_{ex} = 1.68 eV) of GLuGAG:Ce polycrystalline ceramics. In (b) and (c) cases, only spectra for the sample with x = 2.1 are shown for clarity.

It is important to note that the observed shoulder accompanying Ce^{3+} emission in Figure 3.47a, that led to the discovery of the presence of Nd^{3+} and Eu^{3+} in these GLuGAG:Ce polycrystalline ceramics, can often be seen in the PL spectra of Ce-doped garnets [39, 71, 89-

92]. The existence of the additional luminescent rare-earth elements (such as Eu^{3+} and Nd^{3+}) can negatively affect the performance of the garnet materials as scintillators, especially, since the indication of the energy transfer from Ce^{3+} to Eu^{3+} (Figure 3.47a) is evident.

Lastly, scintillation performance of GLuGAG:Ce polycrystalline ceramics was quantified based on the measurements of the light yield. As an example of these measurements, the pulse height distributions of the investigated samples and a BGO single crystal irradiated with a ^{241}Am point source are shown in Figure 3.51, where photopeaks related to 13.9 keV and 59.5 keV γ-rays can be seen. Measurements using point sources with different γ-ray energies combined with the extraction of the photopeak positions from each measurement allowed evaluation of the light yield of the materials. Figure 3.52 presents the light yield and its linearity (also referred to as "proportionality") of the polycrystalline samples as a function of the γ-ray energy relative to a BGO single crystal. "Sintered only" samples, with the exception of the x = 0.15 material, revealed similar behavior, as seen in Figure 3.52a. Despite the "sintered only" samples being opaque, their light yield value varied around the value for the BGO single crystal, thus showing a good potential of these materials as scintillators. HIPed samples and the sample with x = 0.15, on the other hand, showed very linear behavior (Figure 3.52b) with the light yield value consistently higher than that of the BGO. The most promising results are obtained for the $(Gd_{2.1},Lu_{0.9})(Al,Ga)_5O_{12}$:Ce (x = 2.1) polycrystalline ceramic that showed the light yield to be ca. 2.45±0.2 times higher (average value over 14-835 keV range) than that of the BGO single crystal despite the fact that the HIPed samples are only translucent.

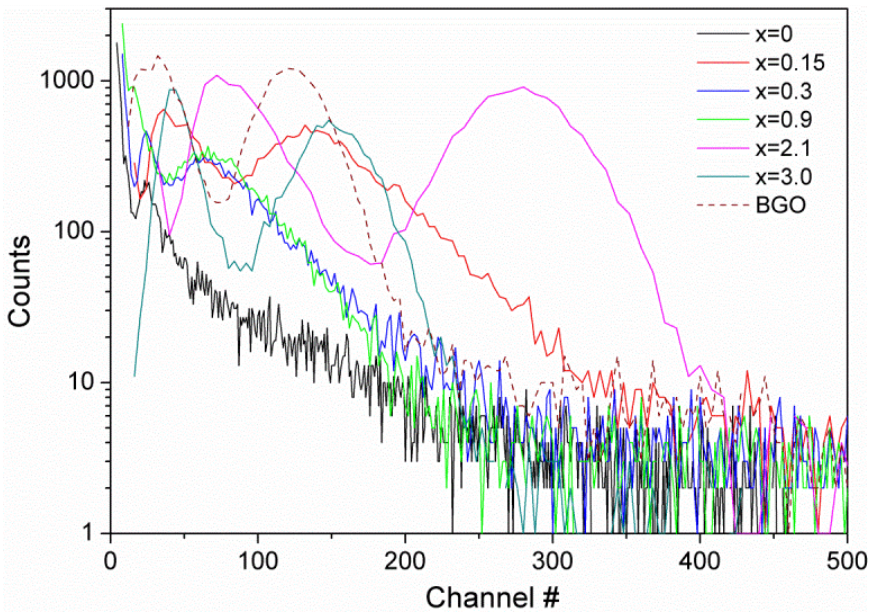

Figure 3.51. Pulse height distribution of GLuGAG:Ce polycrystalline ceramics with different Gd/Lu ratios and BGO single crystal excited with ^{241}Am (photopeaks are related to 13.9 keV and 59.5 keV).

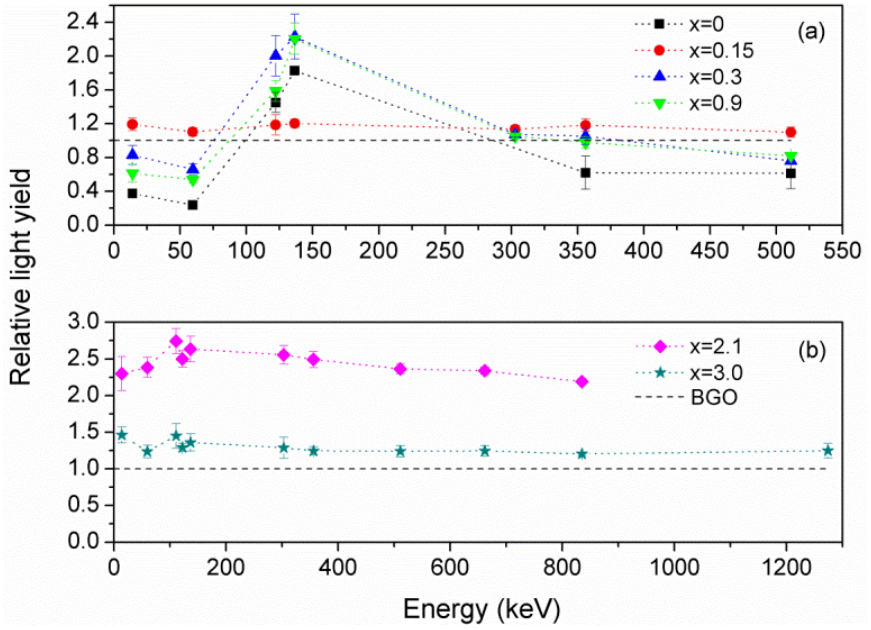

Figure 3.52. Light yield of GLuGAG:Ce polycrystalline ceramics relative to the light yield of BGO single crystal for each γ-ray energy used. (a) “Sintered only” samples, (b) HIPed samples.

3.5. Luminescence investigation of Ce incorporation in garnet-type $Li_7La_3Zr_2O_{12}$ **[93]**

Additional to the investigation of known luminescent garnet materials, luminescent properties of Ce-doped garnet-type $Li_7La_3Zr_2O_{12}$ (LLZO:Ce), as a potentially new material for scintillation applications, were examined in the present work.

Figure 3.53 shows XRD results of undoped and Ce-doped $Li_7(La_{1-x}Ce_x)_3Zr_2O_{12}$ with $0 \leq x \leq 0.05$ that reveals the structural evolution of LLZO upon Ce incorporation. Undoped LLZO has tetragonal structure (183684-ICSD; [94]) composed of $La(1)O_8$ and $La(2)O_8$ dodecahedra, ZrO_6 octahedra, and Li octahedra and tetrahedral [95]. Up to about x = 0.01, the host remains essentially tetragonal LLZO though minor distortions in the diffraction peaks can be observed. Further cerium incorporation lead to structural changes that culminate in a different structure for x = 0.05 that corresponds to a combination of cubic LLZO (261302-ICSD; [96]), and a secondary phase Ce_4O_7 (PDF#:65-7999). Li_2ZrO_3(PDF#:330843) is also observed as a secondary minor phase.

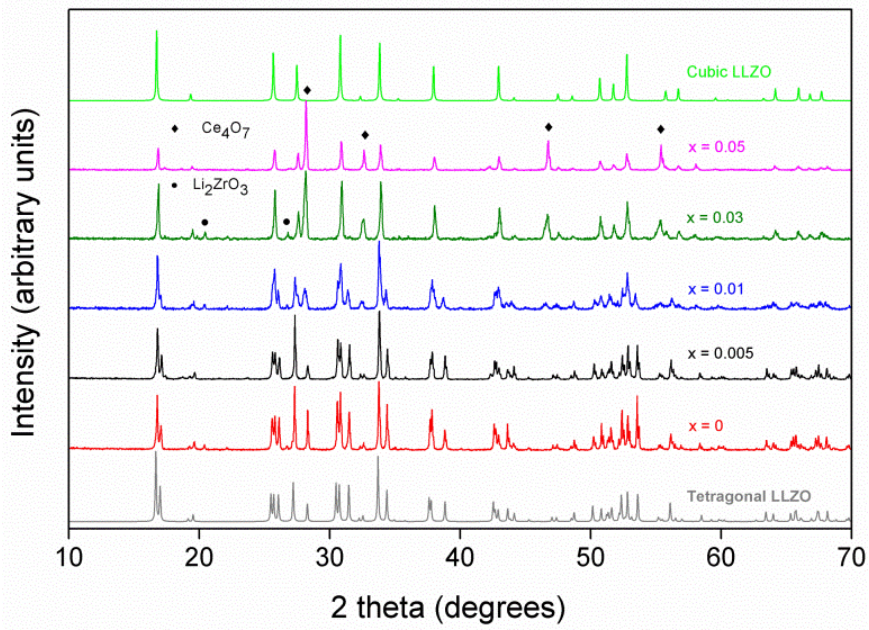

Figure 3.53. XRD results of $Li_7(La_{1-x}Ce_x)_3Zr_2O_{12}$ with x = 0, 0.005, 0.01, 0.03, and 0.05, together with calculated diffractograms of cubic and tetragonal LLZO based on 261302-ICSD [96] and 183684-ICSD [94], respectively. The position of the diffraction peaks from minor phases are indicated.

Figure 3.54 summarizes the RL results at room temperature. Undoped and Ce-doped LLZO present broad emission bands within the spectral range of about 2–3.5 eV. Incorporation of Ce changes the emission spectra, with the centroid shifting to lower energies compared to undoped LLZO. Spectra of LLZO with Ce content up to x = 0.03 are similar in shape and spectral range, while, for x = 0.05, a distinct spectrum shift to even lower energies is observed. Spectral analysis by means of Gaussian bands deconvolution (dotted lines) reveals the emission spectrum of undoped tetragonal LLZO to be composed of a single band centered at 2.84 eV. This band has been reported before and was attributed to the Zr-O charge transfer (CT) transition [97]. At room temperature, within the $0.005 \leq x \leq 0.03$ compositional range, the spectra are deconvoluted with

two Gaussian bands (dotted lines) centered at about 2.41 and 2.78 eV, and, for x = 0.05, an additional band centered at about 2.15 eV is necessary to achieve reliable spectral deconvolution.

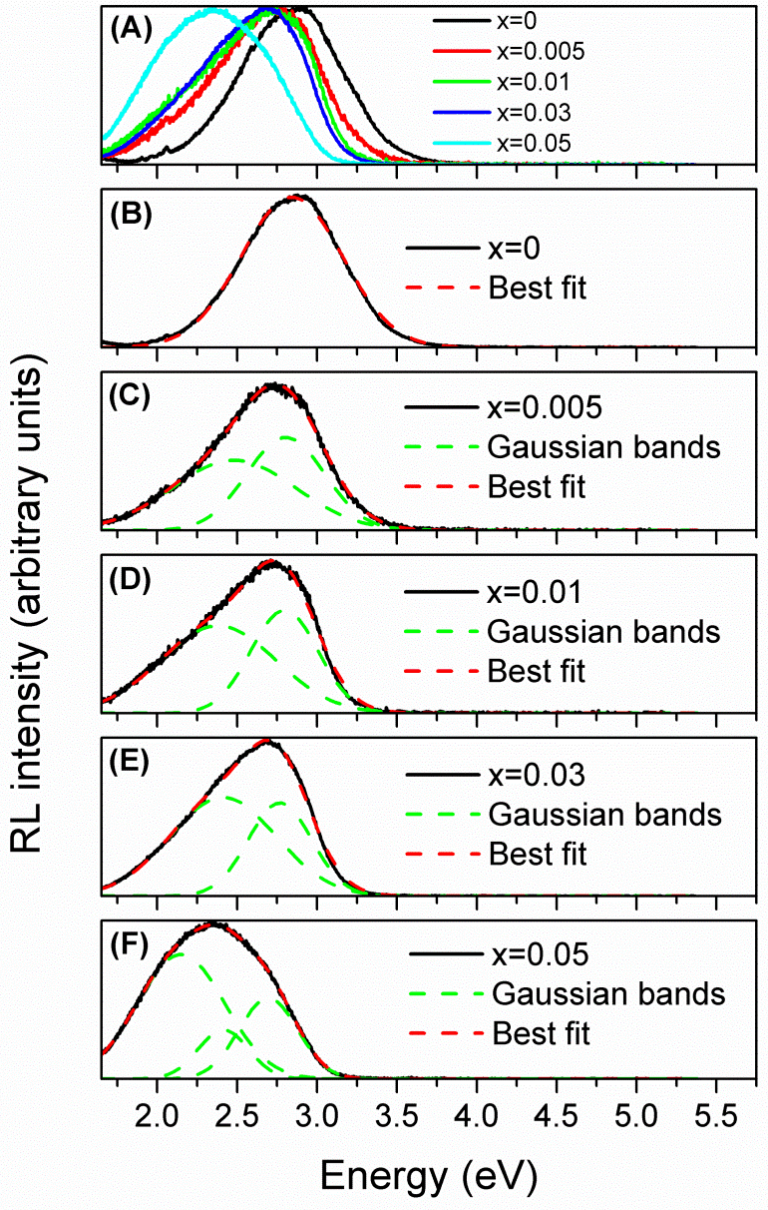

Figure 3.54. a) Normalized RL spectra of $Li_7(La_{1-x}Ce_x)_3Zr_2O_{12}$ with x = 0, 0.005, 0.01, 0.03, and 0.05 obtained at room temperature. Gaussian band deconvolution of RL spectra for b) x = 0, c) x = 0.005, d) x = 0.01, e) x = 0.03, and f) x = 0.05.

The behavior of the peak position of the individual Gaussian bands is presented in Figure 3.55a and shows that Ce incorporation into LLZO quenched the intrinsic Zr-O CT transition, and that Ce occupies two distinct crystallographic sites, as expected from its substitution for La. The difference in energy of 0.37 eV between the two emission bands in tetragonal LLZO:Ce is in very good agreement with the difference observed between the emission bands of Ce^{3+} in two distinct crystallographic sites in Gd_2SiO_5 [98], while being too high to be attributed to spin-orbit splitting typically on the order of 0.2-0.25 eV. Figure 3.55b presents the 2.41/2.78 integrated band intensity ratio. The behavior of the intensity ratio as a function of the Ce content suggests an increasing preference for Ce to be incorporated into the site responsible for the band located at 2.41 eV. Since the ionic radius of La^{3+} is slightly larger than that of Ce^{3+} [68], and since the La-O distances are overall longer in $La(1)O_8$ than in the $La(2)O_8$ sites (ca. 0.259 and ca. 0.254 nm, respectively [95]), easier incorporation of Ce^{3+} into $La(1)O_8$ sites is expected, suggesting the 2.41 eV band is associated with Ce^{3+} occupying these sites. The band at 2.15 eV is attributed to Ce emission in cubic LLZO.

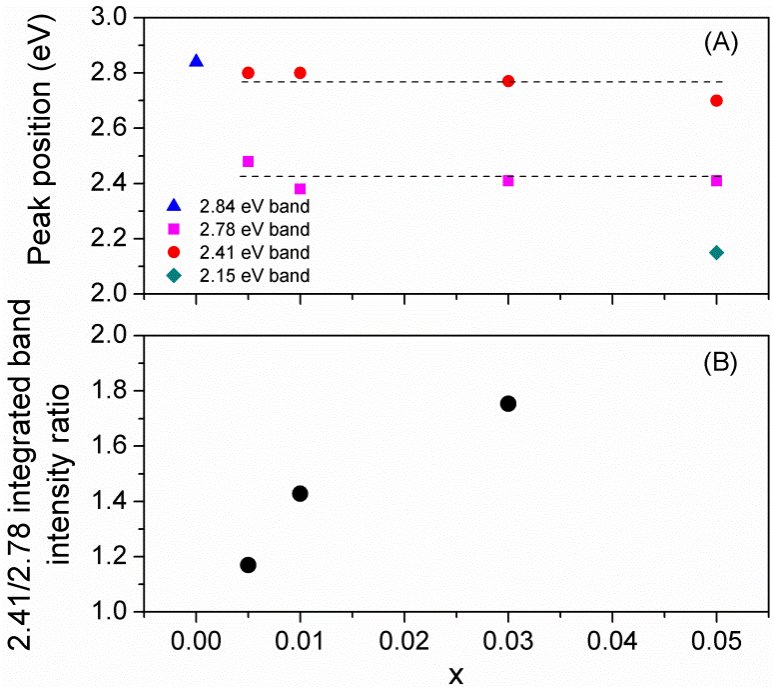

Figure 3.55. a) Peak position of Gaussian bands used in the deconvolution of RL spectra obtained at room temperature, and b) 2.41/2.78 integrated band intensity ratio as a function of the nominal Ce content.

The effects of temperature on RL are presented in Figure 3.56 for x = 0, 0.005, and 0.01 for selected temperatures between room temperature and 250 °C. Already by 50–60 °C, thermal quenching reduces intensity by about half. At 250 °C the emission is negligible for undoped LLZO and weak for the Ce-doped materials, with higher Ce contents yielding higher thermal stability.

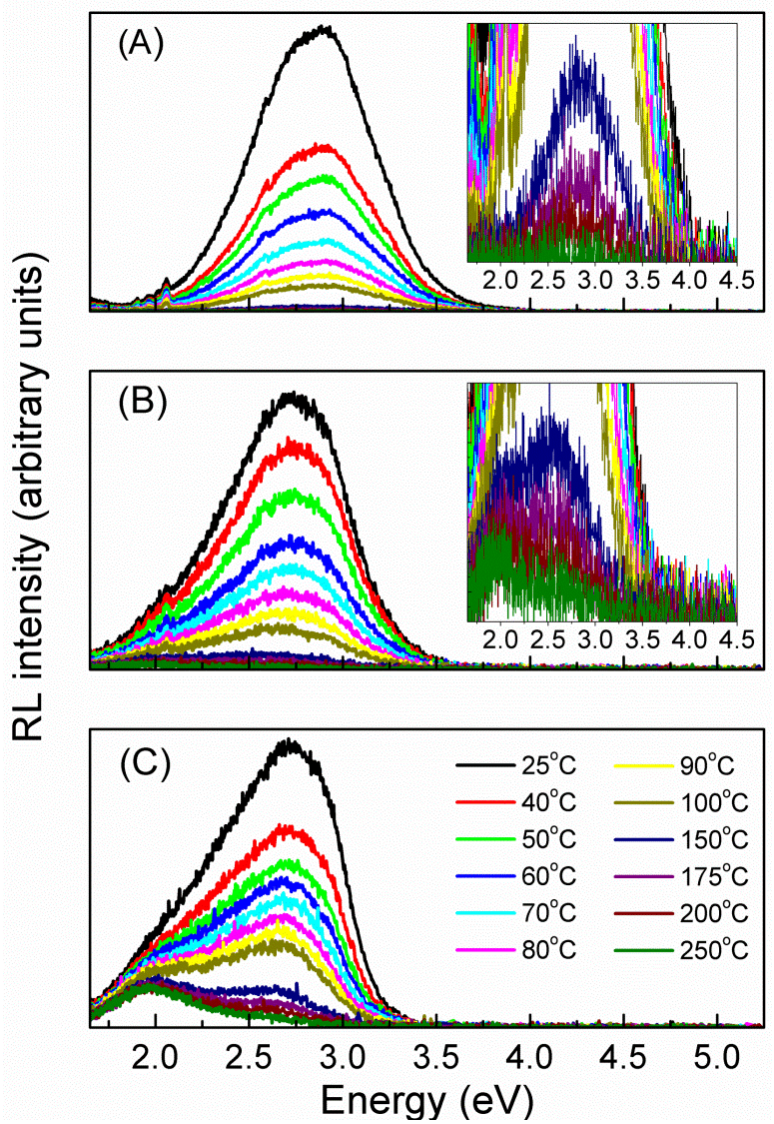

Figure 3.56. RL spectra obtained at different temperatures for a) x = 0, b) x = 0.005, and c) x = 0.01. The color indicates the temperature at which the spectrum was taken.

In Figure 3.57, the results of the spectral deconvolution are presented as a function of temperature. Similarly to the room temperature data, the emission from undoped LLZO is fitted with one Gaussian band, while for x = 0.005 and 0.01 two bands are used. Figure 3.57a shows the evolution of the peak position of the Gaussian bands as a function of the temperature. The band centered at 2.84 eV (at room temperature) observed only in undoped tetragonal LLZO

shows a small shift toward lower energies, from 2.84 to 2.82 eV. In the case of x = 0.005 and 0.01, both bands shift to lower energies, from 2.78 to 2.34 eV and from 2.41 to 1.95 eV (average values), respectively, over the entire temperature range, with the 2.41 eV band stabilizing at 1.95 eV at about 150 °C. Figure 3.57b shows the 2.41/2.78 integrated band intensity ratio for LLZO with x = 0.005 and 0.01 as a function of temperature. These results show that, while luminescence is dominated by the emission of the 2.41 eV band at room temperature/low temperatures, depending on the Ce concentration, the center responsible for this emission is more strongly thermally quenched than the center responsible for the 2.78 eV band. Different thermal stability of Ce occupying nonequivalent crystallographic sites was also observed in Gd_2SiO_5:Ce [98]. The distinct thermal behavior of each of the emission bands centered at 2.84, 2.78, and 2.41 eV demonstrate the different nature of the respective luminescence centers associated to these bands.

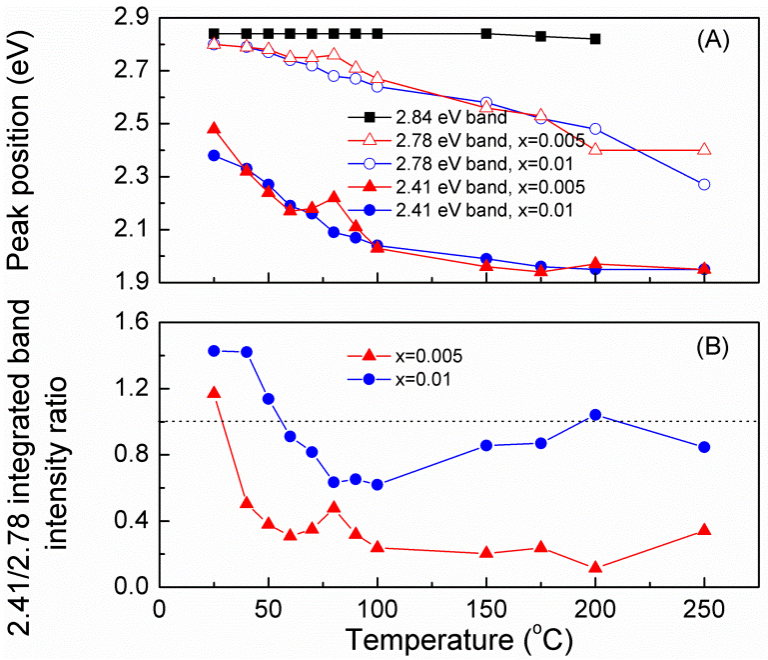

Figure 3.57. Results of Gaussian band spectral deconvolution as a function of temperature for x = 0.005, and 0.01: a) peak position, and b) integrated band intensity ratio.

References

[1] T.C.d. Oliveira, M.S.d. Silva, L.M.d. Jesus, D.V. Sampaio, J.C.A.d. Santos, N.R.d.S. Souza, R.S.d. Silva, Laser sintering and radioluminescence emission of pure and doped Y_2O_3 ceramics, Ceram Int, 40 (2014) 16209-16212.

[2] K. Papagelis, G. Kanellis, S. Ves, G.A. Kourouklis, Lattice Dynamical Properties of the Rare Earth Aluminum Garnets ($RE_3Al_5O_{12}$), Phys Status Solidi B, 233 (2002) 134-150.

[3] R. Lu, K.D. Jackson, A.M. Hofmeister, Infrared spectra from solid solutions of spessartine and yttrium aluminum garnet, Can Mineral, 31 (1993) 381-390.

[4] A.M. Hofmeister, K.R. Campbell, Infrared spectroscopy of yttrium aluminum, yttrium gallium, and yttrium iron garnets, J Appl Phys, 72 (1992) 638-646.

[5] J.P. Hurrell, S.P.S. Porto, I.F. Chang, S.S. Mitra, R.P. Bauman, Optical Phonons of Yttrium Aluminum Garnet, Phys Rev, 173 (1968) 851-856.

[6] K. Papagelis, S. Ves, Vibrational properties of the rare earth aluminum garnets, J Appl Phys, 94 (2003) 6491-6498.

[7] G. Gouadec, P. Colomban, Raman Spectroscopy of nanomaterials: How spectra relate to disorder, particle size and mechanical properties, Prog Cryst Growth Ch, 53 (2007) 1-56.

[8] G. Blasse, A. Bril, A new phosphor for flying-spot cathode-ray tubes for color television: yellow-emitting $Y_3Al_5O_{12}:Ce^{3+}$, Appl Phys Lett, 11 (1967) 53-55.

[9] V. Bachmann, C. Ronda, A. Meijerink, Temperature quenching of yellow Ce^{3+} luminescence in YAG:Ce, Chem Mater, 21 (2009) 2077-2084.

[10] Y. Zorenko, T. Voznyak, V. Gorbenko, E. Zych, S. Nizankovski, A. Dan'ko, V. Puzikov, Luminescence properties of $Y_3Al_5O_{12}$:Ce nanoceramics, J Lumin, 131 (2011) 17-21.

[11] Y. Zorenko, T. Zorenko, V.V. Gorbenko, T. Voznyak, V. Savchyn, P. Bilski, A. Twardak, Peculiarities of luminescent and scintillation properties of YAG:Ce phosphor prepared in different crystalline forms, Opt Mater, 34 (2012) 1314-1319.

[12] Y. Zorenko, V. Gorbenko, E. Mihokova, M. Nikl, K. Nejezchleb, A. Vedda, V. Kolobanov, D. Spassky, Single crystalline film scintillators based on Ce- and Pr-doped aluminium garnets, Radiat Meas, 42 (2007) 521-527.

[13] V. Babin, K. Blazek, A. Krasnikov, K. Nejezchleb, M. Nikl, T. Savikhina, S. Zazubovich, Luminescence of undoped LuAG and YAG crystals, Phys Status Solidi C, 2 (2005) 97-100.

[14] Y. Zorenko, T. Voznyak, V.V. Gorbenko, A. Doroshenko, A. Tolmachev, R. Yavetskiy, I. Petrusha, V. Turkevich, Comparative study of the luminescence of $Y_3Al_5O_{12}$ nanoceramics and single crystals under excitation by synchrotron radiation, Opt Mater, 35 (2013) 2049-2052.

[15] Y. Zorenko, A. Voloshinovskii, I. Konstankevych, V. Kolobanov, V. Mikhailin, D. Spassky, Luminescence of excitons and antisite defects in the phosphors based on garnet compounds, Radiat Meas, 38 (2004) 677-680.

[16] Y. Zorenko, T. Zorenko, T. Voznyak, A. Mandowski, X. Qi, M. Batentschuk, J. Friedrich, Luminescence of F^+ and F centers in AI_2O_3-Y_2O_3 oxide compounds, IOP Conference Series: Materials Science and Engineering, 15 (2010) 012060.
[17] A. Pujats, M. Springis, The F-type centres in YAG crystals Radiat Eff Defect S, 155 (2001) 65-69.
[18] M. Springis, A. Pujats, J. Valbis, Polarization of luminescence of colour centres in YAG crystals, J Phys-Condens Mat, 3 (1991) 5457-5461.
[19] X. Zeng, G. Zhao, J. Xu, H. Li, X. He, H. Pang, M. Jie, Effect of air annealing on the spectral properties of Ce:$Y_3Al_5O_{12}$ single crystals grown by the temperature gradient technique, J Cryst Growth, 274 (2005) 495-499.
[20] Y. Dong, G. Zhou, J. Xu, G. Zhao, F. Su, L. Su, H. Li, J. Si, X. Qian, X. Li, J. Shen, Color centers and charge state change in Ce:YAG crystals grown by temperature gradient techniques, J Cryst Growth, 286 (2006) 476-480.
[21] Y. Zorenko, A. Voloshinovskii, V. Savchyn, T. Voznyak, M. Nikl, K. Nejezchleb, V. Mikhailin, V. Kolobanov, D. Spassky, Exciton and antisite defect-related luminescence in $Lu_3Al_5O_{12}$ and $Y_3Al_5O_{12}$ garnets, Phys Status Solidi B, 244 (2007) 2180-2189.
[22] S.W.S. McKeever, Thermoluminescence of Solids, Cambrige University Press, Cambrige, 1988.
[23] J.T. Randall, M.H.F. Wilkins, Phosphorescence and Electron Traps. II. The Interpretation of Long-Period Phosphorescence, Proceedings of the Royal Society of London. Series A, Mathematical and Physical Sciences, 184 (1945) 390-407.
[24] J.T. Randall, M.H.F. Wilkins, Phosphorescence and Electron Traps. I. The Study of Trap Distributions, Proceedings of the Royal Society of London. Series A, Mathematical and Physical Sciences, 184 (1945) 365-389.
[25] R. Chen, S.W.S. McKeever, Theory of Thermoluminescence and Related Phenomena, World Scientific, Singapore, 1997.
[26] A.J.J. Bos, P. Dorenbos, A. Bessière, B. Viana, Lanthanide energy levels in YPO_4, Radiat Meas, 43 (2008) 222-226.
[27] M. Puchalska, P. Bilski, GlowFit — a new tool for thermoluminescence glow-curve deconvolution, Radiat Meas, 41 (2006) 659-664.
[28] C. Varney, F. Selim, Positron Lifetime Measurements of Vacancy Defects in Complex Oxides, Acta Phys Pol A, 125 (2014) 764-766.
[29] C. Varney, D. Mackay, A. Pratt, S. Reda, F. Selim, Energy levels of exciton traps in yttrium aluminum garnet single crystals, J Appl Phys, 111 (2012) 063505.
[30] E. Mihóková, M. Nikl, J.A. Mareš, A. Beitlerová, A. Vedda, K. Nejezchleb, K. Blažek, C. D'Ambrosio, Luminescence and scintillation properties of YAG:Ce single crystal and optical ceramics, J Lumin, 126 (2007) 77-80.

[31] A. Vedda, D. Di Martino, M. Martini, J. Mares, E. Mihokova, M. Nikl, N. Solovieva, K. Blazek, K. Nejezchleb, Trap levels in Y-aluminum garnet scintillating crystals, Radiat Meas, 38 (2004) 673-676.
[32] K. Wisniewski, C. Koepke, A.J. Wojtowicz, W. Drozdowski, M. Grinberg, S.M. Kaczmarek, J. Kisielewski, Excited State Absorption and Thermoluminescence in Ce and Mg Doped Yttrium Aluminum Garnet, Acta Phys Pol A, 95 (1999) 403-412.
[33] W. Hoogenstraaten, Electron traps in ZnS phosphors, Philips Res. Rep., 13 (1958).
[34] K. Papagelis, S. Ves, Infrared spectroscopy and lattice dynamical calculations of $Gd_3Al_5O_{12}$, $Tb_3Al_5O_{12}$ and $Lu_3Al_5O_{12}$ single crystals, J Phys Chem Solids, 64 (2003) 599-605.
[35] M. Nikl, J.A. Mares, N. Solovieva, H.-L. Li, X.-J. Liu, L.-P. Huang, I. Fontana, M. Fasoli, A. Vedda, C. D'Ambrosio, Scintillation characteristics of $Lu_3Al_5O_{12}$:Ce optical ceramics, J Appl Phys, 101 (2007) 0335151-0335155.
[36] M.G. Chapman, R.C. Walker, J.M. Schmitt, C.L. McPherson, F. Ameena, C.J. Kucera, C.A. Quarles, T.A. DeVol, J. Ballato, L.G. Jacobsohn, Effects of sintering temperature on open-volume defects and thermoluminescence of yttria and lutetia ceramics, J Am Ceram Soc, 99 (2016) 1449-1454.
[37] L.G. Jacobsohn, K. Serivalsatit, C.A. Quarles, J. Ballato, Investigation of Er-doped Sc_2O_3 transparent ceramics by positron annihilation spectroscopy, J Mater Sci, 50 (2015) 3183-3188.
[38] Y.V. Zorenko, V.I. Gorbenko, G.B. Stryganyuk, V.N. Kolobanov, D.A. Spasskii, K. Blazek, M. Nikl, Luminescence of excitons and antisite defects in $Lu_3Al_5O_{12}$:Ce single crystals and single-crystal films, Opt Spectrosc+, 99 (2005) 923-931.
[39] M. Nikl, A. Yoshikawa, K. Kamada, K. Nejezchleb, C.R. Stanek, J.A. Mares, K. Blazek, Development of LuAG-based scintillator crystals – A review, Prog Cryst Growth Ch, 59 (2013) 47-72.
[40] V. Babin, V.V. Laguta, A. Maaroos, A. Makhov, M. Nikl, S. Zazubovich, Luminescence of F^+-type centers in undoped $Lu_3Al_5O_{12}$ single crystals, Phys Status Solidi B, 248 (2011) 239-242.
[41] J. Pejchal, V. Babin, A. Beitlerova, R. Kucerkova, D. Panek, J. Barta, V. Cuba, A. Yamaji, S. Kurosawa, E. Mihokova, A. Ito, T. Goto, M. Nikl, A. Yoshikawa, Luminescence and scintillation properties of $Lu_3Al_5O_{12}$ nanoceramics sintered by SPS method, Opt Mater, 53 (2016) 54-63.
[42] J.-P. Zhong, H.-B. Liang, Q. Su, J.-Y. Zhou, J.-Y. Wang, Spectroscopic properties of vacancies and trap levels in $Lu_3Al_5O_{12}$:Ce^{3+} crystals, T Nonferr Metal Soc, 19 (2009) 1628-1633.
[43] V. Babin, V.V. Laguta, A. Makhov, K. Nejezchleb, M. Nikl, S. Zazubovich, Luminescence and ESR Study of Irregular Ce^{3+} Ions in LuAG:Ce Single Crystals, IEEE T Nucl Sci, 55 (2008) 1156-1159.
[44] M. Nikl, E. Mihokova, J. Pejchal, A. Vedda, Y. Zorenko, K. Nejezchleb, The antisite Lu_{Al} defect-related trap in $Lu_3Al_5O_{12}$:Ce single crystal, Phys Status Solidi B, 242 (2005) R119–R121.

[45] S. Liu, X. Feng, M. Nikl, L. Wu, Z. Zhou, J. Li, H. Kou, Y. Zeng, Y. Shi, Y. Pan, Fabrication and Scintillation Performance of Nonstoichiometric LuAG:Ce Ceramics, J Am Ceram Soc, 98 (2015) 510-514.
[46] E. Mihokova, A. Vedda, M. Fasoli, F. Moretti, A.L. Bulin, M. Nikl, M. Bettinelli, A. Speghini, H. Ogino, A. Yoshikawa, Defect states in $Lu_3Ga_xAl_{5-x}O_{12}$ crystals and powders, Opt Mater, 32 (2010) 1298-1301.
[47] M. Nikl, K. Kamada, V. Babin, J. Pejchal, K. Pilarova, E. Mihokova, A. Beitlerova, K. Bartosiewicz, S. Kurosawa, A. Yoshikawa, Defect engineering in Ce-doped aluminum garnet single crystal scintillators, Cryst Growth Des, 14 (2014) 4827-4833.
[48] A. Vedda, M. Martini, D. Di Martino, V.V. Laguta, M. Nikl, E. Mihikova, J. Rosa, K. Nejezchleb, K. Blazek, Defect states in $Lu_3Al_5O_{12}$:Ce crystals, Radiat Eff Defect S, 157 (2002) 1003-1007.
[49] A. Vedda, D. Di Martino, M. Martini, V.V. Laguta, M. Nickl, E. Mihokova, J. Rosa, K. Nejezchleb, K. Blazek, Thermoluminescence of Zr-codoped $Lu_3Al_5O_{12}$:Ce crystals, Phys Status Solidi A, 195 (2003) R1-R3.
[50] P.A. Douissard, T. Martin, F. Riva, Y. Zorenko, T. Zorenko, K. Paprocki, A. Fedorov, P. Bilski, A. Twardak, Epitaxial growth of LuAG:Ce and LuAG:Ce,Pr films and their scintillation properties, IEEE T Nucl Sci, 63 (2016) 1726-1732.
[51] Y. Zorenko, V. Gorbenko, T. Zorenko, K. Paprocki, M. Nikl, J.A. Mares, P. Bilski, A. Twardak, O. Sidletskiy, I. Gerasymov, B. Grinyov, A. Fedorov, Scintillating screens based on the single crystalline films of multicomponent garnets: New achievements and possibilities, IEEE T Nucl Sci, 63 (2016) 497-502.
[52] K. Serivalsatit, B. Kokuoz, B. Yazgan-Kokuoz, M. Kennedy, J. Ballato, Synthesis, Processing, and Properties of Submicrometer-Grained Highly Transparent Yttria Ceramics, J Am Ceram Soc, 93 (2010) 1320-1325.
[53] M. Mendelson, Average grain size in polycrystalline ceramics, J Am Ceram Soc, 52 (1969) 443-446.
[54] T. Yanagida, Y. Fujimoto, K. Kamada, D. Totsuka, H. Yagi, T. Yanagitani, Y. Futami, S. Yanagida, S. Kurosawa, Y. Yokota, A. Yoshikawa, M. Nikl, Scintillation Properties of Transparent Ceramic Pr:LuAG for Different Pr Concentration, IEEE T Nucl Sci, 59 (2012) 2146-2151.
[55] Y. Shi, M. Nikl, X. Feng, J.A. Mares, Y. Shen, A. Beitlerova, R. Kucerkova, Y. Pan, Q. Liu, Microstructure, optical, and scintillation characteristics of Pr^{3+} doped $Lu_3Al_5O_{12}$ optical ceramics, J Appl Phys, 109 (2011) -.
[56] W.H. Rhodes, Y. Wang, C. Brecher, J. Gary Baldoni, Loss and Recovery of Transparency in Pressure-Consolidated $Lu_3Al_5O_{12}$, J Am Ceram Soc, 94 (2011) 3655-3658.

[57] M.R. Marchewka, M.G. Chapman, H. Qian, L.G. Jacobsohn, Incorporation of Pr into LuAG ceramics, Opt Mater, 68 (2017) 53-57.
[58] Y. Shen, X. Feng, V. Babin, M. Nikl, A. Vedda, F. Moretti, E. Dell'Orto, Y. Pan, J. Li, Y. Zeng, Fabrication and scintillation properties of highly transparent Pr:LuAG ceramics using Sc,La-based isovalent sintering aids, Ceram Int, 39 (2013) 5985-5990.
[59] M. Nikl, H. Ogino, A. Krasnikov, A. Beitlerova, A. Yoshikawa, T. Fukuda, Photo-and radioluminescence of Pr-doped $Lu_3Al_5O_{12}$ single crystal, Phys Status Solidi A, 202 (2005) R4–R6.
[60] W. Drozdowski, P. Dorenbos, R. Drozdowska, A.J.J. Bos, N.R.J. Poolton, M. Tonelli, M. Alshourbagy, Effect of Electron Traps on Scintillation of Praseodymium Activated $Lu_3Al_5O_{12}$, IEEE T Nucl Sci, 56 (2009) 320-327.
[61] P. Dorenbos, The 5d level positions of the trivalent lanthanides in inorganic compounds, J Lumin, 91 (2000) 155-176.
[62] V. Gorbenko, Y. Zorenko, V. Savchyn, T. Zorenko, A. Pedan, V. Shkliarskyi, Growth and luminescence properties of Pr^{3+}-doped single crystalline films of garnets and perovskites, Radiat Meas, 45 (2010) 461-464.
[63] A. Yoshikawa, K. Kamada, F. Saito, H. Ogino, M. Itoh, T. Katagiri, D. Iri, M. Fujita, Energy Transfer to Pr^{3+} Ions in Pr:$Lu_3Al_5O_{12}$ (LuAG) Single Crystals, IEEE T Nucl Sci, 55 (2008) 1372-1375.
[64] G.H. Dieke, Spectra and Energy Levels of Rare Earth Ions in Crystals, John Wiley & Sons, 1968.
[65] M. Nikl, E. Mihokova, V. Laguta, J. Pejchal, S. Baccaro, A. Vedda, Radiation damage processes in complex-oxide scintillators, in: L. Juha, R.H. Sobierajski, H. Wabnitz (Eds.) Proceedings of SPIE: European Symposium on Optics and Optoelectronics: Damage to VUV, EUV, and X-ray Optics, 2007, pp. U92-U104.
[66] Y. Shen, X. Feng, Y. Shi, A. Vedda, F. Moretti, C. Hu, S. Liu, Y. Pan, H. Kou, L. Wu, The radiation hardness of Pr:LuAG scintillating ceramics, Ceram Int, 40 (2014) 3715-3719.
[67] J. Zhong, H. Liang, Q. Su, G. Zhang, P. Dorenbos, D.B. Muhammad, Effects of Annealing Treatments on Luminescence and Scintillation Properties of Ce:$Lu_3Al_5O_{12}$ Crystal Grown by Czochralski Method, J Rare Earth, 25 (2007) 568-572.
[68] R. Shannon, Revised effective ionic radii and systematic studies of interatomic distances in halides and chalcogenides, Acta Crystallogr A, 32 (1976) 751-767.
[69] K. Papagelis, J. Arvanitidis, E. Vinga, D. Christofilos, G.A. Kourouklis, H. Kimura, S. Ves, Vibrational properties of $(Gd_{1-x}Y_x)_3Ga_5O_{12}$ solid solutions, J Appl Phys, 107 (2010) 1135041-1135048.

[70] Y. Zorenko, V. Gorbenko, J. Vasylkiv, A. Zelenyj, A. Fedorov, R. Kucerkova, J.A. Mares, M. Nikl, P. Bilski, A. Twardak, Growth and luminescent properties of scintillators based on the single crystalline films of $Lu_{3-x}Gd_xAl_5O_{12}$:Ce garnet, Mater Res Bull, 64 (2015) 355-363.
[71] Y. Zorenko, V. Gorbenko, J. Vasylkiv, T. Strzyżewski, A. Fedorov, R. Kucerkova, J.A. Mares, M. Nikl, P. Bilski, A. Twardak, Growth and luminescent properties of scintillators based on the single crystalline films of $(Lu,Gd)_3(Al,Ga)_5O_{12}$:Ce garnets, J Lumin, 169, Part B (2016) 828-837.
[72] Y. Wu, Z. Luo, H. Jiang, F. Meng, M. Koschan, C.L. Melcher, Single crystal and optical ceramic multicomponent garnet scintillators: A comparative study, Nucl Instrum Meth A, 780 (2015) 45-50.
[73] F. Meng, Y. Wu, M. Koschan, C.L. Melcher, P. Cohen, Effect of annealing atmosphere on the cerium valence state and F^+ luminescence center in Ca-codoped GGAG:Ce single crystals, Phys Status Solidi A, 252 (2015) 1394-1401.
[74] F. Meng, M. Koschan, Y. Wu, C.L. Melcher, Relationship between Ca^{2+} concentration and the properties of codoped $Gd_3Ga_3Al_2O_{12}$:Ce scintillators, Nucl Instrum Meth A, 797 (2015) 138-143.
[75] Y. Wu, F. Meng, Q. Li, M. Koschan, C.L. Melcher, Role of Ce^{4+} in the Scintillation Mechanism of Codoped $Gd_3Ga_3Al_2O_{12}$:Ce, Phys Rev Appl, 2 (2014) 044009.
[76] M. Nikl, V. Babin, J.A. Mares, K. Kamada, S. Kurosawa, A. Yoshikawa, J. Tous, J. Houzvicka, K. Blazek, The role of cerium variable charge state in the luminescence and scintillation mechanism in complex oxide scintillators: The effect of air annealing, J Lumin, 169, Part B (2016) 539-543.
[77] X. Chen, H. Qin, Y. Zhang, Z. Luo, J. Jiang, H. Jiang, Preparation and Optical Properties of Transparent $(Ce,Gd)_3Al_3Ga_2O_{12}$ Ceramics, J Am Cer Soc, 98 (2015) 2352-2356.
[78] K. Kamada, T. Endo, K. Tsutumi, T. Yanagida, Y. Fujimoto, A. Fukabori, A. Yoshikawa, J. Pejchal, M. Nikl, Composition Engineering in Cerium-Doped $(Lu,Gd)_3(Ga,Al)_5O12$ Single-Crystal Scintillators, Cryst Growth Des, 11 (2011) 4484-4490.
[79] J. Luo, Y. Wu, G. Zhang, H. Zhang, G. Ren, Composition–property relationships in $(Gd_{3-x}Lu_x)(Ga_yAl_{5-y})O_{12}$:Ce (x = 0, 1, 2, 3 and y = 0, 1, 2, 3, 4) multicomponent garnet scintillators, Opt Mater, 36 (2013) 476-481.
[80] M. Kitaura, A. Sato, K. Kamada, S. Kurosawa, A. Ohnishi, M. Sasaki, K. Hara, Photoluminescence studies on energy transfer processes in cerium-doped $Gd_3Al_2Ga_3O_{12}$ crystals, Opt Mater, 41 (2015) 45-48.
[81] P. Dorenbos, Electronic structure and optical properties of the lanthanide activated $RE_3(Al_{1-x}Ga_x)_5O_{12}$ (RE=Gd, Y, Lu) garnet compounds, J Lumin, 134 (2013) 310-318.
[82] Z. Yang, J.H. Lin, M.Z. Su, Y. Tao, W. Wang, Photon cascade luminescence of Gd^{3+} in $GdBaB_9O_{16}$, J Alloy Compd, 308 (2000) 94-97.

[83] K. Bartosiewicz, V. Babin, K. Kamada, A. Yoshikawa, M. Nikl, Energy migration processes in undoped and Ce-doped multicomponent garnet single crystal scintillators, J Lumin, 166 (2015) 117-122.
[84] J. Luo, Y. Wu, G. Ren, Luminescence Property and Energy Transfer of Ce^{3+}, Eu^{3+} Co-doped $Lu_3Al_5O_{12}$ Polycrystals, J Inorg Mater, 29 (2014) 1211-1217.
[85] H. Zhang, Y. Wang, L. Han, Photoluminescence properties and energy transfer between Eu^{3+} and Nd^{3+} in polyborate $BaGdB_9O_{16}:Eu^{3+}$, Nd^{3+}, J Appl Phys, 109 (2011) 053109.
[86] S. Batygov, Y. Voronkov, N. Margiani, N. Ryskin, Luminescence of Nd^{3+} ions in garnets under high-energy excitation, in: G. Dube, L. Chase (Eds.) OSA proceedings on advanced solid-state lasers, Optical Society of America, Washington, 1991, pp. 368-370.
[87] A. Niklas, W. Jelenski, X-Ray Luminescence of YAG:Nd^{3+}, Phys Status Solidi A, 77 (1983) 393-398.
[88] D.C. Brown, C.D. McMillen, C. Moore, J.W. Kolis, V. Envid, Spectral properties of hydrothermally-grown Nd:LuAG, Yb:LuAG, and Yb:Lu_2O_3 laser materials, J Lumin, 148 (2014) 26-32.
[89] Z. Onderisinova, M. Kucera, M. Hanus, M. Nikl, Temperature-dependent nonradiative energy transfer from Gd^{3+} to Ce^{3+} ions in co-doped LuAG:Ce,Gd garnet scintillators, J Lumin, 167 (2015) 106-113.
[90] S. Hu, X. Qin, G. Zhou, C. Lu, L. Guanghui, Z. Xu, S. Wang, Luminescence characteristics of the Ce^{3+}-doped garnets: the case of Gd-admixed $Y_3Al_5O_{12}$ transparent ceramics, Opt Mater Express, 5 (2015) 2902-2910.
[91] Y. Pan, M. Wu, Q. Su, Tailored photoluminescence of YAG:Ce phosphor through various methods, J Phys Chem Solids, 65 (2004) 845-850.
[92] P.A. Tanner, L. Fu, L. Ning, B.-M. Cheng, M. Brik, G. , Soft synthesis and vacuum ultraviolet spectra of YAG:Ce^{3+} nanocrystals: reassignment of Ce^{3+} energy levels, J Phys Condens Mat, 19 (2007) 216213.
[93] A.A. Trofimov, C. Li, K.S. Brinkman, L.G. Jacobsohn, Luminescence investigation of Ce incorporation in garnet-type $Li_7La_3Zr_2O_{12}$, Opt Mater, 68 (2017) 7-10.
[94] A. Logéat, T. Köhler, U. Eisele, B. Stiaszny, A. Harzer, M. Tovar, A. Senyshyn, H. Ehrenberg, B. Kozinsky, From order to disorder: The structure of lithium-conducting garnets $Li_{7-x}La_3Ta_xZr_{2-x}O_{12}$ (x = 0–2), Solid State Ionics, 206 (2012) 33-38.
[95] J. Awaka, N. Kijima, H. Hayakawa, J. Akimoto, Synthesis and structure analysis of tetragonal $Li_7La_3Zr_2O_{12}$ with the garnet-related type structure, J Solid State Chem, 182 (2009) 2046-2052.
[96] C.A. Geiger, E. Alekseev, B. Lazic, M. Fisch, T. Armbruster, R. Langner, M. Fechtelkord, N. Kim, T. Pettke, W. Weppner, Crystal Chemistry and Stability of "$Li_7La_3Zr_2O_{12}$" Garnet: A Fast Lithium-Ion Conductor, Inorg Chem, 50 (2011) 1089-1097.

[97] X. Zhang, Z. Zhang, S.I. Kim, Y. Moon Yu, H.J. Seo, Photoluminescence properties of Eu^{3+} in garnet-type $Li_7La_3Zr_2O_{12}$ polycrystalline ceramics, Ceram Int, 40 (2014) 2173-2178.
[98] H. Suzuki, T.A. Tombrello, C.L. Melcher, J.S. Schweitzer, UV and gamma-ray excited luminescence of cerium-doped rare-earth oxyorthosilicates, Nucl Instrum Meth A, 320 (1992) 263-272.

CHAPTER FOUR

CONCLUSIONS AND FUTURE WORK

4.1. Conclusions

1. A detailed comparison between polycrystalline ceramic and single crystal scintillators, including several compositions (YAG:Ce, LuAG:Ce, LuAG:Pr, GLuGAG:Ce) was performed in terms of their microstructure, luminescence and scintillation.

2. Some reasons for lower performance of polycrystalline ceramic scintillators were identified:

   a. Lower optical transparency

   b. Higher level of structural disorder

   c. Higher luminescence self-absorption

3. Results suggest that polycrystalline ceramics has shallower traps that single crystal

4. The first systematic evaluation of microstructure, luminescence, and scintillation performance of GLuGAG:Ce in the form of polycrystalline ceramics was conducted.

5. In the attempt of materials discovery, LLZO:Ce was fabricated and its luminescent properties investigated for the first time.

6. Detailed evaluation of thermoluminescence of LuAG:Ce and YAG:Ce above room temperature was accomplished.

7. Demonstrated the capability of ATR FTIR for the characterization of polycrystalline ceramic scintillators.

4.2. Future work

- Expand TL evaluation of YAG:Ce and LuAG:Ce by means of different methods of TL analysis, including T_m-T_{stop} method and method of multiple heating rates with heating rate range below 1 °C/sec.
- Prepare and characterize ceramics with the same density but different grain sizes to broaden investigation of microstructure influence on the materials performance.
- Perform RL and TL of GLuGAG:Ce to complete the investigation of their luminescent properties.